



**HAL**  
open science

# Extensions of Fractional Brownian Fields and Morphological Spectral Analysis for Discrimination of Catalysts

Zhangyun Tan

► **To cite this version:**

Zhangyun Tan. Extensions of Fractional Brownian Fields and Morphological Spectral Analysis for Discrimination of Catalysts. Methodology [stat.ME]. Université Grenoble Alpes, 2016. English. NNT : . tel-01532841

**HAL Id: tel-01532841**

**<https://hal.science/tel-01532841>**

Submitted on 3 Jun 2017

**HAL** is a multi-disciplinary open access archive for the deposit and dissemination of scientific research documents, whether they are published or not. The documents may come from teaching and research institutions in France or abroad, or from public or private research centers.

L'archive ouverte pluridisciplinaire **HAL**, est destinée au dépôt et à la diffusion de documents scientifiques de niveau recherche, publiés ou non, émanant des établissements d'enseignement et de recherche français ou étrangers, des laboratoires publics ou privés.

## THÈSE

Pour obtenir le grade de

### **DOCTEUR DE LA COMMUNAUTÉ UNIVERSITÉ GRENOBLE ALPES**

Spécialité : **STIC - Traitement de l'Information**

Arrêté ministériel : 7 août 2006

Présentée par

**Zhangyun TAN**

Thèse dirigée par **Abdourrahmane M. ATTO**  
et codirigée par **Olivier ALATA**  
et co-encadrée par **Maxime MOREAUD**

préparée au sein du **Laboratoire LISTIC**  
et de l'**Ecole Doctorale SISEO**

# **Extensions of Fractional Brownian Fields and Morphological Spectral Analysis for Discrimination of Cat- alysts**

Thèse soutenue publiquement le **19 December 2016**,  
devant le jury composé de :

**M. Jean-Christophe BURIE**

Professeur - Université de La Rochelle, Rapporteur

**M. Johan DEBAYLE**

Maître de conférences, HDR - École des Mines de Saint-Etienne, Rapporteur

**M. Dominique PASTOR**

Professeur - Télécom Bretagne, Examineur

**M. Abdourrahmane M. ATTO**

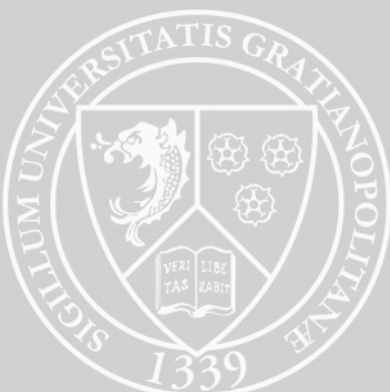
Université Savoie Mont Blanc, Directeur de thèse

**M. Olivier ALATA**

Université Jean Monnet Saint-Etienne, Co-Directeur de thèse

**M. Maxime MOREAUD**

IFP Energies Nouvelles, Co-Encadrant de thèse





---

## ACKNOWLEDGMENT

---

The realized study during these three last years will not be accomplished without the encouragement and guidance of many individuals and organizations.

I would like to express my very deep gratitude to my supervisors, Abdourrahmane M. ATTO, Associate Professor at LISTIC (Laboratoire d'Informatique, Systèmes, Traitement de l'Information et de la Connaissance) of University of Savoie Mont Blanc, Olivier ALATA, Professor at Lab. Hubert Curien of University Jean Monnet Saint-Etienne and Maxime MOREAUD, R & D Project Manager at IFP Energies Nouvelles, who guided me at each and every aspect of this thesis. They have taught me how to do the research, how to enlarge the scope of academic knowledge, answered all my questions, helped me better understand theory as well as its application and always encouraged me to solve the questions independently. Throughout this research work, they brought me their competences in stochastic modeling, morphology, texture analysis, transmission electron microscopy, programming... I value their constructive criticisms of my work and writing. They showed me that working hard in academe can be rewarding and satisfying. I am looking forward to more collaborations in the future.

I am quite grateful to Professor Dominique PASTOR to be the president of the jury, which is such a great honor for me. I would like to thank Professor Jean-Christophe BURIE and Associate Professor Johan DEBAYLE. They agreed to serve as referees of my thesis.

I also would like to thank the faculty and staff. I am very pleased to work in the laboratory of LISTIC of University of Savoie Mont Blanc. Besides, the visit and work in Lab. Hubert Curien of University Jean Monnet Saint-Etienne and IFP Energies Nouvelles were also very interesting and helped me advance well my thesis study. I wish to express my thanks to administrative and technical staff, Joelle Pellet, Assia Combettes, Florent Baldini and Jean-Claude Jouffre for their friendly and warmly help. I would like to thank professors Kavé Salamatian, Didier Coquin, Patrick Lambert, Emmanuel Trouvé and Yajing Yan. They taught me a lot during my stay in LISTIC. Their explanation, kindness and encouragements gave me much motivation to do the research. I would

like to thank my fellow Phd students and my friends: Meriem Hafsi, Quentin Hoareau, Matthias Jauvin, Thang Long Nguyen, Rihab Ben Ameer, Hela Hadhri, Cédric Deffo Sikounmo, Rizlène Outach, Bastien Rizzon, Jingxiu Su and Haixing He for their friendly and warmly help and suggestion personally and professionally.

I would like to thank the colleague Florent Moreau in IFP Energies Nouvelles for his help to collect the image database.

I will forever be thankful to my friends Dazeng Zhang and Dr. Raghavendra Nunna. They have been helpful in providing advice many times before and during my thesis even when I was irritable and depressed.

My deepest gratitude goes to my parents, my boyfriend with my future twins sons, my brother and sister with her husband as well as their son for their total and unwavering support, encouragement and confidence during my studies.

Thanks to everyone who has given me their valuable time, skills and enthusiasm during these last years!

Finally, I would like to show my sincere thanks to the Rhône-Alpes region in the terms of ARC6 who has awarded me the scholarships in the last three years and IFP Energies Nouvelles who has provided research displacement funding. Their financial aides are also important for the completion of this thesis.

---

## ABBREVIATIONS

---

AEM: Analytical Electron Microscopy  
AR: Auto-Regressive  
ARC6: Academies of Research Community 6  
ARCH: Auto-Regressive Conditional Heteroscedastic  
ARFBF: Auto Regressive Fractional Brownian Field  
ARFIMA: Auto-Regressive Fractional Integrated Moving Average  
ARMA: Auto-Regressive Moving Average  
ASOSS: Asymptotically Second Order Self-Similar  
ASS: Asymptotically Self-Similar  
 $Cat_X$ : Catalyst X  
 $Cat_Y$ : Catalyst Y  
CMFBF: Convolution Mixture of 2-D FBF and 2-D modulated FBF  
DPF: Diesel Particulate Filters  
DPM: Diesel Particle Matter  
DSWT: Discrete Stationary Wavelet Transform  
EELS: Electron Energy Loss Spectroscopy  
FBF: Fractional Brownian Field  
FBM: Fractional Brownian Motion  
FFT: Fast Fourier Transform  
FGN: Fractional Gaussian Noise  
FI process: Fractional Integrated process  
GARMA: Gegenbauer Auto-Regressive Moving Average  
GFBF: Generalized Fractional Brownian Field  
HM: Harmonic Mean  
HRTEM: High Resolution Transmission Electron Microscopy  
 $H$ -SS process:  $H$  Self-Similar process  
 $H$ -SSSI process:  $H$  Self-Similar process with Stationary Increments  
IDSWT: Inverse Discrete Stationary Wavelet Transform  
 $k$ -factor GARMA process:  $k$ -factor Gegenbauer Auto-Regressive Moving Average process  
 $K$ -factor GFBF:  $K$ -factor Generalized Fractional Brownian Field  
Log-RDWP: Log-Regression on Diagonal Wavelet Packet spectrum

Log-RPHW: Log-Regression based on Poly-Harmonic Wavelet  
Log-RPWP: Log-Regression on Polar representation of Wavelet Packet spectrum  
MA: Moving Average  
ML-PHW: Maximum Likelihood based on Poly-Harmonic Wavelet  
MSE: Mean Square Error  
NC: Non-Causal  
NSHP: Non Symmetric Half Plan  
PSD: Power Spectral Density  
QP: Quart Plan  
S $\alpha$ S: Symmetric  $\alpha$  Stable  
SC: Semi-Causal  
SOSS: Second Order Self-Similar  
SS: Self-Similar  
STEM: Scanning Transmission Electron Microscopy  
TEM: Transmission Electron Microscopy  
WHFR: Wavelet based High Frequency Removal  
WP: Wavelet Packet  
WPS: Wavelet Packet Spectrum

---

## NOTATIONS

---

- $A$ : 2-D Auto-Regressive process  
 $\alpha_i$ : an adaptive threshold  
 $B$ : 2-D isotropic Fractional Brownian Field process  
 $B_{H_0}$ : 2-D standard isotropic Fractional Brownian Field process  
 $B_{H_q}$ : 2-D modulated isotropic Fractional Brownian Field process  
 $q$  ( $q \in \{1, 2, \dots, Q\}$ ): Hurst parameter index of modulated isotropic Fractional Brownian Field process  
 $B_{G_{H_k}}$ : Generalized Fractional Brownian Field process  
 $k$  ( $k \in \{0, 1, \dots, Q\}$ ): Hurst parameter index of Generalized Fractional Brownian Field process  
 $a_{m_1, m_2}$ : coefficients of 2-D AR process  
 $C = \frac{N!}{2(N-2)!}$ : the number of all possible combinations of the log-ratios  
 $C_h$ : condition  $C_h$  on a function  $h$   
 $E(x, y)$ : an independent and identically distributed process with zero mean and variance  $\sigma_e$   
 $G$ : distance value between fringes in HRTEM image  
 $\Delta_G$ : distance variation  
 $\Gamma$ : stand gamma function  
 $H$ : Hurst parameter,  $0 < H < 1$   
 $I(x, y)$ : Image  
 $K$ : kernel smoothing function  
 $L_\theta$ : tangential length of the detected lobe  
 $M_1, M_2$ : 2-D AR order  
 $\mu$ : mean  
 $\Phi$ : polynomial  
 $\Psi$ : polynomial  
 $P_i[r, \theta]$ : the point designing ième maximum value in estimated PSD and  $i \in \{1, 2\}$   
 $Q$ : an binary image using a morphological reconstruction  
 $\rho$ : auto-correlation function  
 $S$ : Power Spectral Density  
 $S(r, \theta)$ : Power Spectral Density in polar coordinate in frequency domain

$S(u, v)$ : Power Spectral Density in Cartesian coordinate in frequency domain,  $u \in [-\pi, \pi]$   
and  $v \in [-\pi, \pi]$   
 $\sigma$ : standard derivation  
 $\sigma_b^2$ : the variance of a white Gaussian noise  
*skew*: third moment skewness  
*kurt*: fourth moment kurtosis  
 $T$ : Cartesian-to-polar transform  
 $\theta_{M_1, M_2}$ : the parameter set of 2-D AR model  
*var*: variance  
 $Y$ : CMFBBF model  
 $Z$ : 2-D ARFBBF model

---

## ABSTRACT

---

My thesis concerns statistical characterization of spatial arrangements of fringes (active phases) in the catalysts imaged by High Resolution Transmission Electron Microscopy (HRTEM). The contributions proposed in this thesis are two statistical models for the description of these HRTEM image contents.

The first model involves 2-D Fractional Brownian Field (FBF) and 2-D Auto Regressive (AR) models, as well as morphological analysis of the spectra associated with these models (ARFBF morphological analysis). Concerning FBF modeling, we propose two methods for estimating its parameter: Log-RDWP (Log-Regression on Diagonal Wavelet Packet spectrum) and Log-RPWP (Log-Regression on Polar representation of Wavelet Packet spectrum). We propose a morphological method on ARFBF spectrum for detecting and identifying HRTEM texture features. It is shown that the morphological properties of spectral features make possible, a separation between different catalysts.

The second model proposed in this thesis is a generalization of FBF (GFBB) constructed by using convolution and modulation operators of several FBF. The textures synthesized from GFBB model are shown to present some structural similarities with certain fringe structures present in HRTEM images. We details association of a GFBB to an HRTEM fringe by considering a GFBB mixture comprising an FBF and a modulated version of FBF (model called CMFBF). This CMFBF has a spectral representation associated with two poles (spectral peaks) and two Hurst parameters. The spectral peak at zero frequency characterizes the background of the HRTEM image and the first Hurst parameter describes the regularity of this background. The second peak and its corresponding Hurst parameter is representative of the fringe structural and spectral contents.

**Keywords:** HRTEM image ; Active phases of catalyst ; ARFBF modeling ; Morphology analysis ;  $K$ -factor GFBB modeling ; Hurst parameter estimation.



Ma thèse porte sur la caractérisation des arrangements spatiaux de phases actives dans les catalyseurs observés à Haute Résolution par Microscopie Électronique en Transmission (imagerie HRMET). Les contributions de la thèse sont la proposition de deux modèles statistiques pour analyser ces arrangements dans les images HRMET.

Le premier modèle est une intégration, par opération de convolution, des Champs Browniens Fractionnaires (CBF) et des champs Auto-Régressifs (AR), donnant ainsi une famille de modèles appelés ARCBF. Le modèle ARCBF requiert l'estimation d'un paramètre de Hurst. Nous proposons à cet effet, deux méthodes d'estimation : la méthode Log-RDWP (log-régression sur la diagonale du spectre des paquets d'ondelettes) et la méthode Log-RPWP (log-régression sur la représentation en coordonnées polaires du spectre des paquets d'ondelettes). L'analyse morphologique des spectres associés à ces modèles (analyse spectrale morphologique ARCBF) permet de détecter et d'identifier les attributs associés aux textures observées sur les images HRMET, attributs qui rendent possible la discrimination de différents types de catalyseurs à partir d'observations de leurs échantillons représentatifs.

Le second modèle est une Généralisation des CBF (GCBF) construite par convolution de plusieurs champs CBF modulés. Nous donnons les détails de l'association d'un modèle GCBF à une texture observée sur les images HRMET : pour une imagerie donnée, cette association se réduit au choix d'une sous-classe des GCBF consistant à la convolution d'un CBF et d'un CBF modulé (modèle dit CMCBF). Un CMCBF admet une représentation spectrale associée à deux pôles (pics spectraux) et deux paramètres de Hurst. Le premier pic spectral est observé à la fréquence zéro et caractérise le fond de l'imagerie (arrière-plan) dont la régularité est décrite par le premier paramètre de Hurst. Le second pic est représentatif d'une frange dont les caractéristiques sont le second paramètre de Hurst et la fréquence de modulation bidimensionnelle. Les textures synthétisées à partir du modèle GCBF/CMFBBF admettent des contenus structurés présentant des similitudes avec de nombreuses franges observables dans les images HRMET.

**Mots clés:** HRMET image; Phases actives dans les catalyseurs; Modélisation ARFBBF; Analyse morphologique; Modélisation  $K$ -factor GFBF; Estimation du paramètre Hurst.



<b>List of Figures</b>		<b>17</b>
<b>List of Tables</b>		<b>21</b>
<b>1 General introduction</b>		<b>23</b>
1.1 Context and motivation . . . . .		23
1.2 Contributions . . . . .		24
1.3 Thesis outline . . . . .		25
<b>2 High Resolution Transmission Electron Microscopy (HRTEM) imaging</b>		<b>27</b>
2.1 Transmission Electron Microscopy (TEM) . . . . .		27
2.1.1 Schematic description of a TEM . . . . .		27
2.1.2 Specimen preparation . . . . .		30
2.1.3 TEM imaging theory . . . . .		30
2.1.4 HRTEM . . . . .		33
2.2 Observations of soot nanostructure by HRTEM . . . . .		33
2.3 Observations of active phase of hydrotreating catalysts . . . . .		35
2.3.1 HRTEM images and sub-images of catalyst X ( $Cat_X$ ) . . . . .		36
2.3.2 HRTEM images and sub-images of catalyst Y ( $Cat_Y$ ) . . . . .		36
2.4 Structure of fringes (active phases) of catalyst in spatial domain and in frequency domain . . . . .		39
<b>3 Generalities on stochastic modeling</b>		<b>43</b>
3.1 Introduction . . . . .		43
3.2 Short versus long memory process . . . . .		43
3.2.1 Stationary processes . . . . .		43
3.2.2 Short memory process . . . . .		44
3.2.3 Long memory process . . . . .		44
3.3 Self-similar process . . . . .		45
3.3.1 Continuous time self-similar process . . . . .		45
3.3.1.1 Self-similar process in continuous time . . . . .		45

3.3.1.2	Self-similar process with stationary increments in continuous time . . . . .	45
3.3.2	Discrete time self-similar process . . . . .	46
3.3.2.1	Self-similar process in discrete time . . . . .	46
3.3.2.2	Second order self-similar process in discrete time . . . . .	46
3.3.3	Relationships between (asymptotical) self-similarity and short/long memory behaviors . . . . .	47
3.4	Examples of self-similar and/or long range dependence processes in continuous time . . . . .	48
3.4.1	Gaussian H-SSSI models - fractional Brownian motion . . . . .	48
3.4.1.1	Brownian motion . . . . .	48
3.4.1.2	Fractional Brownian Motion (FBM) . . . . .	48
3.4.2	Non-Gaussian H-SSSI models . . . . .	49
3.5	Examples of self-similar and short/long range dependence processes in discrete time . . . . .	50
3.5.1	FGN process . . . . .	51
3.5.2	$k$ -factor GARMA process . . . . .	51
3.5.2.1	Properties . . . . .	52
3.5.2.2	ARFIMA process . . . . .	53
3.5.2.3	FI process . . . . .	54
3.6	2-D stochastic modeling . . . . .	55
3.6.1	2-D isotropic FBF modeling . . . . .	56
3.6.2	2-D ARMA, AR, MA modeling . . . . .	56
3.6.2.1	AR model . . . . .	58
3.6.2.2	MA model . . . . .	60
3.6.2.3	Causality . . . . .	60
<b>4</b>	<b>2-D G-AR-FBF modeling and parameter estimation</b> . . . . .	<b>63</b>
4.1	2-D Auto-Regressive Fractional Brownian Field . . . . .	63
4.1.1	ARFBF Definition and Spectral Characterization . . . . .	64
4.1.2	ARFBF modeling procedure . . . . .	65
4.2	2-D $K$ -factor Generalized Fractional Brownian Fields . . . . .	66
4.2.1	2-D $K$ -GFBBF modeling . . . . .	66
4.2.1.1	Modulated Fractional Brownian Field $B_{H_q}$ . . . . .	66
4.2.1.2	Generalized Fractional Brownian Fields $B_{GH_K}$ with $K$ spectral poles . . . . .	67
4.2.1.3	A particular sub-class of GFBBF: the CMFBF . . . . .	68
4.3	Hurst parameter estimation of 2-D FBF . . . . .	69
4.3.1	Log-RDWP estimation method . . . . .	69
4.3.2	Log-RPWP estimation method . . . . .	70
4.3.3	Results of Hurst parameter estimation . . . . .	71
4.3.4	Performance of Log-RPWP Hurst parameter estimator . . . . .	72
<b>5</b>	<b>Application to HRTEM image characterization</b> . . . . .	<b>75</b>
5.1	$K$ -factor GFBBF samples and Soot HRTEM textures . . . . .	75

5.2	Convolution mixture of FBF and modulated FBF modeling for HRTEM catalyst texture synthesis . . . . .	77
5.2.1	Motivation . . . . .	77
5.2.2	CMFBB modeling for catalyst HRTEM image . . . . .	79
5.2.2.1	Step 1: FBF modeling and suppression . . . . .	79
5.2.2.2	Step 2: Modulated FBF parameter estimation . . . . .	79
5.2.3	Synthesis of catalyst HRTEM images from CMFBB . . . . .	80
5.3	Morphology analysis of catalyst active phase using ARFBB modeling . . . . .	84
5.3.1	Problem formulation . . . . .	84
5.3.1.1	Pre-processing - WHFR . . . . .	85
5.3.2	ARFBB modeling of HRTEM image . . . . .	86
5.3.2.1	FBF modeling and suppression . . . . .	86
5.3.2.2	AR modeling . . . . .	87
5.3.3	Morphological analysis of HRTEM ARFBB features . . . . .	88
5.3.3.1	Morphological analysis . . . . .	88
5.3.3.2	Lobe detection . . . . .	88
5.3.3.3	Characterization on average spatial distance between atomic layers $G$ , distance variation $\Delta_G$ and tangential length $L_\theta$ . . . . .	90
5.3.4	Statistical analysis for catalyst discrimination . . . . .	91
5.3.4.1	Statistical distributions of $G$ , $\Delta_G$ and $L_\theta$ . . . . .	91
5.3.4.2	Kolmogorov-Smirnov test for catalyst discrimination . . . . .	93
<b>6</b>	<b>General conclusion</b>	<b>99</b>
<b>7</b>	<b>Appendix: résumé substantiel</b>	<b>101</b>
	<b>Bibliography</b>	<b>107</b>



---

## List of Figures

---

1.1	Material texture structure and fringe description . . . . .	24
2.1	Transmission electron microscopy (Tecnai G2 - type of MET used at IFP Energies nouvelles). . . . .	28
2.2	Diagram outlining the internal components of a basic TEM system. From " <a href="https://en.wikipedia.org">https://en.wikipedia.org</a> ". . . . .	29
2.3	Specimen preparation. . . . .	31
2.4	Contrast absorption introduced by the diaphragm in sample outlet. $t$ represents the thickness of thin blade. Figure provided by [22]. . . . .	31
2.5	Electron $e^-$ , elastic scattering (no energy change) with relatively large angle of deviation and inelastic scattering (energy change) with small angle of deviation. . . . .	32
2.6	High Resolution Transmission Electron Microscope (HRTEM) imaging. From [20]. . . . .	34
2.7	HRTEM image of soot. . . . .	34
2.8	HRTEM images and sub-images of $Cat_X$ . . . . .	36
2.9	Sub-images of $Cat_X$ . . . . .	37
2.10	HRTEM images and sub-images of $Cat_Y$ . . . . .	37
2.11	Sub-images of $Cat_Y$ . . . . .	38
2.12	HRTEM image and its PSD, see [34]. . . . .	38
2.13	Structure of fringes: (1) parallel and constant inter-distance, (2) parallel and non-constant inter-distance and (3) non-parallel, in spatial domain as well as in frequency domain. . . . .	40
3.1	FBF texture samples for different Hurst parameters $H$ . . . . .	57
3.2	Linear time invariant system. . . . .	57
3.3	Quarter plan prediction supports denoted (a) $D_{QP_1}$ (see Eq. (3.50)) and (b) $D_{QP_2}$ (see Eq. (3.51)) with finite order $(M_1, M_2) = (2, 2)$ and $(x, y) \in \mathbb{Z}^2$ . . . . .	58
3.4	Each row presents an original image with its corresponding synthesized image from the corresponding AR model. . . . .	59

3.5	Causal Non Symmetric Half Plan (NSHP) prediction support $D_{NSHP}$ , $(m_1, m_2) \in \mathbb{Z}^2$ and $(x, y) \in \mathbb{Z}^2$ .	61
3.6	Semi-Causal (SC) prediction support $D_{SC}$ , $(m_1, m_2) \in \mathbb{Z}^2$ and $(x, y) \in \mathbb{Z}^2$ .	61
3.7	Non-Causal (NC) prediction support $D_{NC}$ , $(m_1, m_2) \in \mathbb{Z}^2$ and $(x, y) \in \mathbb{Z}^2$ .	62
4.1	Procedure of ARFBF modeling.	65
4.2	CMFBF modeling procedure.	68
4.3	Mean square value computed with values obtained in Tab. 4.1 and Tab. 4.2 for $RDWP_8$ and $RPWP_{32}$ (best results) with image size equal to $512 \times 512$ and $2048 \times 2048$ .	72
5.1	$K$ -factor GFBF $\mathcal{E}_{\mathcal{H}_K}$ for different values of $K$ . Figure is originated from [10].	76
5.2	Wavelet spectra $S_W \mathcal{E}_{\mathcal{H}_K}$ of $K$ -factor GFBF $\epsilon_{\mathcal{H}_K}$ texture images given in Fig. 5.1. Spectra are given in $[0, \frac{\pi}{2}] \times [0, \frac{\pi}{2}]$ . Figure is originated from [10].	76
5.3	HRTEM image $I_{TEM}$ (top-left) and its wavelet spectrum $S_W I_{TEM}$ (top-right). Bottom: some Zooms (Z) on regions of image $I_{TEM}$ and their wavelet spectrum.	77
5.4	The original image $I_1$ (catalyst HRTEM) with its WPS (Wavelet Packet Spectrum) $S_1$ are given in the first row. The image $I_4$ (row 4) has been synthesized from CMFBF modeling of $I_1$ . The intermediate images ( $I_2, I_3$ ) and the spectral features ( $S_2, S_3$ ) obtained at every step of this modeling are given for illustration. The WPS of $I_4$ is $S_4$ and it shows strong similarities with $S_1$ .	78
5.5	The complete CMFBF framework.	80
5.6	Synthesis of catalyst HRTEM image using CMFBF estimated Hurst parameters $H_0$ and $H_1$ from $im_1$ . In the first row, the original image and its WPS; in the second row, the residual image (after removing the FBF contribution from the original image) and its WPS; in the third row, the demodulated version of the residual image and its WPS. Finally, the last row presents the synthesized image with its corresponding WPS.	81
5.7	Synthesis of catalyst HRTEM image using CMFBF estimated Hurst parameters $H_0$ and $H_1$ from $im_2$ . In the first row, the original image and its WPS; in the second row, the residual image (after removing the FBF contribution from the original image) and its WPS; in the third row, the demodulated version of the residual image and its WPS. Finally, the last row presents the synthesized image with its corresponding WPS.	82
5.8	Selected 18 $Cat_X$ HRTEM images.	83
5.9	Selected 8 $Cat_Y$ HRTEM images.	83
5.10	Images synthesized from an average of $H_0$ and $H_1$ parameters of 18 $Cat_X$ HRTEM images using CMFBF modeling and its WPS.	83
5.11	Images synthesized from an average of $H_0$ and $H_1$ parameters of 8 $Cat_Y$ HRTEM images using CMFBF modeling and its WPS.	84
5.12	Morphology analysis procedure using ARFBF model.	84
5.13	ARFBF modeling procedure of HRTEM image.	86
5.14	AR modeling.	87
5.15	Estimated PSD $S^*(r, \theta)$ from AR in polar coordinate.	88
5.16	Estimated PSD $S^*(r, \theta)$ from AR in polar coordinate and lobe detection.	89

5.17	The spectral lobe detected can be considered as an ellipse embedded in a bounding box $(r_{min}, r_{max}, \theta_{min}, \theta_{max})$ . . . . .	90
5.18	Kernel distributions of distance (left), distance variation (center) and tangential length (right) of the detected lobe of $Cat_X$ (— in blue) and $Cat_Y$ (— in red). . . . .	93
5.19	ARFBF modeling morphology analysis of HRTEM images of catalyst - ARFBF modeling morphological characterization of HRTEM image of catalyst and catalyst discrimination. . . . .	97
7.1	Modèle MCCBF pour la synthèse de textures HRMET de catalyseurs. . .	104
7.2	Application du modèle ARCBF aux images HRMET de catalyseurs . . .	105



---

## List of Tables

---

4.1	Mean values of estimated $\hat{\alpha}$ and their variances computed from 10 FBF realizations with image size equal to $512 \times 512$ . . . . .	71
4.2	Mean values of estimated $\hat{\alpha}$ and their variances computed from 10 FBF realizations with image size equal to $2048 \times 2048$ . . . . .	72
4.3	Mean values and standard deviations for estimated Hurst parameters from 10 FBF realizations. . . . .	73
5.1	Statistics of distance (see Eq. (5.11)), distance variation (see Eq. (5.12)) and tangential length (see Eq. (5.15)) features of the detected lobe of catalyst image databases ( $Cat_X$ and $Cat_Y$ ). . . . .	93
5.2	1-D Kolmogorov–Smirnov test of $Cat_X$ and $Cat_Y$ . . . . .	94
5.3	1-D Kolmogorov–Smirnov test of sub-classes $Cat_X^m$ and $Cat_Y^n$ of $Cat_X$ and $Cat_Y$ respectively, $m, n \in \{1, 2\}$ . . . . .	95
5.4	2-D Kolmogorov–Smirnov test of $Cat_X$ and $Cat_Y$ . . . . .	96
5.5	2-D Kolmogorov–Smirnov test of sub-classes $Cat_X^m$ and $Cat_Y^n$ of $Cat_X$ and $Cat_Y$ respectively, $m, n \in \{1, 2\}$ . . . . .	96



### 1.1 Context and motivation

My thesis aims at proposing statistical models for the analysis and characterization of textures issued from Transmission Electron Microscopy (TEM) images. High Resolution TEM (HRTEM) imaging is used to observe material at nano scales (nano texture structures). At these scales, we can analyze spatial arrangements of catalyst active phases which produce fringe patterns in the HRTEM images. Characterizing these fringes is useful for understanding the properties of the observed material. In this thesis, we have performed statistical and morphological characterizations of structures that are observed by HRTEM imaging systems.

The originality of my thesis is addressing a joint statistical and morphological framework for deriving a characterization of HRTEM micro-textures. This framework relies on several statistical results for texture characterization (see [8, 9, 36, 57, 81]) that are essential in deriving texture descriptors.

With TEM micro-graphs at high resolution (namely HRTEM), dark or bright linear patterns (fringes) (see Fig. 1.1) can be observed and correspond to active phases depositing on the catalyst support. HRTEM images present a very important texture aspect with fringes of different natures and different orientations. We propose to use a joint statistical and morphology model-based approach to characterize these fringes.

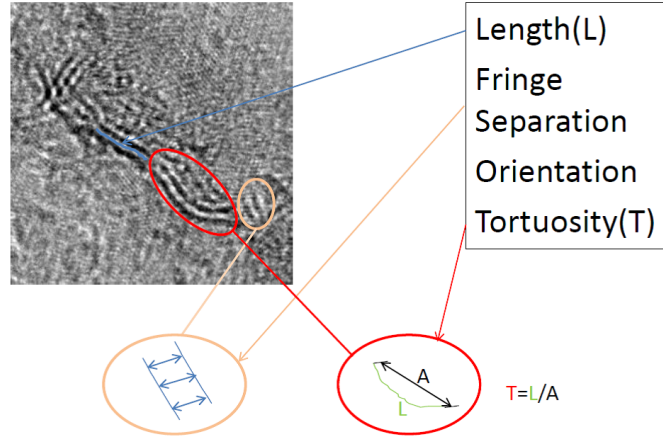


Figure 1.1: Material texture structure and fringe description

## 1.2 Contributions

The contributions presented in this thesis include two proposed statistical models in order to capture the spatial arrangements of fringes in the catalysts imaged by HRTEM:

- the first model involves 2-D Fractional Brownian Field (FBF) and 2-D Auto-Regressive (AR) models, as well as the morphological spectral consideration (Auto-Regressive Fractional Brownian Field (ARFBF) morphological analysis);
- the second model is based on convolution and modulation operators of FBF and represents a class of  $K$ -factor Generalized Fractional Brownian Field (GFBF) that are non-stationary and multi-fractional field models.

Both ARFBF and GFBF modeling require in practice, FBF based parameter estimations restricted to small samples (local behavior as an FBF is the neighborhood of any given spectral peak). Concerning these FBF based local parameter estimations, we propose two methods that are adapted to small samples:

- Log-RDWP estimation: Log-Regression on Diagonal Wavelet Packets,
- Log-RPWP estimation: Log-Regression on Polar representation of Wavelet Packets.

These methods outperforms standard FBF parameter estimation methods and show robustness with respect to FBF sample generators.

The highlights of the thesis are the following. With ARFBF modeling:

- we obtain a fractionally regularized estimator of the texture Power Spectral Density (PSD),
- we derive a morphological method to detect and identify the most relevant spectral features (lobes) and finally

- we propose a method for clustering different catalysts from the properties of detected ARFBF lobes.

With GFBF modeling, we show that many textures synthesized from HRTEM texture parameters have strong structural similarities with those of certain original HRTEM structures.

Applications of this work are expected to have environmental impacts in terms of:

- lowering material environmental impact by using more specialized catalysts (references [115, 71, 58, 93] are with the same goal) ;
- improving post-treatment for making standard and hybrid motors cleaner and efficient, by means of a better understanding of catalysts/soot nanostructures.

### 1.3 Thesis outline

This thesis is organized as follows.

Chapter 2 presents HRTEM imaging which involves: 1) the Transmission Electron Microscopy (TEM) system, 2) the studied materials (soot and catalyst) and 3) the relation between the structures of the active phase of catalyst and their observations in the spatial and frequency domains.

Chapter 3 provides a state of the art in 1-D and 2-D statistical modelings. In particular, standard AR and FBF models are presented and their properties are highlighted.

Chapter 4 provides ARFBF and GFBF models. It also addresses parameter estimation by providing Log-RDWP and Log-RPWP regression methods.

Chapter 5 addresses the application of our proposed models to HRTEM imagery. It starts by presenting soot HRTEM texture simulation from GFBF based modeling and synthesis. Then, an application of a convolution mixture of FBF and modulated FBF is discussed for HRTEM catalyst texture synthesis. Finally ARFBF morphology analysis is applied for characterizing spectral HRTEM texture contents and clustering the HRTEM samples.

Chapter 6 provides a conclusion and draw some prospects to the work.



---

## High Resolution Transmission Electron Microscopy (HRTEM) imaging

---

In this chapter, we present the TEM system and high resolution images acquired by this system. Two sample sets will be given in the following:

- First sample set: soot images, for which we have been interested in GFBB models that are able to make synthetic soot textures generation possible from random number generators.
- Second sample set: active phases of hydrotreating catalysts, for which we have proposed an ARFBF approach allowing to discriminate different materials.

All TEM images presented in this work are produced at IFP Energie nouvelles, Physics and Analysis division, with a JEOL 2100F microscope.

## 2.1 Transmission Electron Microscopy (TEM)

### 2.1.1 Schematic description of a TEM

A TEM (see Fig. 2.1) is composed by several systems (see Fig. 2.2) which include illuminating system, specimen manipulation system, imaging system as well as vacuum system, with the following properties (see [22]).

- The illuminating system is composed by electron gun, condenser aperture and condenser lenses which include condenser lens 1 and condenser lens 2. We have the following properties:
  - condenser aperture determines the aperture of the beam and the size of the diffraction spots,
  - condenser lens 1 determines the minimum spot size on the sample,

- condenser lens 2 determines the illuminated area of the sample and the beam parallelism.
- The specimen manipulation system is composed by specimen port which has to:
  - be thin (10 – 50 nm, where ‘nm’ denotes nanometers) and representative, as well as
  - alter the incident wave function to produce a contrast (diffraction, absorption, phase, electric or magnetic polarization ...) and
  - degrade as little as possible under the beam.
- The imaging system is composed by objective lens, intermediate lens and projector lens. Diffraction lens transfers diffraction pattern or image of the object on the observation screen.
- The vacuum system provides an environment in which the electrons travel.



Figure 2.1: Transmission electron microscopy (TecnaI G2 - type of MET used in IFP Energies nouvelles). From "<https://www.fei.com/products/tem/tecnaI/?LangType=1033>".

In a TEM system, samples are usually observed at magnifications of order 250000. The resolution is limited by the data transferred by the objective lens. It ranges from about 0.1 nm to 0.3 nm. The energy of the incident electron wave ranges from 80 to 300 keV. When the incident electron wave - which can be approximated by a plane wave - penetrates the thin sample (approximately 100 nm), the coherent interaction with material inside structure undergoes Bragg scattering. The coherent interaction changes the energy and movement orientation of the incident electron. It is shown that different material structuring lead to different types of interactions.

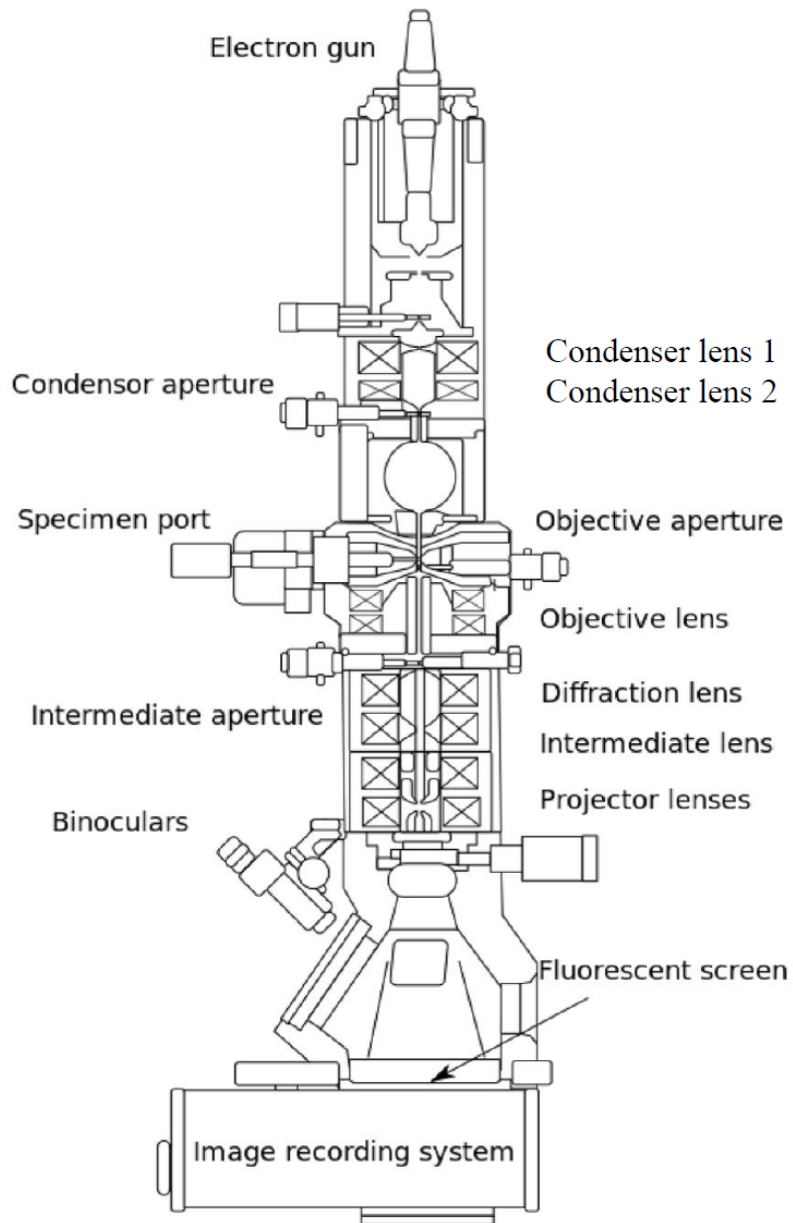


Figure 2.2: Diagram outlining the internal components of a basic TEM system. From "<https://en.wikipedia.org>".

## 2.1.2 Specimen preparation

The specimen has to comply with some requirements (see [21]) for being a relevant TEM imaging system:

- the specimen must be transparent for the electron beam, thickness of the sample viewing area should be controlled around  $100 \sim 200nm$ .
- the specimen shall be representative to truly reflect certain characteristics of the analyzed material (sample preparation must not affect these characteristics).

It is problematic to use samples with unknown compositions and thickness (see [16]). An alternative, when dealing with a sample with multiple constituent, is the Electron Energy Loss Spectroscopy (EELS) which allows for obtaining information on the elementary composition of a sample (see [15]) or the chemical environment (see [56]) at the nanometer scale.

In order to produce sufficiently thin sample blocks (thickness in a few tens of nm units) for TEM observation of catalyst support (see Fig. 2.3), transition alumina / amorphous and silica-alumina or more scarcely silica / titania are usually used as supports of catalyst sample preparation. The preparation is as follows:

- firstly, the sample is grinded in a mortar,
- then it is placed into suspension such as ethanol or heptane (sample is soluble in ethanol or heptane),
- after that, one must take one drop of suspension which is treated in an ultrasonic bath and deposit it on a copper grid coated with a holey amorphous carbon film,
- the final step consists in placing the dried grid in the microscope.

## 2.1.3 TEM imaging theory

Details concerning TEM image formation can be found in [20]. Fig. 2.4 illustrates that a part of transmitted electron  $e^-$  are selected in sample outlet of a circular opening (contrast diaphragm). Two points of sample whose diffusion properties are different (type of constituent atoms or the number of atoms with local thickness) can be discriminated. When the thickness of thin blade  $t$  is small, the interactions between the electron  $e^-$  and the sample are very limited and the slow-down of speed of  $e^-$  can be negligible. The principle of absorption contrast for specimen observation can be said "amorphous" (dense collection of  $e^-$  without special organization but with a distance between substantially equivalent nearest neighbors). This absorption contrast does not correspond to a real absorption of  $e^-$  in the samples but to a virtual absorption in the image because some  $e^-$  are blocked by the contrast aperture. If an  $e^-$  with high energy passes near an atom (see Fig. 2.5), then:

- after coulomb interactions between the negative charge of  $e^-$  incident and the charges located in the atom, the attractive or repulsive forces will slow or accelerate  $e^-$ ;

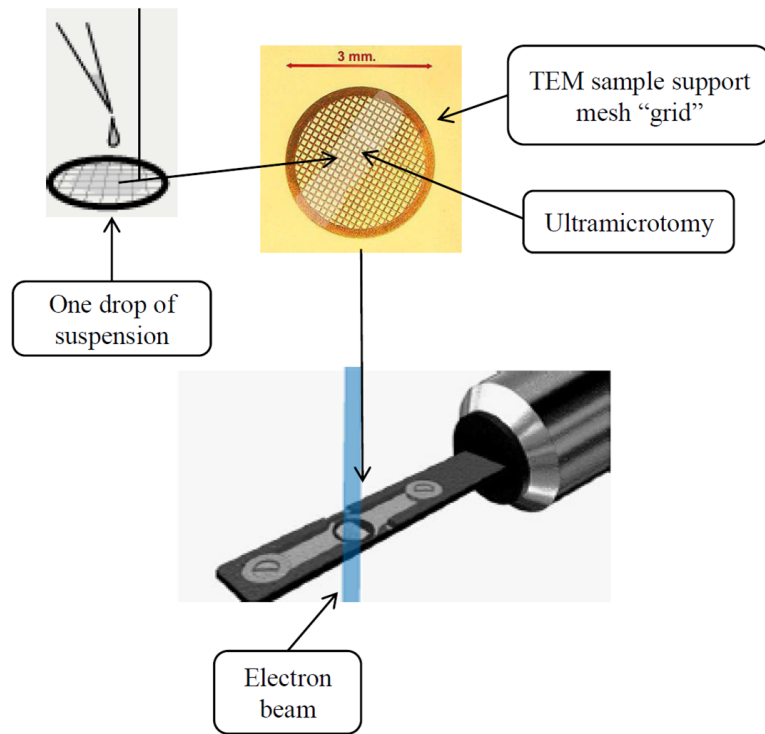


Figure 2.3: Specimen preparation.

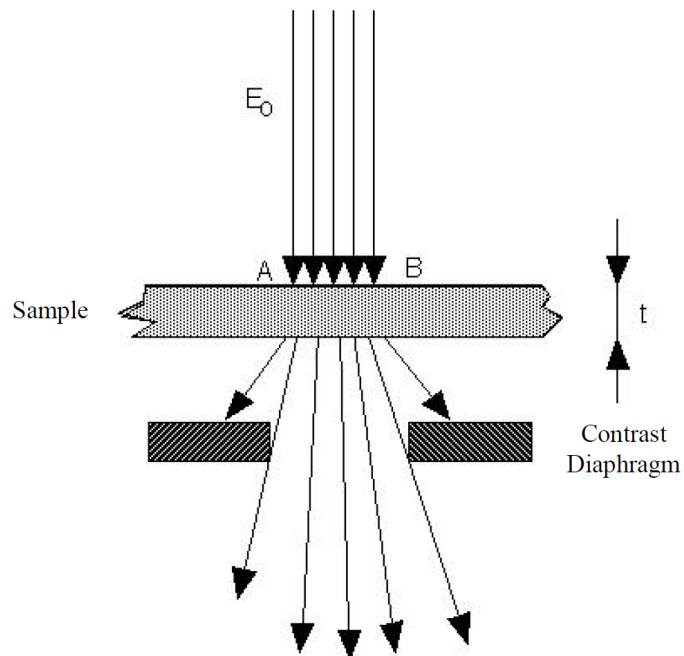


Figure 2.4: Contrast absorption introduced by the diaphragm in sample outlet.  $t$  represents the thickness of thin blade. Figure provided by [22].

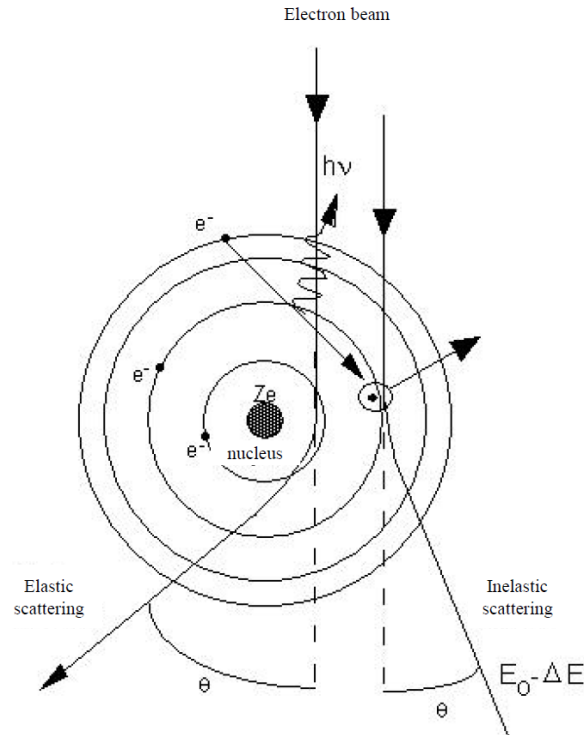


Figure 2.5: Electron  $e^-$ , elastic scattering (no energy change) with relatively large angle of deviation and inelastic scattering (energy change) with small angle of deviation.

- it is considered that the isolated atom is at rest (minimum energy state), it will acquire energy from  $e^-$ .

The  $e^-$  arriving near the nucleus undergoes attractive interaction corresponding to a strong deviation. It can be considered as an elastic scattering (no energy change) with relatively large angle of deviation ( $10^{-2}$  radians). The  $e^-$  arriving in the  $e^-$  cloud of the atom can communicate energy (for the same mass particles). Passage of  $e^-$  of the atom in a higher level, or even expulsion generates loss of energy of  $e^-$  incident. It can be considered as inelastic scattering (energy change) with small angle of deviation ( $10^{-3}$ ,  $10^{-4}$  radians). Elastic effects open a beam of initially parallel incident  $e^-$ . Inelastic effects have more complex consequences for further analysis (microscopy analysis). The size of the scattering angle is related to the density and thickness of samples, therefore it can affect the pixels of the image (lightening and/or shading different image parts). Images will be displayed on the imaging device after amplification and focus adjustment.

As mentioned above, because of different structures / different parts inside the sample, when the electron beam penetrates the sample, the energy and orientation of transmission beam change, thus the intensity of transmission is different. This irregular distribution of the intensity is called contrast. The number of  $e^-$  collected at a point of the detector  $I(x, y)$  ( $I$  is considered as one image) is different from that collected at a neighboring point  $I(x + dx, y + dy)$ . The contrast is defined as

$$C = \frac{I(x + dx, y + dx) - I(x, y)}{I(x, y)}, \quad (2.1)$$

where  $I(x, y)$  denotes a pixel of image  $I$ .

TEM has high spatial resolution and can provide rich analytic structure information. It is widely used to characterize nanostructure of materials, particularly heterogeneous catalysts (see [65]). It is possible to consider supported nanoparticles as ideal systems, because supported nanoparticles are often ideal phase objects as well as can easily be prepared and observed (see [54]). TEM exists on several forms as HRTEM, STEM (Scanning Transmission Electron Microscope), AEM (Analytical Electron Microscope)... We will explore HRTEM for visualizing soot and catalyst nanostructure in this work.

#### 2.1.4 HRTEM

HRTEM acquires an image by using a wide aperture to let the central spot and the diffracted spots closest to the diffraction pattern, in addition with observing an interference between these beams. The enlarged image shows all the crystal symmetry and periodicity properties corresponding to the cliché area of selected diffraction. The juxtaposition of aligned black and white dots with distances between rows equal the spacing in the real crystal. The enlarged image is a projection of the atomic structures.

HRTEM imaging has some limitations as follows:

- the imaged material sample must satisfy specific positioning conditions in order to avoid overlaps between adjacent columns of the atomic projections;
- the microscope must be able to resolve involved inter-atomic distances (various lens aberration issues);
- visualization on the sensors of an amplitude can suffer from loss of phase information.

The atomic columns can appear as white or black.

In practice, it's possible to resolve up to 0.2 nm between the planes. HRMET images of atomic structure only represent a certain projection of these structures (see [20]).

## 2.2 Observations of soot nanostructure by HRTEM

In the range of pollution related to transport, Diesel Particle Matter (DPM) emissions have a significant impact on global climate change by strong absorption of solar radiation in the atmosphere, and on health by penetrating through the human respiratory system. Soot are produced by the incomplete combustion of the fuels. For diesel engines, DPM emissions are limited by means of Diesel Particulate Filters (DPF). The exhaust gas is forced through porous ceramic channels walls, wherein the particles are trapped. These filters are very efficient (> 99% of efficiency) but some issues need to be solved on the regeneration procedure by the vehicles. When a soot load of several grams per liter is deposited, a regeneration of the filter has to be done by increasing temperature and causes fuel penalty. In the recent years, efforts to link soot nanostructure and re-activity have

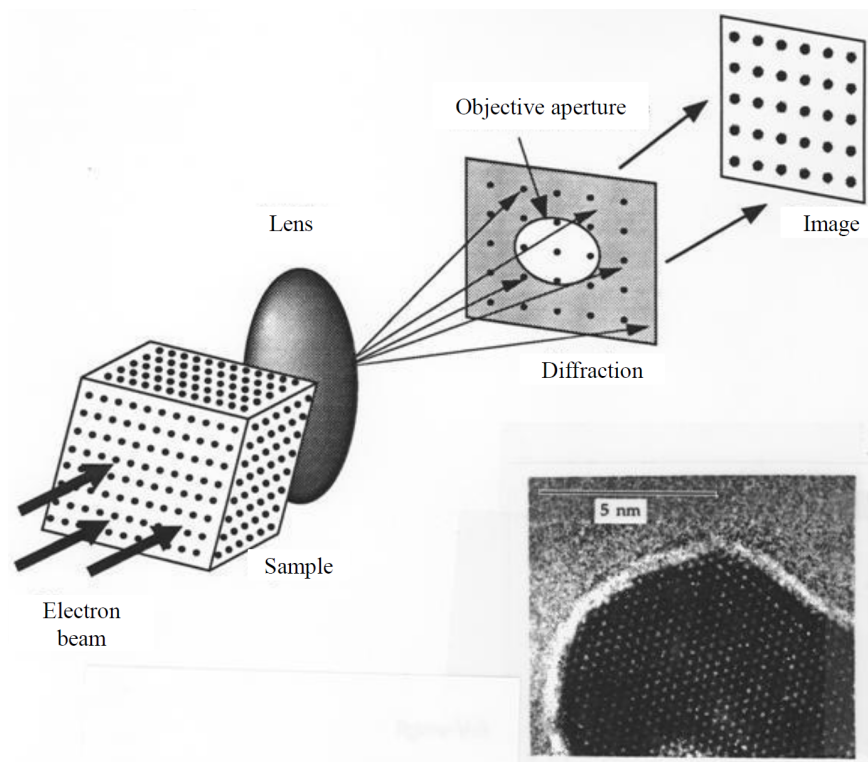


Figure 2.6: High Resolution Transmission Electron Microscope (HRTEM) imaging. From [20].

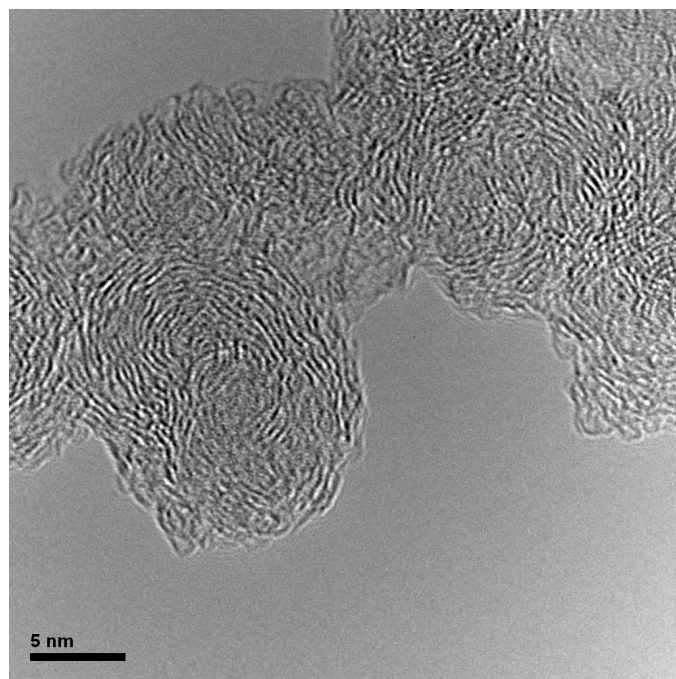


Figure 2.7: HRTEM image of soot.

been done to improve DPF regeneration and HRTEM is often used to visualize the soot nanostructure (see [112]).

A stochastic modeling based on empirical bi-variate distributions has been proposed in [75] for soot particle structure description. This model have been applied to qualitatively replicate observed particle shapes and provide quantitative improvements over older single-variable models. One model of soot particle nucleation which can predict the classical picture of soot particle inception and the classical description of soot particle structure and growth in laminar premixed hydrocarbon flames are proposed in [33]. The density of active sites which can describe surface growth depends on the chemical environment (see [33]). In flame environments, coronene ( $C_{24}H_{12}$ ) and pyrene ( $C_{16}H_{10}$ ) molecule represent the types of soot precursor molecule. A stochastic modeling "basin-hopping global optimization" was used to locate minima on the potential energy surface of the molecular clusters such that its size is similar to small soot particles. Varying soot density on this model and observing how the shape of the particle size distribution changes can inform us on the density of nascent soot. Fig. 2.7 shows an HRTEM image of soot. TEM-style projections of the resulting geometries of the molecule clusters are similar to those observed experimentally in TEM images of soot particles (see [100]).

## 2.3 Observations of active phase of hydrotreating catalysts

Catalyst is an additional substance participating in a chemical reaction and can make the reaction occur faster and/or require less activation energy. Usually, only tiny amounts are required. Because of non-consumption in the catalyzed reaction, catalysts can continue to catalyze the reaction of further quantities of reactant. Catalyst has active phase and support components. Hayden and all have demonstrated the importance of initial oxide state and particularly the active-support interactions on the final sulphided state in a way of oxidising atmosphere or 5%  $H_2S/H_2$  (at a pressure of 68 Pa) and at variable temperature (775-875 K) (see [45]). The morphology with inter-distance between two neighboring white/black fringes (active phase) is in relation to the quantity of oxygen in catalyst (see [59]). Some fringes are curved with radii of curvature as high as 2 to 5 nm (see [24]), and Iwata and all proposed that this curved property may provide default active sites (see [50]). HRTEM (High Resolution Transmission Electron Microscopy) is used as a valuable tool for imaging the crystal structure of crystalline nanomaterials such as catalyst at the atomic scale.

We are interested in the characterization of hydrotreating catalysts with sulphide phases supported on alumina (see [101]) and more specially the active phases of these catalysts. Samples are observed with Transmission Electron Microscope in bright field mode at magnification of the order of 250000. We focus on the analysis of CoMoS sites which produce alternations of black and white fringes as observed in Fig. 2.8 and Fig. 2.10. CoMoS refers to a class of active phases involving Cobalt, Molybdenum and Sulphur atomic structures. The catalytic activity and selectivity depend on the morphology of these sites (see [73] and [101]).

TEM in general has played a very important role in investigating micro-structure of catalysts. Sanders and Pollack showed that TEM was the first method to demonstrate the structure of the active phase of  $MoS_2$  in nanometric stacked lamellar sheets (see [79, 91]). Eltzner showed that STEM also demonstrated the proximity of promoters (Ni, Co) to molybdenum and tungsten (see [26]). We present here the HRTEM images and the analyzed samples of two types (X and Y) of catalysts.

### 2.3.1 HRTEM images and sub-images of catalyst X ( $Cat_X$ )

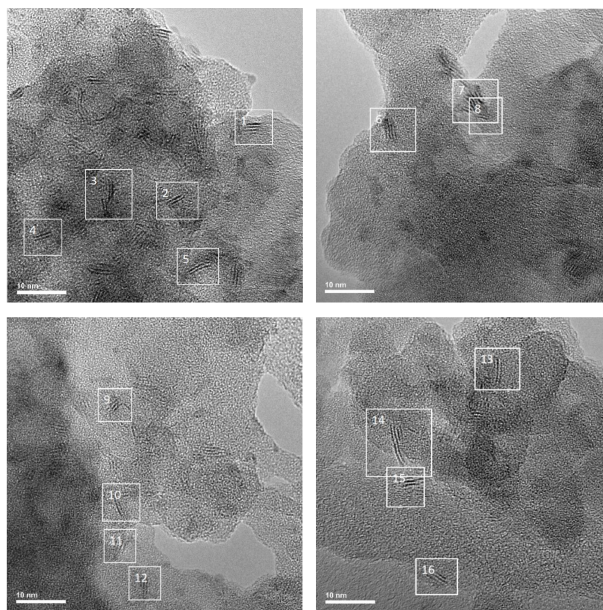


Figure 2.8: HRTEM images and sub-images of  $Cat_X$

Fig. 2.8 shows HRTEM images of Molybdenum sulfide sheets (black fringes) deposited on an alumina support for catalyst X. Several sub-images of catalyst X are given in Fig. 2.9. Each HRTEM image consists of  $1024 \times 1024$  pixels. Its numerical resolution is 0.04 nm by pixel. In this work, 93 sub-images (selected fringes) containing active phases taken from 21 HRTEM images of catalyst X are collected to form a sample database, the size of any of these 93 sub-images ranges, in pixel coordinates, between the lower bound [89; 100] and the upper bound [265; 270].

### 2.3.2 HRTEM images and sub-images of catalyst Y ( $Cat_Y$ )

Fig. 2.10 shows HRTEM images of Molybdenum sulfide sheets (black fringes) deposited on an alumina support for catalyst Y and several sub-images of this catalyst are given by Fig. 2.11. Each HRTEM image consists of  $1024 \times 1024$  pixels. Its numerical resolution is 0.04 nm by pixel. A total of 109 sub-images (selected fringes) containing active phases taken from 19 HRTEM images of catalyst Y are used as sample Y database, the size of any sub-image ranges, in pixel coordinates, between the lower bound [84; 85] and the upper bound [329; 294]. Fig. 2.12 shows an example of an HRTEM image of catalyst (left) and

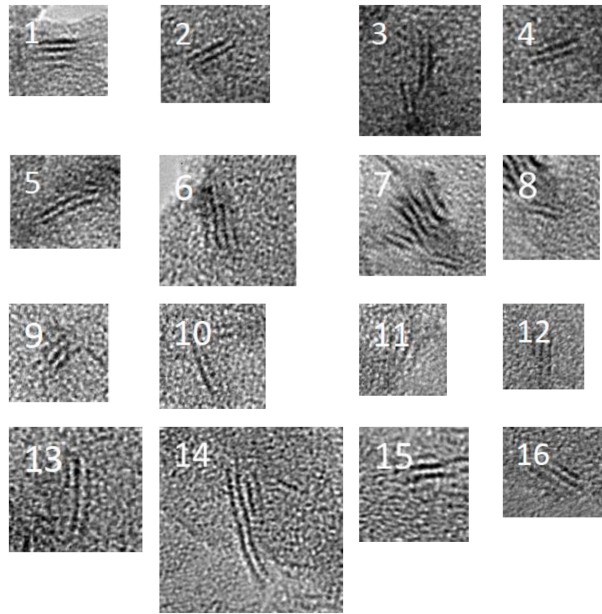


Figure 2.9: Sub-images of  $Cat_x$

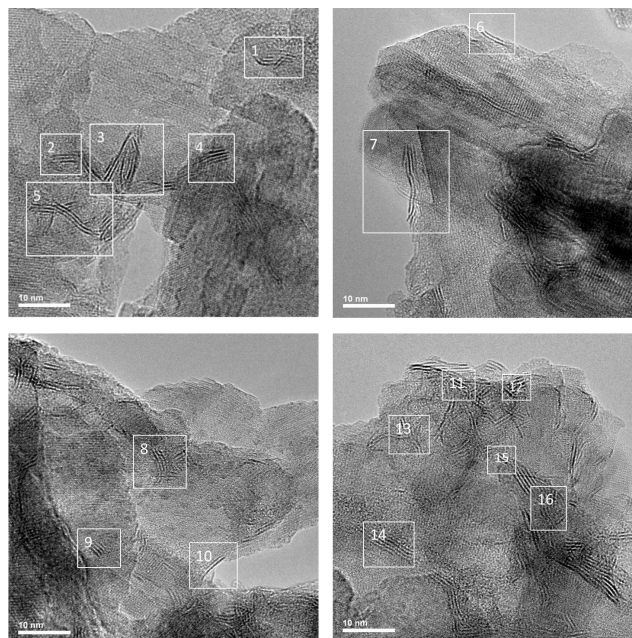


Figure 2.10: HRTEM images and sub-images of  $Cat_y$

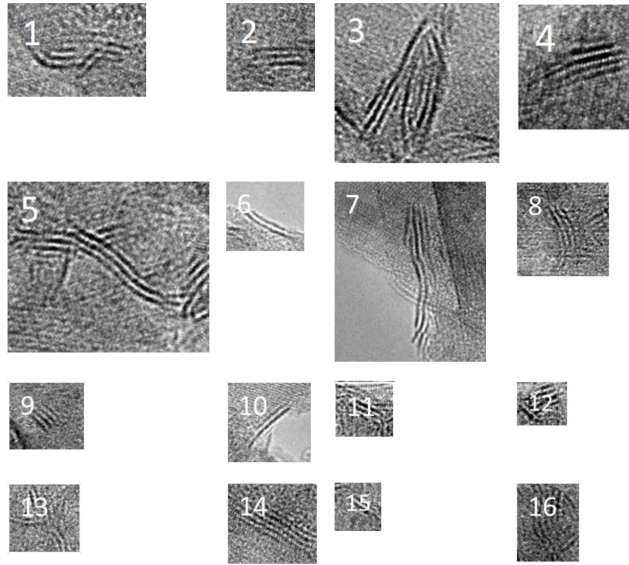


Figure 2.11: Sub-images of  $Cat_Y$

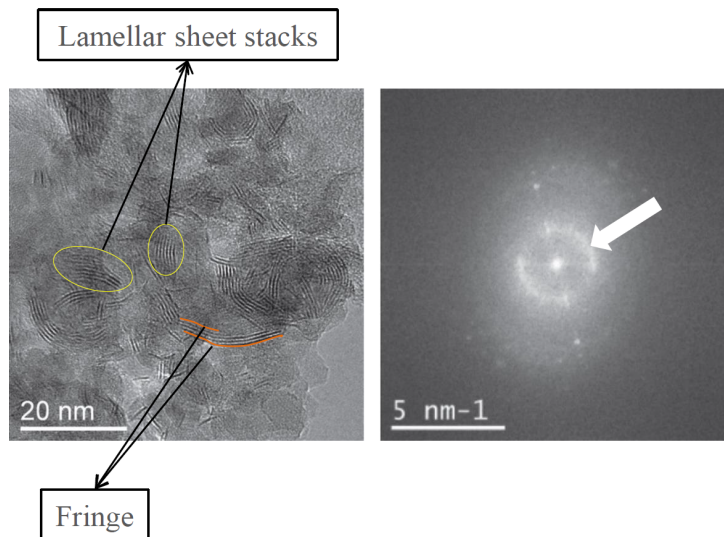


Figure 2.12: HRTEM image and its PSD, see [34].

its power spectral density (right) (see [34]). In the image, we can find clearly a number of alternations of black and white fringes with a lateral extension of a few nanometers. The stacking of the lamellar sheets in the HRTEM image has a ring (arrowed) form in the Power Spectral Density (PSD) of the image. The spatial frequency in PSD (the right image of Fig. 2.12) is at around  $1.63 \text{ nm}^{-1}$ , corresponding to a period of 0.613 nm. This period is close to the inter-distance between two neighboring white/black fringes at 0.615 nm which can be usually seen in literature (see [44]). We denote the image as  $I$ , its PSD denoted as  $S_I$  is calculated from the periodogram of the image  $I$  with size  $M \times N$  as

$$S_I(u, v) = \frac{|\hat{I}(u, v)|^2}{M \times N}, \quad (2.2)$$

where  $\hat{I}$  is the Fast Fourier Transform.

The fringe length can be defined as the lateral extension of the sheet stacks (see Fig. 2.12). Reference [17] proposed using active contour growth to measure the length of the stacks. Because of fairly thick support, slabs in an image can be in focus, over-focused or under-focused. This may induce measurement uncertainties for a stack. When the slabs are orthogonal to the beam, they are invisible, apart when moiré patterns are present, due to a crystalline support or rotation between lamellar sheets (see [83]). The quality of the slabs in HRTEM depends not only the orientation, but also the size (larger slabs, better quality). We observe numerous areas of a sample and the supports are disordered materials, with a statistical approach, we will show that these images are representative of the sample population (see Section 5.3.4).

In this work, we will study the morphology with inter-distance between two neighboring white/black fringes and the curved property of fringes (active phase) observed in Fig. 2.9 and Fig. 2.11 with some approaches based on stochastic modeling.

## 2.4 Structure of fringes (active phases) of catalyst in spatial domain and in frequency domain

An HRTEM fringe can be seen as a quasi-periodic or pseudo-periodic image pattern. As a consequence, it is expected to be represented by a peak or a lobe in the frequency domain.

Fig. 2.13 presents the ideal structure of the active phase of catalyst in spatial domain and its correspondence in frequency domain:

- When the fringes (active phases) are parallels, the form of the lobe in the corresponding power spectral density is isotropic. We have:
  - \* if the fringe inter-distance is constant, the lobe will result in a single frequency point (see (1a) in Fig. 2.13), then:
    - if the equal fringe inter-distance is small, the lobe is far from the zero frequency point (higher frequency) (see (1b) in Fig. 2.13), and

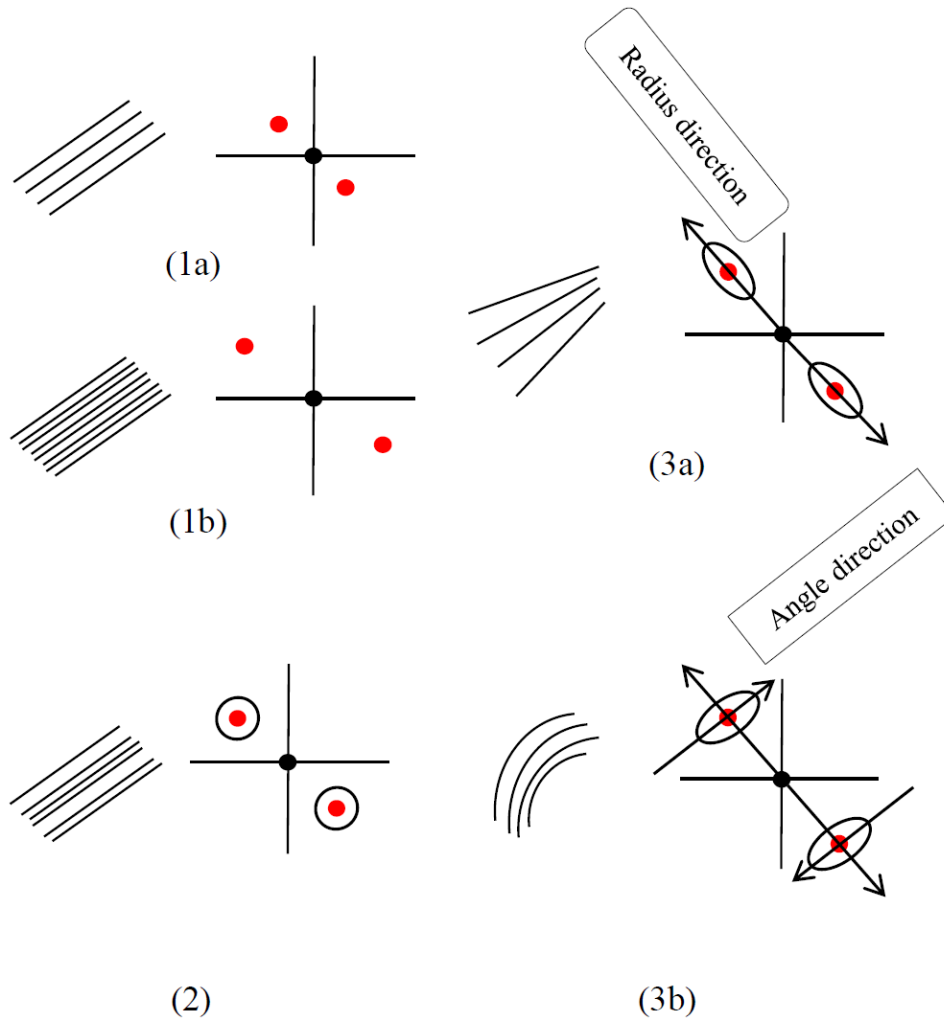


Figure 2.13: Structure of fringes: (1) parallel and constant inter-distance, (2) parallel and non-constant inter-distance and (3) non-parallel, in spatial domain as well as in frequency domain.

- if the equal fringe inter-distance is high, the lobe is near to the zero frequency point (lower frequency);
- \* if the fringe inter-distance is not constant, the lobe will be wide (see (2) in Fig. 2.13).
- When the fringes of active phase structure are not strictly parallels, the form of the lobe in its power spectral density is anisotropic (see (3) in Fig. 2.13). We have:
  - \* if the fringes possess the structure of different regular rays transmitted from the same point, the main lobe direction is parallel to the vector (central DSP/black point, center lobe/red point) and we can also denote this direction as radius direction (see (3a) in Fig. 2.13);
  - \* if the fringes possess a curve structure, the main lobe direction is perpendicular to the vector (central DSP/black point, center lobe/red point) and we can denote this direction as angle direction (see (3b) in Fig. 2.13).

A morphological characterization of these peaks/lobes in the spectral domain can allow us to obtain information about:

- inter fringes distance,
- regularity of spacing, when analyzing radial length of lobes and
- regularity of curvature, when analyzing tangential length of lobes.

This morphological characterization will be presented in Chapter 5. As it is carried out on a stochastic model-based spectrum estimation, the two next chapters will concern stochastic modeling: some generalities on stochastic modeling will be recalled in Chapter 3, whereas our contributions will be addressed in Chapter 4.



### 3.1 Introduction

This chapter addresses generalities on stochastic modeling. Definitions and properties presented in this chapter follows from the literature on stochastic processes and can be found for instance in references [27], [13, 99], [102], [68], [67], [109], [64], [90, 88, 89], [28, 29], [110, 14, 63, 96, 30, 86].

Firstly we provide description of random processes in terms of short/long memory (Section 3.2) and self-similarity (Section 3.3) properties. Then some examples of short memory /long memory / self-similar random processes are given in continuous (Section 3.4) and discrete (Section 3.5) times. Finally, extensions to 2-D random fields is addressed by focusing on Fractional Brownian and Auto-Regressive fields (Section 3.6).

### 3.2 Short versus long memory process

#### 3.2.1 Stationary processes

**DEFINITION 1** *The time series  $(X_t)_t$  is said to be strictly stationary, if*

$$F_{X_{t_1}, X_{t_2}, \dots, X_{t_n}}(x_1, x_2, \dots, x_n) = F_{X_{t_1+k}, X_{t_2+k}, \dots, X_{t_n+k}}(x_1, x_2, \dots, x_n), \quad (3.1)$$

where  $\{t_1, t_2, \dots, t_n\} \in \mathbb{Z}$ ,  $k \in \mathbb{Z}$ ,  $n \in \mathbb{Z}$ , and  $F$  denotes the cumulative joint distribution function of a set of random variables.

The terms "weakly stationary", "second-order stationary", "co-variance stationary" and "wide-sense stationary" are equivalent to describe stationarity restricted to second order statistics in situations such that

$$E(X_{t_1}) = E(X_{t_1+k}), \quad (3.2)$$

and

$$\text{Cov}(X_{t_1}, X_{t_2}) = \text{Cov}(X_{t_1+k}, X_{t_2+k}), \quad (3.3)$$

for all  $t_1, t_2, k \in \mathbb{Z}$ , the co-variances are assumed to exist.

### 3.2.2 Short memory process

**DEFINITION 2** A second-order stationary process  $(X_t)_t$  is called short memory (or short range dependence) process, if its auto-correlation function  $\rho_k$  satisfies

$$\sum_{k=0}^{\infty} \rho_k < \infty, \quad (3.4)$$

with

$$\rho_k = \frac{E[(X_t - \mu)(X_{t+k} - \mu)]}{\sigma^2},$$

where  $\mu$  and  $\sigma^2$  represent the mean and variance of the process  $X_t$ . The Auto-Regressive Moving Average (ARMA) process (see Section 3.6.2) and Auto-Regressive Conditional Heteroscedastic (ARCH) (see [27]) process are two standard short memory processes.

### 3.2.3 Long memory process

**Condition  $C_h$**  on a function  $h$  is defined as: for all  $a \in \mathbb{R}$ , when  $x \rightarrow \infty$  or  $x \rightarrow 0$ ,

$$\frac{h(ax)}{h(x)} \rightarrow 1. \quad (3.5)$$

**DEFINITION 3** A second-order stationary process  $(X_t)_t$  is called long memory process if it has an auto-correlation function  $\rho_k$  which behaves like a power function decaying to zero hyperbolically as

$$\rho_k \sim f_\rho(k)k^{-\alpha}, \quad (3.6)$$

as  $k \rightarrow \infty$ , where  $0 < \alpha < 1$ ,  $\sim$  represents the asymptotic equivalence and  $f_\rho(k)$  is a function which changes slowly to infinity and satisfying the **condition  $C_h$**  given above.

In Eq. (3.6), if  $H = 1 - \frac{\alpha}{2}$ , the long memory behavior occurs when  $\frac{1}{2} < H < 1$  (case of Hurst parameter  $H$  which will be introduced later in the manuscript).

**DEFINITION 4** In frequency domain, second-order stationary process  $(X_t)_t$  is a long memory process if its spectral density function  $S$  can be approximated by

$$S(\lambda) \sim f_S(\lambda)\lambda^{-2d}, \quad (3.7)$$

as  $\lambda \rightarrow 0^+$ , where  $0 < d < \frac{1}{2}$ ,  $f_S(\lambda)$  is a function which decays slowly to zero at frequency zero and satisfying the **condition  $C_h$** .

One can note that in the definition given above,  $\lambda \rightarrow 0^+$ ,  $\lambda^{-2d}$  is not integrable when  $d \geq \frac{1}{2}$ , thus second-order stationarity cannot be obtained in this case.

In addition, Eq. (3.7) highlights a singularity (unboundedness) of the spectral density at zero frequency. For a discrete time process, we can simply say that a process has long memory property if its spectral density is unbounded at a finite frequency point in  $[0, \pi]$ . It means that  $\exists \lambda_0 \in [0, \pi]$ , such that  $S(\lambda_0)$  is unbounded. While a process is said to be a short memory process if its spectral density is bounded for frequencies in  $[0, \pi]$ .

### 3.3 Self-similar process

Self-similarity describes certain forms of statistical dependency. The concept of long memory and that of self-similarity or asymptotical self-similarity are not equivalent (see [13]).

#### 3.3.1 Continuous time self-similar process

##### 3.3.1.1 Self-similar process in continuous time

**DEFINITION 5** A real-valued stochastic process  $X = \{X(t)\}_{t \in \mathbb{R}}$  is an  $H$  Self-Similar process (denoted as a  $H$ -SS process), if for any  $a > 0$ ,

$$\{X(at)\}_{t \in \mathbb{R}} \stackrel{D}{=} \{a^H X(t)\}_{t \in \mathbb{R}}, \quad (3.8)$$

where  $H > 0$  and " $\stackrel{D}{=}$ " means 'identical in finite-dimensional distributions'.

##### 3.3.1.2 Self-similar process with stationary increments in continuous time

**DEFINITION 6** A real-valued stochastic process  $X = \{X(t)\}_{t \in \mathbb{R}}$  is an  $H$  Self-Similar process with Stationary Increments (denoted as a  $H$ -SSSI process), if  $X$  is  $H$ -SS process and, for any  $h \in \mathbb{Z}$ ,

$$\{X(t+h) - X(h)\}_{t \in \mathbb{R}} \stackrel{D}{=} \{X(t) - X(0)\}_{t \in \mathbb{R}}, \quad (3.9)$$

where  $H > 0$ .

Let  $\{X(t)\}_{t \in \mathbb{R}}$  be an  $H$ -SSSI process with  $0 \leq H < 1$ , its increment  $X(t) - X(t-1)$  is denoted as a process  $\{I(t)\}_{t \in \mathbb{Z}}$  ( $I(t) = X(t) - X(t-1)$ ). Denote respectively by  $\gamma_X(\cdot)$  and  $\sigma^2$ , the co-variance and variance functions of  $\{X(t)\}_{t \in \mathbb{R}}$ . The  $H$ -SSSI process  $X$  has the following properties (see [13, 99]):

- $X(0) = 0$  almost surely (a.s.).
- $-X(t) \stackrel{D}{=} X(-t)$ .
- For the  $H$ -SS process  $\{X(t)\}_{t \in \mathbb{R}}$ , the process  $\{Y(t)\}_{t \in \mathbb{R}} = e^{-tH} X(e^t)$  is stationary. While  $\{Y(t)\}_{t \in \mathbb{R}}$  is stationary, the process  $X(t) = t^H Y(\ln t)$   $t > 0$  is a  $H$ -SS process.

- for  $H \in (0, 1)$ ,
  - when  $0 < H < \frac{1}{2}$ , the process  $\{I(t)\}_{t \in \mathbb{Z}}$  is a short memory process.
  - when  $H = \frac{1}{2}$ , the process  $\{I(t)\}_{t \in \mathbb{Z}}$  is uncorrelated.
  - when  $\frac{1}{2} < H < 1$ , the process  $\{I(t)\}_{t \in \mathbb{Z}}$  is a long memory process.

### 3.3.2 Discrete time self-similar process

#### 3.3.2.1 Self-similar process in discrete time

**DEFINITION 7** A discrete strictly stationary stochastic process  $\{X(t)\}_{t \in \mathbb{Z}}$  is exactly Self-Similar (abbreviation ‘SS’) (or Asymptotically Self-Similar denoted as ASS) if for all  $t$ ,

$$X(t) \stackrel{D}{=} m^{1-H} X^{(m)}(t), \quad (3.10)$$

with

$$X^{(m)}(t) = \frac{1}{m} \sum_{k=(t-1)m+1}^{tm} X(k), \quad (3.11)$$

holds for all  $m$  (or  $m \rightarrow \infty$ ) and  $k = 1, 2, \dots$ , where  $m$  indicates the level of the aggregation and  $\frac{1}{2} < H < 1$ .

#### 3.3.2.2 Second order self-similar process in discrete time

**DEFINITION 8** Let  $\{X(t)\}_{t \in \mathbb{Z}}$  be a discrete time co-variance stationary process.

- The process  $\{X(t)\}_{t \in \mathbb{Z}}$  is called exactly Second Order Self-Similar (denoted as SOSS) if  $m^{1-H} X^{(m)}(t)$  has the same auto-correlation as  $X(t)$ , for all  $m$  and for all  $t$ . Thus,

$$\text{Var}(X^{(m)}) = \text{Var}(X) m^{2H-2}, \quad (3.12)$$

and

$$\rho_k^{(m)} = \rho_k, \quad (3.13)$$

where  $\frac{1}{2} < H < 1$ ,  $m > 1$ ,  $k = 0, 1, 2, \dots$ , and the auto-correlation function  $\rho_k \sim C k^{2H-2}$ , as  $k \rightarrow \infty$ .

- The process  $\{X(t)\}_{t \in \mathbb{Z}}$  is called Asymptotically Second Order Self-Similar (denoted as ASOSS) if for  $\forall k > 0$ ,

$$\lim_{m \rightarrow \infty} \rho_k^{(m)} = \frac{1}{2} [(k+1)^{2H} - 2k^{2H} + (k-1)^{2H}]. \quad (3.14)$$

In DEFINITION 7, the exact (or asymptotical) SS concerns all the finite dimensional distributions of a strictly stationary process. In DEFINITION 8, the exact (or asymptotical) SOSS concerns only the variance and auto-correlation function of a co-variance stationary process. Under Gaussian framework, exact SOSS (respectively ASOSS) is equivalent to exact SS (respectively ASS).

From DEFINITION 8, the SOSS process  $\{X(t)\}_{t \in \mathbb{Z}}$  has the following properties:

- Its auto-correlation function  $\rho_k$  can be expressed, for  $\forall k > 0$ , as:

$$\rho_k = \frac{1}{2}[(k+1)^{2H} - 2k^{2H} + (k-1)^{2H}]. \quad (3.15)$$

- For  $\frac{1}{2} < H < 1$ , the SOSS process  $\{X(t)\}_{t \in \mathbb{Z}}$  exhibits long memory behavior (see Section 3.2.3).

### 3.3.3 Relationships between (asymptotical) self-similarity and short/long memory behaviors

With properties presented in Sections 3.2.2, 3.2.3 and 3.3, the following considers the relation between self-similarity and short memory behaviors as well as long memory behaviors.

**LEMMA 1** *Let  $\{X(t)\}$  be a co-variance stationary process, if this process is short memory as in DEFINITION 2, then it is not asymptotically second-order self-similar.*

The proof is given in [63]. This proof is based on the fact that the auto-correlation function of a short memory process decays exponentially to zero, thus it does not satisfy the condition presented in Eq. (3.15), which means that the short memory process is not ASOSS.

**LEMMA 2** *Let  $\{X(t)\}$  be a co-variance stationary process, if this process is long memory with  $\frac{1}{2} < H < 1$  as is defined in DEFINITION 3, then it is asymptotically second-order self-similar. Furthermore, under Gaussianity, the process is asymptotically self-similar.*

The proof is given in [102]. This proof is based on the fact that the auto-correlation function  $\rho_k$ , for  $\forall k = 1, 2, \dots$ , with

$$\rho_k = \frac{1}{2}[(k+1)^{2H} - 2k^{2H} + (k-1)^{2H}], \quad (3.16)$$

of a co-variance stationary long memory process decays hyperbolically, i.e.

$$\lim_{k \rightarrow \infty} \frac{\rho_k}{k^{2H-2}} = c. \quad (3.17)$$

Thus a co-variance stationary long memory process is ASOSS.

**LEMMA 3** *Let  $\{X(t)\}$  be a co-variance stationary long memory process with  $\frac{1}{2} < H < 1$ . If the spectral density of the process blows up at the origin, then the process is asymptotically second-order self-similar. Furthermore, under Gaussianity, it is asymptotically self-similar.*

The proof is a straightforward consequence of DEFINITION 4, LEMMA 2 and LEMMA 3.

## 3.4 Examples of self-similar and/or long range dependence processes in continuous time

In this section, we provide some examples of self-similar and/or long range dependence processes in continuous time.

### 3.4.1 Gaussian H-SSSI models - fractional Brownian motion

#### 3.4.1.1 Brownian motion

**DEFINITION 9** *Process  $X(t)$ , for  $t \geq 0$ , is called a (standard) Brownian motion if:*

- $X(0) = 0$  a.s (almost surely).
- $X(t)$  has independent increments.
- For each  $t$ ,  $X(t)$  has a Gaussian distribution with mean equal to zero and variance equal to  $t$ .
- $E[X(t) - X(s)] = 0$ .

The Brownian motion is a  $\frac{1}{2}$ -SS process, however, it is not a long memory process because of its independent increments. The standard deviation of the increment  $X(t+T) - X(t)$ , with  $T > 0$ , equals  $T^{\frac{1}{2}}$ .

#### 3.4.1.2 Fractional Brownian Motion (FBM)

The unique Gaussian H-SSSI model is the FBM which is presented as follows.

**DEFINITION 10** *The FBM  $X_H(t)$  is the self-similar process with parameter  $H$ , for  $0 < H < 1$  defined by the following stochastic integral:*

$$X_H(t) = \int \omega_H(t, u) dX(u), \quad (3.18)$$

where  $X(u)$  is the standard Brownian motion, the convergence of the integral is under  $L^2$ -norm with respect to the Lebesgue measure on the real numbers and the weight function  $\omega_H$  satisfying the conditions as follows:

- $\omega_H(t, u) = 0$ , for  $t \leq u$ .
- $\omega_H(t, u) = (t - u)^{H-\frac{1}{2}}$ , for  $0 \leq u < t$ .
- $\omega_H(t, u) = (t - u)^{H-\frac{1}{2}} - (-u)^{H-\frac{1}{2}}$ , for  $u < 0$ .

The following theorem is proved in [68].

**THEOREM 1** *The increments of FBM  $X_H(t)$  with parameter  $H$  are stationary and SS.*

The FBM possesses the following properties:

- The co-variance function of FBM which is denoted as  $\gamma(k)$ ,  $k \in \mathbb{Z}$ , is proportional to  $|k|^{2H-2}$  as  $k \rightarrow \infty$ .
- The spectral density of FBM is proportional to  $\omega^{-2H-1}$ , as  $\omega \rightarrow 0$  and  $0 < H < 1$ , thus the FBM exhibits long memory behavior.
- FBM can be divided into three classes:
  - when  $0 < H < \frac{1}{2}$ , FBM is called an anti-persistent process,
  - when  $H = \frac{1}{2}$ , FBM is called a random walk,
  - when  $\frac{1}{2} < H < 1$ , FBM is called a persistent process.
- FBM is a generalization of the Brownian motion.

For  $H \notin (0, 1)$ , the FBM with Hurst exponent  $H$  can be seen as moving average version of  $dX(t)$  where  $X$  denotes the Brownian motion defined above (see [68]). FBM  $X_H(t)$  can also be seen as a fractional derivative or integral of  $X(t)$  (see [109]).

Finally, one can note also that it exists some extensions of FBM (a mono-fractal process) in terms of multi-fractal (or fractional) processes by letting the Hurst parameter be itself a variable of  $t$  (instead of being a constant parameter in the case of FBM). The reader can refer to the literature [28, 29], [67] for more details.

### 3.4.2 Non-Gaussian H-SSSI models

It exists an infinite number of non-Gaussian H-SSSI models that are called  $\alpha$  stable processes for  $0 < \alpha < 2$  (see [90]). The construction of such processes starts by considering a random variable  $X$  with alpha-stable characteristic distribution:

$$\Phi(e^{i\theta X}) = \begin{cases} e^{-\sigma^\alpha |\theta|^\alpha (1 - i\beta(\text{sgn}\theta) \tan \frac{\pi\alpha}{2}) + i\mu\theta} & \text{if } \alpha \neq 1, \\ e^{-\sigma|\theta|(1 + i\beta \frac{2}{\pi}(\text{sgn}\theta) \ln |\theta|) + i\mu\theta} & \text{if } \alpha = 1, \end{cases}$$

with

$$\text{sgn}\theta = \begin{cases} 1 & \text{if } \theta > 0, \\ 0 & \text{if } \theta = 0, \\ -1 & \text{if } \theta < 0, \end{cases}$$

where  $\sigma \geq 0$ ,  $\beta \in [-1, 1]$  and  $\mu \in \mathbb{R}$ .

In general, there is no analytical close form for the probability density function  $f$  associated with  $\Phi$ . However, for  $0 < \alpha < 2$ , this probability density function,  $f$ , can be written asymptotically in  $x$  as:

$$f(x) \propto (1 + \text{sgn}(x)\beta)|x|^{-\alpha-1}.$$

Merging a set of  $\alpha$  stable random variables into a sequence, we derive a process that is distributed as  $\alpha$  stable in the sense that any finite sub-sequence can be seen as an  $\alpha$  stable distributed random vector. These processes can be used to model impulsive signals for which the Gaussian assumption used in FBM definition is far from being relevant. Some remarkable properties of these processes are:

- The relationship between Hurst parameter  $H$  and  $\alpha$  is:
  - $H \in (0, \frac{1}{\alpha}]$ , if  $0 < \alpha < 1$ ;
  - $H \in (0, 1]$ , if  $1 < \alpha < 2$ .
- When  $0 < \alpha < 2$  and  $H \neq \frac{1}{\alpha}$ , the linear fractal stable motion (or linear fractal Lévy motion) is considered.
- When  $0 < \alpha < 2$  and  $H = \frac{1}{\alpha}$ , the  $\alpha$ -stable Lévy motion is considered.
- When  $1 < \alpha < 2$ , the log-fractional stable motion is  $\frac{1}{\alpha}$ -SSSI process.
- An  $\alpha$ -stable process is said to be symmetric (and called S $\alpha$ S) if for  $\forall \theta \in \mathbb{R}$  and  $\sigma \geq 0$ :

$$\Phi(e^{i\theta X}) = e^{-\sigma^\alpha |\theta|^\alpha}.$$

- Three famous Symmetric  $\alpha$ -Stable (S $\alpha$ S)  $H$ -SSSI processes are:
  - the linear fractional stable motion,
  - the real harmonically fractional stable motion and
  - the sub-Gaussian fractional motion.

These three S $\alpha$ S  $H$ -SSSI processes reduce to FBM if  $\alpha = 2$ .

The relationship between SS process, Gaussian process, Brownian motion, FBM,  $\alpha$ -stable process and Lévy process (see [90, 88, 89]) can be presented as:

- A SS and Gaussian process is a FBM.
- A SS and Lévy process is an  $\alpha$ -stable process.
- A Gaussian and Lévy process is a Brownian motion with drift.
- Brownian motion is a particular case of SS processes, Gaussian processes and Lévy processes.

### 3.5 Examples of self-similar and short/long range dependence processes in discrete time

In this section, we present some discrete time stochastic processes and their SS / long memory / short memory properties.

### 3.5.1 FGN process

The first level of construction of discrete time random models is to consider discrete sampling of continuous time processes. This sampling can be followed by summations or differencing operations. For instance, the Fractional Gaussian Noise (FGN) is the discrete time process  $\{X(t)\}_{t \in \mathbb{Z}}$  defined by

$$X(t) = X_H(t) - X_H(t-1), \quad (3.19)$$

where  $\{X_H(t)\}_{t \in \mathbb{R}}$  is a fractional Brownian motion (see Section 3.4.1). FGN is the increment sequence of the FBM process. Its properties are detailed as follows [68]:

- FGM is an exactly SS stationary Gaussian process with mean equal to zero.
- The FGN is the unique exactly SS stationary Gaussian process.

The second level of random process model construction is considering discrete time recursive equations between random variables. The widest class of random processes constructed by this way include both short memory and long memory terms, in addition with fractional integration/differencing terms. It is called  $k$ -factor GARMA (Gegenbauer Auto-Regressive Moving Average) process (see [110, 38]) and it includes many standard discrete time processes, as highlighted below.

### 3.5.2 $k$ -factor GARMA process

**DEFINITION 11** *The  $k$ -factor Gegenbauer Auto-Regressive Moving Average (GARMA) process  $\{X(t)\}_{t \in \mathbb{Z}}$  is defined by the recursive equation:*

$$\Phi_L W_L (X_t - c) = \Theta_L \epsilon_t, \quad (3.20)$$

with

$$W_L = \prod_{i=1}^k (1 - 2u_i L + L^2)^{d_i}, \quad (3.21)$$

where

- $L$  is the lag operator, also called back-shift operator, defined as  $L^k X_t = X_{t-k}$ ;
- $\Phi_L$  and  $\Theta_L$  are two polynomial functions of degree  $p$  and  $q$ , respectively, defined as:  $\Phi_L = \sum_{i=1}^p \phi_i L^i$  and  $\Theta_L = \sum_{j=1}^q \theta_j L^j$ ;
- $c$  is the expectation of  $X_t$  (often assumed to equal 0);
- $\epsilon_t, \epsilon_{t-1} \dots$  are zero-mean white noise error terms with variance  $\sigma_\epsilon^2$ ;
- $k$  is the number of unbounded peaks at the frequencies  $f_i = \frac{\cos^{-1} u_i}{2\pi}$ ,  $i \in \{1, \dots, k\}$ ,  $k$  being a finite positive integer and the parameters  $f_i$  are called Gegenbauer frequencies, these parameters are associated with the long-memory behavior of the model;
- $u_i$  is the periodicity parameter specifying the frequency where the long-memory behavior occurs;

- $d_i$  ( $d_i \in \mathbb{R}$ ) is the fractional difference parameter, it indicates how slowly the auto-correlation damps;
- $(1 - 2u_iL + L^2)^{-d_i}$  is the generating function of Gegenbauer polynomials  $C_n^d(u)$  which is defined as

$$(1 - 2u_iL + L^2)^{-d_i} = \sum_{n=0}^{\infty} C_n^{d_i}(u_i)L^n, \quad (3.22)$$

where  $d \neq 0$ ,  $u$  is in the interval  $[-1, 1]$ ,  $C_n^d(u)$  is given by

$$C_n^{d_i}(u_i) = \sum_{j=0}^{\lfloor \frac{n}{2} \rfloor} \frac{(-1)^j (2u_i)^{n-2j} \Gamma(d_i - j + n)}{j!(n-2j)! \Gamma(d_i)} \quad (3.23)$$

with  $\lfloor \frac{n}{2} \rfloor$  being the largest integer less than or equal to  $\frac{n}{2}$ , and  $\Gamma$  is the special gamma function (see [30]).

### 3.5.2.1 Properties

The main characteristics of the  $k$ -factor GARMA model can be summarized as follows (see proofs in [110, 14, 63, 96, 30, 86]):

- $X_t$  is stationary (DEFINITION 1): if all the roots of the equation  $\Phi_L = 0$  lie outside the unit circle and  $d_i < \frac{1}{2}$  when  $u_i \neq 1$  or  $d_i < \frac{1}{4}$  when  $|u_i| = 1, i = 1, \dots, k$ .
- Stationary  $X_t$  is long memory (see DEFINITION 3): if  $d_i > 0$ .
- The spectral density of the  $k$ -factor GARMA:

$$S(\omega) = \sigma^2 \frac{|\Theta(e^{-j\omega})|^2}{|\Phi(e^{-j\omega})|^2} \prod_{i=1}^k \{4[\cos(\omega) - u_i]\}^{-d_i}. \quad (3.24)$$

- A  $k$ -factor GARMA process is co-variance stationary and exhibits long memory behavior when
  - $u_i$  are distinct,
  - all the roots of the polynomials  $\Phi_L$  and  $\Theta_L$  are distinct and outside the unit circle,
  - and
    - \* if  $0 < d_i < \frac{1}{2}$  and  $|u_i| < 1$  or
    - \* if  $0 < d_i < \frac{1}{4}$  and  $|u_i| = 1$  for  $i = 1, 2, \dots, k$ .
- Under the co-variance stationary and long memory conditions given just above, the  $k$ -factor GARMA process is second-order asymptotically self-similar. Furthermore, under Gaussian framework, it is asymptotically self-similar.

We present here two particular cases of  $k$ -factor GARMA process as follows:

- When  $k = 1$ ,  $k$ -factor GARMA process reduces to a Gegenbauer ARMA (GARMA) process (see [40]).
- When  $k = 1$  and  $u = 1$ ,  $k$ -factor GARMA process reduces to a Fractional Integrated ARMA (ARFIMA) process (see [39, 46]).
- When  $k = 1$ ,  $u = 1$ ,  $\Phi_L = 1$  and  $\Theta_L = 1$ ,  $k$ -factor GARMA process reduces to a Fractional Integrated (FI) process (see [46]).

Let us pay a particular attention to the ARFIMA and the FI processes in the two following sub-sections.

### 3.5.2.2 ARFIMA process

The stochastic ARFIMA process with parameters  $(p, d, q)$   $\{X_t\}$  is an extension of fractional differencing FI ( $d$ ) with Box-Jenkins methods ARMA  $(p, q)$ .

**DEFINITION 12** *The ARFIMA  $(p, d, q)$  process  $\{X_t\}$  is defined by*

$$\Phi_L \nabla^d X_t = \Theta_L \epsilon_t, \quad (3.25)$$

where  $\Phi_L$  and  $\Theta_L$  are polynomials in the backward-shift operator  $L$ ,  $\Phi_L = 1 - \phi_1 L - \dots - \phi_p L^p$  and  $\Theta_L = 1 - \theta_1 L - \dots - \theta_q L^q$ ,  $p, q$  are integers,  $d$  is real and

$$\begin{aligned} \nabla^d &= (1 - L)^d \\ &= \sum_{k=0}^{\infty} C_d^k (-L)^k \\ &= 1 - dL - \frac{1}{2}d(1-d)L^2 - \frac{1}{6}d(1-d)(2-d)L^3 - \dots, \end{aligned} \quad (3.26)$$

where  $d$  is real non-integer.

The ARFIMA process is flexible enough to explain both the short-term and certain long-term correlation structure of a series (see [49, 60, 105, 104, 106]). On distant observations, the effect of parameter  $d$  describes the hyperbolic decay of high-lag correlation structure, while the effects of  $\Phi$  and  $\Theta$  describe the exponential decay of low-lag correlation structure. On very distant observations, the effects of  $\Phi$  and  $\Theta$  will be negligible.

FI and ARMA can be considered as two particular cases of ARFIMA:

- FI ( $d$ ) can be also noted as ARFIMA  $(0, d, 0)$  and
- ARMA  $(p, q)$  can be also noted as ARFIMA  $(p, 0, q)$ .

We present here some properties of ARFIMA  $(p, d, q)$  process:

- Stationarity (DEFINITION 1): all the roots of the equation  $\Phi_L = 1 - \phi_1 L - \dots - \phi_p L^p = 0$  lie outside the unit circle ( $d < \frac{1}{2}$ ).

- Power Spectral density (*PSD*):

$$S_X(\omega) = |2 \sin(\frac{\omega}{2})|^{-2d} S_{ARMA}(\omega), \quad (3.27)$$

with

$$S_{ARMA}(\omega) = \frac{\sigma_E^2 |\Theta(e^{j\omega})|^2}{2\pi |\Phi(e^{j\omega})|^2}, \quad (3.28)$$

and

$$\lim_{\omega \rightarrow 0} \frac{\omega}{2 \sin(\frac{\omega}{2})} = 1, \quad (3.29)$$

where  $0 < d < \frac{1}{2}$ . Thus, as  $\omega \rightarrow 0$ ,

$$S_X(\omega) \approx \frac{\sigma_W^2 |\Theta(1)|^2}{2\pi |\Phi(1)|^2} |\omega|^{-2d} = S_{ARMA}(0) |\omega|^{-2d}. \quad (3.30)$$

where  $S_{ARMA}(\omega)$  is the *PSD* of ARMA process controlling the short-range dependence of the process,  $\Phi(e^{j\omega})$  is the AR polynomial with order  $p$  and  $\Theta(e^{j\omega})$  is the MA polynomial with order  $q$ . Similarly to FBM, ARFIMA has an infinite value peak in the spectrum at  $\omega = 0$ .

### 3.5.2.3 FI process

**DEFINITION 13** *FI* ( $d$ ) process  $X_t$  is defined by

$$X_t = \nabla^{-d} \epsilon_t, \quad (3.31)$$

or

$$\nabla^d X_t = \epsilon_t. \quad (3.32)$$

where  $\epsilon_t$  are independent identically distributed random variables with mean zero and variance  $\sigma_\epsilon^2$  and  $\nabla^d$  is the fractional-differencing operator defined by Eq. (3.26).

We present here some properties of the FI process (see [12, 95] for details). FI ( $d$ ) process (we assume for convenience that  $\sigma_\epsilon^2 = 1$ ) is such that:

- $-\frac{1}{2} < d < 0$ : short memory and anti-persistent,
- $d = 0$ : white noise with zero correlations and constant spectral density,
- $0 < d < \frac{1}{2}$ : long-memory stationary process or self-similar,
- $d < \frac{1}{2}$ : stationary,
- $d = \frac{1}{2}$ : non-stationary.

Power Spectral Densities:

- for  $0 < \omega \leq \pi$  and  $-\frac{1}{2} < d < \frac{1}{2}$ ,

$$S_X(\omega) = (2 \sin \frac{\omega}{2})^{-2d}, \quad (3.33)$$

- for  $0 < d < \frac{1}{2}$ ,

$$S_X(\omega) \sim \omega^{-2d}, \quad (3.34)$$

$S_X(\omega)$  is a decreasing function of  $\omega$ , as  $\omega \rightarrow 0$ ,  $S_x(\omega) \rightarrow \infty$ .

- for  $-\frac{1}{2} < d < 0$ ,  $S_x(\omega)$  is an increasing function of  $\omega$  and vanishes at  $\omega = 0$ .

Co-variance function, for  $-\frac{1}{2} < d < \frac{1}{2}$ :

$$\gamma_u = E(X_t X_{t-u}) = \frac{(-1)^u (-2d)!}{(u-d)! (-u-d)!}. \quad (3.35)$$

Correlation function:

- for  $u = 0, \pm 1, \dots$ ,

$$\rho_u = \frac{\gamma_u}{\gamma_0} = \frac{(-d)!(u+d-1)!}{(d-1)!(u-d)!}, \quad (3.36)$$

- for  $u = 1, 2, \dots$ ,

$$\rho_u = \frac{d(1+d)\dots(u-1+d)}{(1-d)(2-d)\dots(u-d)}, \quad (3.37)$$

- as  $u \rightarrow \infty$ ,

$$\rho_u \sim \frac{(-d)!}{(d-1)!} u^{2d-1}, \quad (3.38)$$

with

$$\gamma_0 = \frac{(-2d)!}{[(-d)!]^2}, \quad (3.39)$$

and

$$\rho_1 = \frac{d}{1-d}. \quad (3.40)$$

The long-term persistency ( $d > 0$ ) implies an hyperbolic decay of the correlation function.

To conclude this review of 1-D random processes, one can mention another class of dependency modeling, the one involved by Markov chains. A brief description of these models can be found in [41].

## 3.6 2-D stochastic modeling

In this section, we present some 2-D random field extensions for certain random processes described in the previous sections. The 2-D stochastic fields considered are: the FBF (Fractional Brownian Field) and the ARMA (Auto-Regressive Moving Average) field. A presentation of other classes of random fields such as 2-D Markov models can be found in [23, 35, 108].

### 3.6.1 2-D isotropic FBF modeling

The Fractional Brownian Field (FBF) is the 2-D extension of FBM (see Section 3.4.1). Isotropic FBF is a one-parameter model extension of FBM. Its parameter is also called *Hurst parameter*, as for FBF. In the 2-D case, this parameter is representative of stochastic regularity (texture roughness, in practice). The isotropic FBF admits one pole located at zero frequency in spectral domain.

**DEFINITION 14** *The 2-D isotropic FBF with Hurst parameter  $H$ ,  $0 < H < 1$ , denoted here as  $B_H(x, y)$ , is defined to be a non-stationary Gaussian zero-mean real-valued field with auto-correlation function defined as*

$$\begin{aligned} \rho_{B_H}(x, y, s, t) &= E[B_H(x, y)\overline{B_H(s, t)}] \\ &= \frac{\sigma_b^2}{2}\{(x^2 + y^2)^H + (s^2 + t^2)^H - ((x - s)^2 + (y - t)^2)^H\} \end{aligned} \quad (3.41)$$

where  $(s, t) \in \mathbb{Z}^2$  and  $\sigma_b^2$  is a constant representing the variance of a white Gaussian noise.

Although FBF is a non-stationary process, this random process has stationary-increments and stationary wavelet projections (see [78]).

The spectrum of FBF can then be defined by association with respect to the above stationary FBF instances and is given by (see [78, 48, 84, 11]):

$$\begin{aligned} S_{FBF}(u, v) &= \xi(H) \frac{1}{(u^2 + v^2)^{H+1}} \\ &= \xi(H) \frac{1}{\|(u, v)\|^\alpha}, \end{aligned} \quad (3.42)$$

with

$$\alpha = 2H + 2, \quad (3.43)$$

where  $\|(u, v)\| = \sqrt{u^2 + v^2}$ ,

$$\xi(H) = \frac{2^{-(2H+1)}\pi^2\sigma_b^2}{\sin(\pi H)\Gamma^2(1 + H)}$$

and  $\Gamma$  is the standard gamma function.

Fig. 3.1 shows that the Hurst parameter represents the stochastic regularity (texture roughness). When Hurst parameter is bigger, the texture seems to be observed closer. In Fig. 3.1, the size of image synthesized from FBF are equal to  $512 \times 512$ .

### 3.6.2 2-D ARMA, AR, MA modeling

Let us define a second-order stationary random field as  $A = \{A(x, y)\}$ ,  $(x, y) \in \mathbb{Z}^2$ .

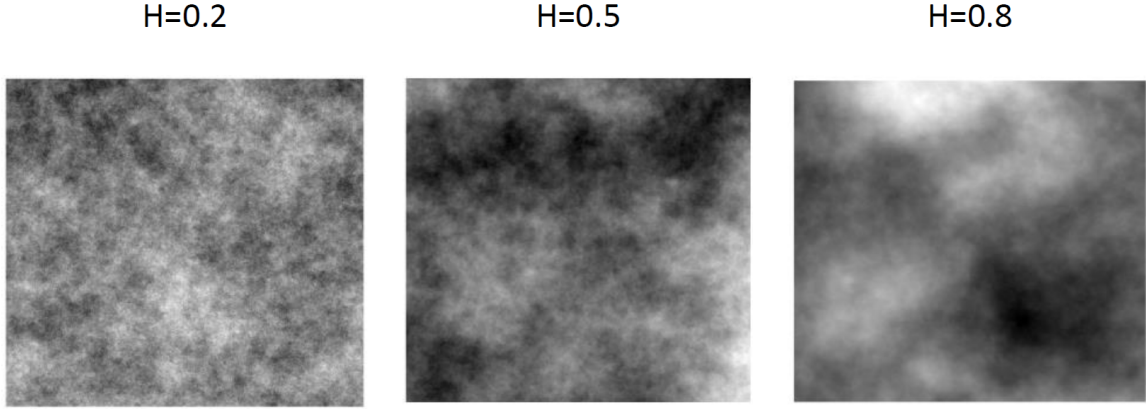


Figure 3.1: FBF texture samples for different Hurst parameters  $H$  ( $H \in \{0.2, 0.5, 0.8\}$ ).

**DEFINITION 15** *Field  $A$  is a 2-D ARMA process (see [2, 3]) if*

$$\begin{aligned} A(x, y) &+ \sum_{(m_1, m_2) \in D_o} a_{(m_1, m_2)} A(x - m_1, y - m_2) \\ &= b_{0,0} E(x, y) + \sum_{(m_1, m_2) \in D_i} b_{(m_1, m_2)} E(x - m_1, y - m_2), \end{aligned} \quad (3.44)$$

where

- $D_i$  and  $D_o$  are the prediction supports associated with the input and output respectively. Subsequently, we assume that the supports of the input and output match  $D_i = D_o = D$ .
- $E$  is an independent identically distributed process with zero mean (centered) and variance equal to 1.
- $\{a_{(m_1, m_2)}\}_{(m_1, m_2) \in D}$  and  $\{b_{(m_1, m_2)}\}_{(m_1, m_2) \in D}$  are 2-D transverse coefficients of ARMA.

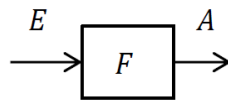


Figure 3.2: Linear time invariant system.

Field  $A$  can be seen as the output of a linear time invariant system with transformation  $F$  when  $E$  is the entry (see Fig. 3.2). When we apply 2-D  $z$ -transform (see [80]) to Eq. (3.44), the filter transfer function is expressed in the form of a 2-D rational function of polynomials in  $z_1$  and  $z_2$ :

$$F(z_1, z_2) = \frac{\Phi(z_1, z_2)}{\Psi(z_1, z_2)}, \quad (3.45)$$

with

$$\Phi(z_1, z_2) = b_{0,0} + \sum_{(m_1, m_2) \in D} b_{m_1, m_2} z_1^{-m_1} z_2^{-m_2}, \quad (3.46)$$

and

$$\Psi(z_1, z_2) = a_{0,0} + \sum_{(m_1, m_2) \in D} a_{m_1, m_2} z_1^{-m_1} z_2^{-m_2}. \quad (3.47)$$

The PSD (see [18, 111]) of ARMA process  $A$  is then expressed as:

$$S_A(u, v) = \frac{|\Phi(e^{j2\pi u}, e^{j2\pi v})|^2}{|\Psi(e^{j2\pi u}, e^{j2\pi v})|^2}. \quad (3.48)$$

For models whose predictive support is finite, polynomials  $\Psi$  and  $\Phi$  are with finite degree. We now present various geometries of prediction support that were most commonly used for the ARMA (resp. AR, MA) model.

We present two particular cases (AR and MA) in ARMA as follows.

### 3.6.2.1 AR model

**DEFINITION 16**  $A$  is considered as an AR when  $b_{m_1, m_2} = 0, \forall (m_1, m_2) \in D$ . Thus the AR is defined as:

$$A(x, y) = - \sum_{(m_1, m_2) \in D} a_{m_1, m_2} A(x - m_1, y - m_2) + b_{0,0} E(x, y). \quad (3.49)$$

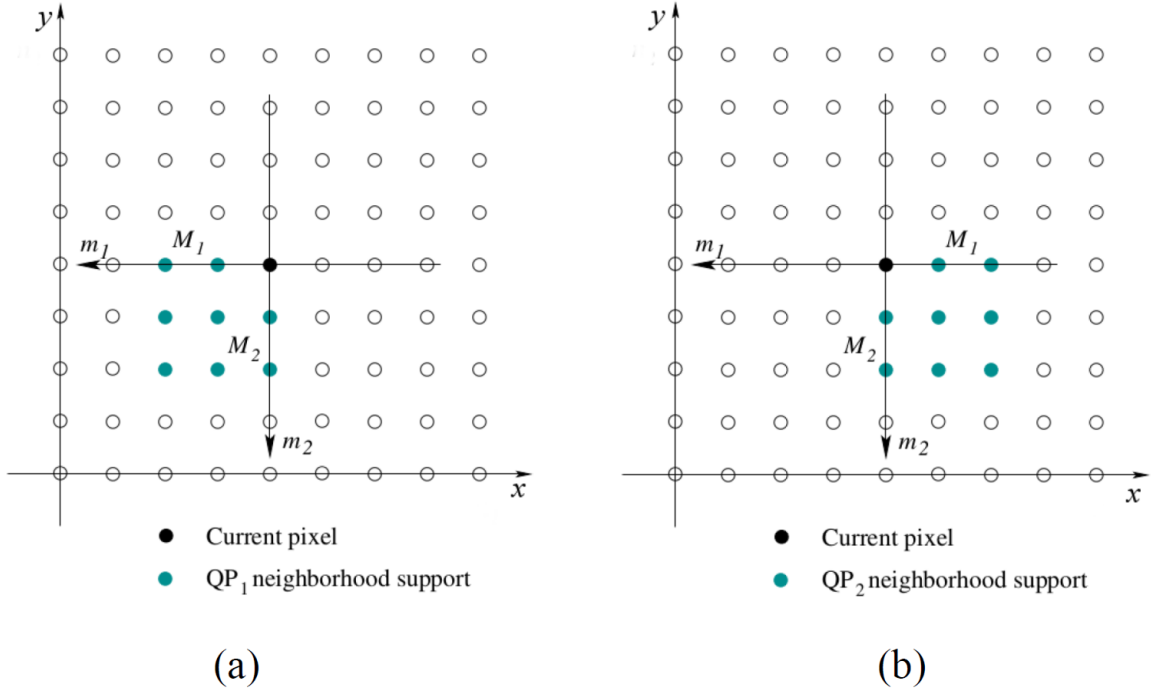


Figure 3.3: Quarter plan prediction supports denoted (a)  $D_{QP_1}$  (see Eq. (3.50)) and (b)  $D_{QP_2}$  (see Eq. (3.51)) with finite order  $(M_1, M_2) = (2, 2)$  and  $(x, y) \in \mathbb{Z}^2$ .

Different prediction supports have been defined in [6] and can be presented as follows.

$$D_{QP_1} = \{0 \leq m_1 \leq M_1, 0 \leq m_2 \leq M_2\} \setminus (0, 0), \quad (3.50)$$

$$D_{QP_2} = \{-M_1 \leq m_1 \leq 0, 0 \leq m_2 \leq M_2\} \setminus (0, 0), \quad (3.51)$$

$$D_{QP_3} = \{-M_1 \leq m_1 \leq 0, -M_2 \leq m_2 \leq 0\} \setminus (0, 0), \quad (3.52)$$

and

$$D_{QP_4} = \{0 \leq m_1 \leq M_1, -M_2 \leq m_2 \leq 0\} \setminus (0, 0), \quad (3.53)$$

where  $(M_1, M_2)$  is the 2-D AR order.

In this work, we will use two prediction supports with Quarter Plan (QP) forms respectively denoted  $QP_\ell, \ell = 1, 2$  (Fig. 3.3 shows an illustrative example of these QPs). The 2-D AR Power Spectral Density (PSD),  $S_{AR}(u, v)$ , is then derived as the harmonic

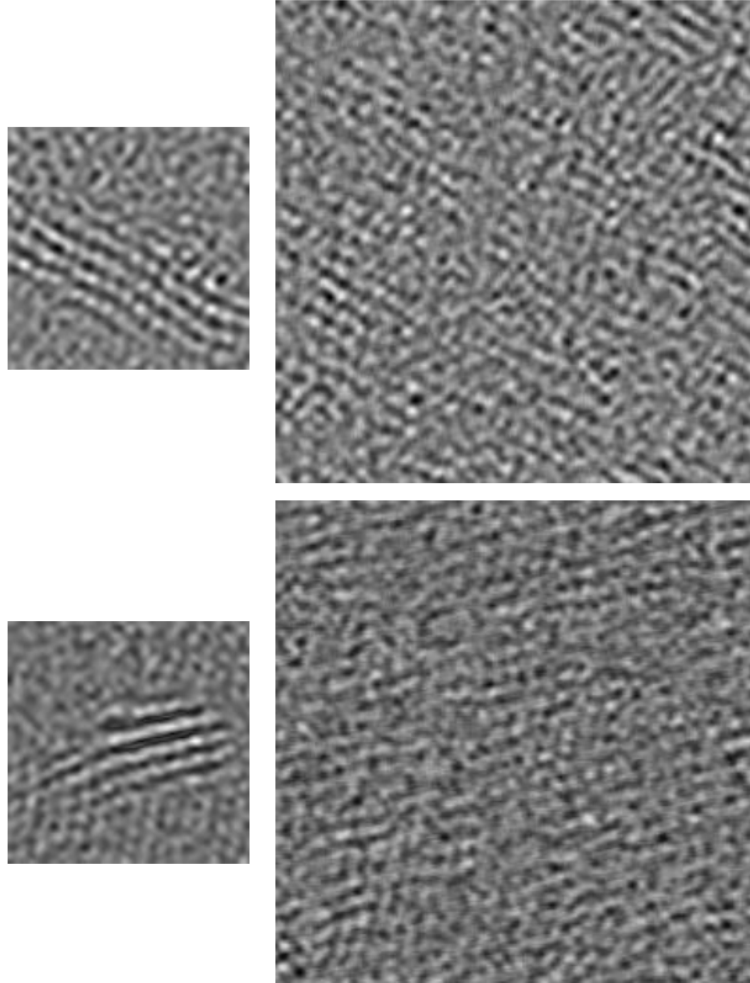


Figure 3.4: Each row presents an original image with its corresponding synthesized image from the corresponding AR model.

mean of the two spectra associated with prediction supports  $QP_\ell, \ell = 1, 2$ , (see [51]):

$$S_{AR}(u, v) = \frac{2S_{QP_1}(u, v)S_{QP_2}(u, v)}{S_{QP_1}(u, v) + S_{QP_2}(u, v)}, \quad (3.54)$$

where

$$S_{QP_\ell}(u, v) = \frac{\sigma_{e,\ell}^2}{|F_{QP_\ell}(u, v)|^2} \quad (3.55)$$

and

$$F_{QP_\ell}(u, v) = 1 + \sum_{m=(m_1, m_2) \in D_{QP_\ell}} a_{m,\ell} e^{-i2\pi u m_1} e^{-i2\pi v m_2}.$$

The 2-D spectrum estimated from this method is easy to compute and has good estimation properties with respect to the other existing methods, see [4] for details.

Let us denote the set of AR parameters associated with  $QP_\ell$ ,  $\ell \in \{1, 2\}$ , as

$$\theta_{M_1, M_2}^{QP_\ell} = \{\sigma_{e,\ell}^2, \{a_{m,\ell}, m \in D_{QP_\ell}\}\}. \quad (3.56)$$

At a fixed order, the parameters of  $\theta_{M_1, M_2}^{QP_\ell}$ ,  $\ell \in \{1, 2\}$ , are estimated thanks to minimization in the least-squares sense, see [82, 3]. This procedure involves Yule-Walker equations and it is equivalent to the maximum likelihood estimation, when the random variables are Gaussian.

In practice, the selection of an accurate prediction support determines model performance. Although a number of works focus on the order  $(M_1, M_2)$  selection, see references [6, 1] among others, this work considers, from preliminary experimental model validation,  $M_1 = M_2 = 10$  as the order of the prediction support.

Fig. 3.4 presents two examples of images synthesized by AR. In each row, an original image is presented at left and its corresponding AR-synthesized image is placed at the right of the row. Fig. 3.1 shows that structures of the original images have the same directions as the fringes observed the synthesized images. These structures are in connection with the lobes which constitute the AR power spectral density features (see [51]).

### 3.6.2.2 MA model

Field  $A$  given by Eq. (3.44) is an MA when  $a_{m_1, m_2} = 0$ ,  $\forall (m_1, m_2) \in D$ . Thus, we have

**DEFINITION 17** *An MA field  $A$  is defined by:*

$$A(x, y) = b_{0,0}E(x, y) + \sum_{(m_1, m_2) \in D} b_{m_1, m_2} E(x - m_1, y - m_2). \quad (3.57)$$

The set of coefficients in MA is the set  $\{b_{m_1, m_2}\}_{(m_1, m_2) \in D}$ .

### 3.6.2.3 Causality

There exists several strategies for selecting AR/MA/ARMA predicting support, [62]. Example of a causal (respectively semi-causal, non-causal) prediction support is given by Fig. 3.5 (respectively Fig. 3.6, Fig. 3.7). In Fig. 3.5, Fig. 3.6 and Fig. 3.7, the supports  $D_{NSHP}$ ,  $D_{SC}$ ,  $D_{NC}$  are defined by:

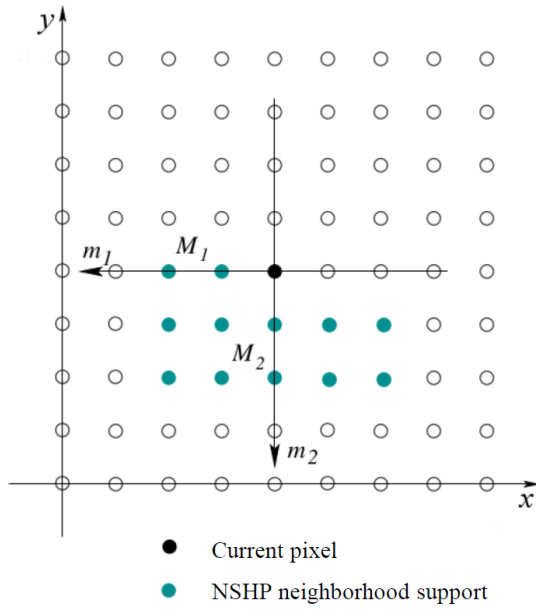


Figure 3.5: Causal Non Symmetric Half Plan (NSHP) prediction support  $D_{NSHP}$ ,  $(m_1, m_2) \in \mathbb{Z}^2$  and  $(x, y) \in \mathbb{Z}^2$ .

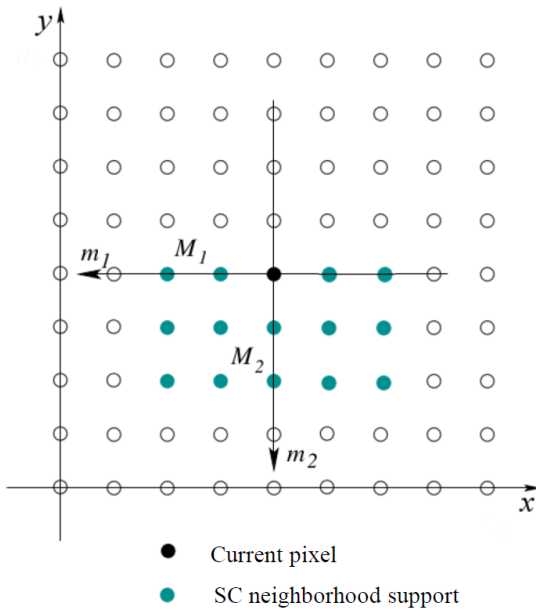


Figure 3.6: Semi-Causal (SC) prediction support  $D_{SC}$ ,  $(m_1, m_2) \in \mathbb{Z}^2$  and  $(x, y) \in \mathbb{Z}^2$ .

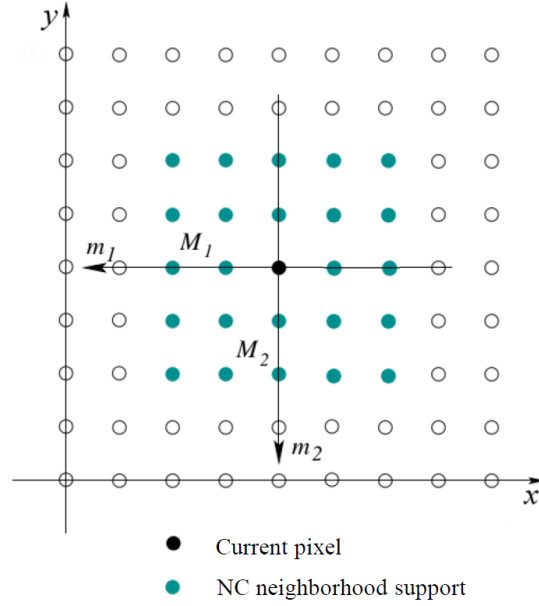


Figure 3.7: Non-Causal (NC) prediction support  $D_{NC}$ ,  $(m_1, m_2) \in \mathbb{Z}^2$  and  $(x, y) \in \mathbb{Z}^2$ .

- [causal]

$$D_{NSHP} = \left\{ (m_1, m_2) \in \mathbb{Z}^2 \left/ \begin{array}{l} -M_1 \leq m_1 \leq M_1, \quad 1 \leq m_2 \leq M_2, \\ 1 \leq m_1 \leq M_1, \quad m_2 = 0 \end{array} \right. \right\}, \quad (3.58)$$

- [semi-causal]

$$D_{SC} = \{(m_1, m_2) \in \mathbb{Z}^2 / -M_1 \leq m_1 \leq M_1, 0 \leq m_2 \leq M_2, (m_1, m_2) \neq (0, 0)\}, \quad (3.59)$$

- [non-causal]

$$D_{NC} = \left\{ (m_1, m_2) \in \mathbb{Z}^2 \left/ \begin{array}{l} -M_1 \leq m_1 \leq M_1, \\ -M_2 \leq m_2 \leq M_2, \end{array} (m_1, m_2) \neq (0, 0) \right. \right\}. \quad (3.60)$$

In practice, the selection of a specific prediction support may depend on the application, see for instance [32, 70], [61], [53, 82], [42], [55, 116].

Comparing for instance Figs. 2.9 and 2.11 with Fig. 3.1 and Fig. 3.4, the model presented in this chapter visually provide simulations close to fringes observed on HRTEM images. We have proposed in this thesis, some new families of parametric models exploiting the insightful, respectively short and long memory properties of AR and FBF fields. These models are presented in the next chapter.

---

## 2-D G-AR-FBF modeling and parameter estimation

---

The contributions proposed in this chapter concern both modeling and parameter estimation issues. For modeling, we propose two extensions of the isotropic FBF. The first extension is a framework integrating 2-D AR and 2-D FBF into a new model called ARFBF. The integration is made by means of convolution operations on discrete sequences of random variables. This model is presented in Section 4.1. The second extension proposed involves convolutions of several FBFs and is called  $K$ -factor GFBF: this model is presented in Section 4.2. Both extensions require concise parameter estimation on small samples. For this purpose, we propose in Section 4.3 a new Hurst parameter estimation method that exploits polar averaging on wavelet packet spectral densities.

### 4.1 2-D Auto-Regressive Fractional Brownian Field

Why a combination of AR and Fractional Brownian Fields ?

The first reason is that 2-D AR random fields are powerful tools for modeling the dependencies in a small pixel neighborhood and, as such, can be considered as relevant short-range correlation structure descriptors. AR field modeling has shown relevancy for describing a wide class of pseudo-periodic textures and has been exploited in [7, 2, 69, 94] for different applications such as classification, segmentation and recognition of textural information. The spectrum of 2-D AR model can be calculated by the Harmonic Mean (HM) method (see [51, 5]).

The second reason is that FBF describes in essence long-range correlation structures. The Hurst exponent of FBF is also representative of stochastic regularity and can be used to describe texture roughness. The spectral characterizations of FBF can be found in [78, 48, 77, 84, 11].

The ARFBF model is built for the sake of exploiting both complementary short-range

and long-range dependencies. In this respect, it is constructed so as to behave as either 2-D AR (when long-range dependencies are not observed) or FBF (when short-range dependencies can be neglected). However, it is more general than a binary selection among 2-D AR or FBF: it involves, in addition with these fields, a wide range of fields showing both strong local dependencies together with exponential spectral decays.

#### 4.1.1 ARFBF Definition and Spectral Characterization

The 2-D ARFBF (see [98]) is defined as the convolution of AR field  $A$  (see Section 3.6.2.1) and isotropic FBF  $B_H$  (see Section 3.6.1). This 2-D ARFBF, hereafter denoted  $Z(x, y)$ , is defined as follows:

$$Z(x, y) = (A * B_H)(x, y). \quad (4.1)$$

In particular,

- $Z$  behaves as an FBF when AR is a white noise;
- $Z$  is an AR when FBF is a white noise ( $H = 0$ ).

From Eq. (7.1), the spectrum associated with the non-stationary ARFBF model is

$$S_{ARFBF}(u, v) = S_{AR}(u, v)S_{FBF}(u, v). \quad (4.2)$$

where  $S_{AR}$  is the AR spectrum defined by Eq. (3.54) and  $S_{FBF}$  is the FBF spectrum given by Eq. (3.42).

The 2-D ARFBF parameter estimation can be performed in a joint framework by using directly  $S_{ARFBF}$ . However, knowing that the pseudo-periodic textural information we seek is well-localized in frequency and can be dissociated from texture roughness, we propose performing a separable parameter estimation of:

- the Hurst parameter associated with FBF near zero-frequency (under assumption that the periodicity tacked by AR is located far from zero-frequency) and
- the set of AR parameters from the procedure described in Section 3.6.2.1, after FBF contribution removal.

Due to this spectral based separable approach, the ARFBF modeling steps of an image  $I_1$  can be summarized by the following procedure.

### 4.1.2 ARFBF modeling procedure

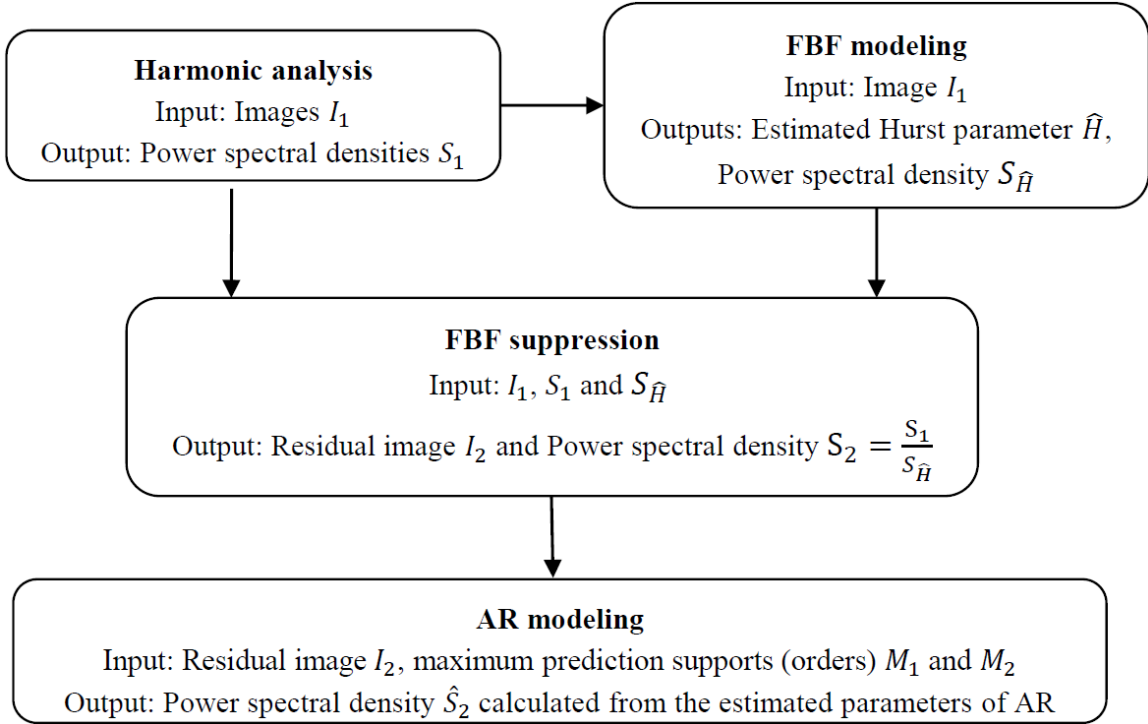


Figure 4.1: Procedure of ARFBF modeling.

ARFBF modeling procedure is illustrated by the block diagram of Fig. 4.1. Let us denote now one input image as  $I_1$ . The ARFBF modeling procedure of this image is detailed as follows:

- First step: calculate the spectrum  $S_1$  of  $I_1$  by using Harmonic analysis or by using the wavelet packet method of [8].
- Second step: estimate, by using the Log-RPWP method presented in Section 4.3.4, the parameter  $H$  and thus  $S_{\hat{H}}$  is derived.
- Third step: remove the contribution of the FBF in  $I_1$ . The residual part is denoted as  $I_2$  and its spectrum denoted as:

$$S_2(u, v) = \frac{S_1(u, v)}{S_{\hat{H}}(u, v)}. \quad (4.3)$$

- Final step, model the residual part  $I_2$  by the 2-D AR and calculate its PSD  $\hat{S}_2$  from the AR estimated parameters ( $\hat{S}_2$  is a smoothed version of  $S_2$  in general).

## 4.2 2-D $K$ -factor Generalized Fractional Brownian Fields

### 4.2.1 2-D $K$ -GFBF modeling

In this section, we present a Generalized Fractional Brownian Fields (GFBF) model [11] based on convolution of modulated fractional Brownian fields. From now on,  $B_{H_0}$  denotes a standard Fractional Brownian Field (Section 3.6.1).

#### 4.2.1.1 Modulated Fractional Brownian Field $B_{H_q}$

The spectrum of  $B_{H_0}$  admits a pole at the zero frequency point (see Eq. (3.42)). The field  $B_{H_0}$  can be modulated so as to translate its pole at a frequency point  $(u_q, v_q) \in [0, \pi] \times [0, \pi]$ . This yields a random field  $B_{H_q}$  (modulated version of standard FBF  $B_{H_0}$ ) that can be written in the form:

$$B_{H_q}(t, s) = e^{iu_q t} e^{iv_q s} B_{H_0}(t, s). \quad (4.4)$$

The random field  $B_{H_q}$  is centered and its auto-correlation function,

$$R_{B_{H_q}}(t, s, x, y) = E[B_{H_q}(t, s) \overline{B_{H_q}(x, y)}], \quad (4.5)$$

is

$$R_{B_{H_q}}(t, s, x, y) = R_{B_{H_0}}(t, s, x, y) e^{iu_q(t-x)} e^{iv_q(s-y)}. \quad (4.6)$$

where  $0 < H_q < 1$ .

This auto-correlation function involves a stationary separable exponential term multiplying  $R_{B_{H_0}}$ . Note, from the expansion of  $R_{B_{H_q}}$  given in Eq. (4.6), that  $B_{H_q}$  is non-stationary: its auto-correlation function involves contributions that cannot reduce to lag terms  $(t - x, s - y)$ .

Similarly to  $B_{H_0}$ , one can associate the spectrum  $S_{B_{H_q}}$  to  $B_{H_q}$ , where

$$S_{B_{H_q}}(u, v) = S_{B_{H_0}}(u - u_q, v - v_q), \quad (4.7)$$

thus:

$$\begin{aligned} S_{B_{H_q}}(u, v) &= \xi(H_q) \frac{1}{((u - u_q)^2 + (v - v_q)^2)^{H_q+1}} \\ &= \xi(H_q) \frac{1}{\|((u - u_q), (v - v_q))\|^{2H_q+2}}, \end{aligned} \quad (4.8)$$

where

- $\|((u - u_q), (v - v_q))\| = \sqrt{(u - u_q)^2 + (v - v_q)^2},$

- 

$$\xi(H_q) = \frac{2^{-(2H_q+1)} \pi^2 \sigma_b^2}{\sin(\pi H_q) \Gamma^2(1 + H_q)},$$

- $\sigma_b^2$  is a constant representing the variance of a white Gaussian noise and
- $\Gamma$  is the special gamma function.

From Eq. (4.8), the spectrum  $S_{B_{H_q}}$  is unbounded near frequency point  $(u_q, v_q)$  (spectral pole with unit norm). This spectral pole is a shifted version of the pole of  $S_{B_{H_0}}$ . In the neighborhood of  $(u_q, v_q)$ , the spectrum  $S_{B_{H_q}}$  has the same exponential decay as  $S_{B_{H_0}}$  around zero.

#### 4.2.1.2 Generalized Fractional Brownian Fields $B_{G_{H_K}}$ with $K$ spectral poles

The standard fractional Brownian field  $B_{H_0}$  admits one spectral pole located at zero frequency point. Its modulated version,  $B_{H_q}$ , admits one spectral pole located at frequency  $(u_q, v_q)$ . The generalization to  $K$  spectral poles performed in [11] concerns the number of poles associated with the spectral density of the fractional Brownian field.

Consider a sequence of Hurst parameters  $H_k \in \{H_0, H_1, H_2, \dots, H_Q\}$  and define a convolution (notation  $\otimes$ , [52]) of  $K$  non-stationary fields  $B = \{B_{H_k}, k = 0, 1, \dots, Q\}$ :

$$B_{G_{H_K}} = \bigotimes_{k=0}^Q B_{H_k}, \quad (4.9)$$

where

- sequence  $B_{H_k}$  is assumed to be composed with independent random fields,
- $\{k = 0, 1, \dots, Q\}$  and  $K = Q + 1$ .

Random field  $B_{G_{H_K}}$  is the so-called  $K$ -factor Generalized Fractional Brownian Fields (GFBF).

From some straightforward calculus involving some properties of the convolution operators, the spectrum of  $B_{G_{H_K}}$ , noted as  $S_{B_{G_{H_K}}}$ , can be written as:

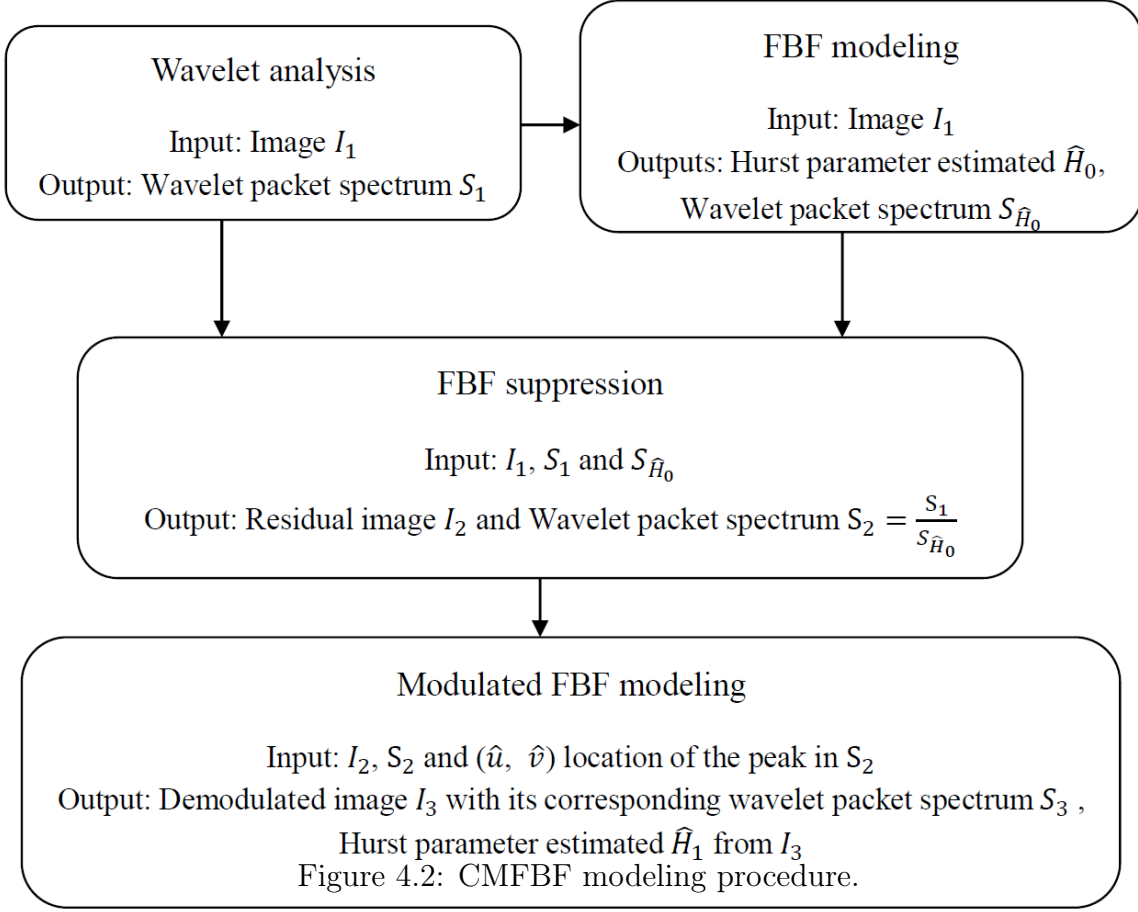
$$S_{B_{G_{H_K}}}(u, v) = \prod_{k=0}^Q \frac{\prod_{k=0}^Q \xi(H_k)}{((u - u_q)^2 + (v - v_q)^2)^{H_k+1}}, \quad (4.10)$$

where

- $$\xi(H_k) = \frac{2^{-(2H_k+1)} \pi^2 \sigma_b^2}{\sin(\pi H_k) \Gamma^2(1 + H_k)},$$
- $\sigma_b^2$  is a constant representing the variance of a white Gaussian noise and
- $\Gamma$  is the special gamma function.

From Eq. (7.4), the GFBF is associated with a spectrum admitting several poles and those poles are not necessarily at the zero of the frequency grid. By construction, the 2-D  $K$ -factor generalized fractional Brownian fields model can admit an arbitrary number of spectral singularity points and Hurst parameters which characterize local exponential decays of the spectrum in several pixel neighborhoods.

#### 4.2.1.3 A particular sub-class of GFBF: the CMFBB



The CMFBB (Convolution Mixture of 2-D FBF and 2-D modulated FBF) is a 2-factor GFBF  $Y(x, y)$  defined by the convolution between a standard FBF  $B_{H_0}$  and a modulated FBF  $B_{H_1}$  (see Eq. (4.4)):

$$Y = B_{H_0} \otimes B_{H_1}, \quad (4.11)$$

We recall that  $B_{H_0}$  admits a spectral pole located at frequency  $(0, 0)$  (see Eq. (3.42)) and  $B_{H_1}$  involves a spectral pole located at  $(u_1, v_1)$  (see Eq. (4.8)). As a consequence, the spectrum  $S_Y$  of  $Y$ ,

$$\begin{aligned} S_Y(u, v) &= S_{B_{H_0}}(u, v) S_{B_{H_1}}(u, v) \\ &= \frac{\xi(H_0)}{(u^2 + v^2)^{H_0+1}} \frac{\xi(H_1)}{((u - u_1)^2 + (v - v_1)^2)^{H_1+1}}, \end{aligned} \quad (4.12)$$

admits two spectral poles: those located at frequencies  $(0, 0)$  and  $(u_1, v_1)$  respectively (we assume that  $(u_1, v_1) \neq (0, 0)$ ).

Under the assumption that  $(u_1, v_1)$  is not closed to  $(0, 0)$ , estimation of CMFBB parameters can be reduced to 2 estimations of FBF parameters close to the frequencies of interest, namely  $(u_1, v_1)$  and  $(0, 0)$ . The estimation of the Hurst parameter is given in Section 4.3. The procedure for associating a CMFBB model to a texture image  $I_1$  is illustrated by Fig. 4.2. It involves the following steps:

- First step, calculate the spectrum  $S_1$  of  $I_1$  by using the wavelet packet method of [8].
- Second step, estimate, by using the Log-RPWP method presented in Section 4.3.4, the parameter  $H_0$  and thus  $S_{\hat{H}_0}$  is derived.
- Third step, remove the contribution of the FBF in  $I_1$ . The residual part is denoted as  $I_2$  and its spectrum denoted as:

$$S_2(u, v) = \frac{S_1(u, v)}{S_{\hat{H}_0}(u, v)}. \quad (4.13)$$

- Final step, model the residual part  $I_2$  as a modulated FBF, then derive the estimated location  $(\hat{u}, \hat{v})$  and estimated Hurst parameter  $\hat{H}_1$ .

### 4.3 Hurst parameter estimation of 2-D FBF

As highlighted in Section 4.1 and Section 4.2 above, estimation of ARFBF and GFBF parameters can be performed locally in the spectral domain, by applying log-regression in the neighborhood of every pole. The limited number of samples forces us to reconsider FBF estimation procedure in a context of small samples.

Several methods exist for estimating the Hurst parameter of the 2-D Fractional Brownian Field (FBF), for instance, maximum likelihood estimates (see [97, 31]), box-counting approach (see [47]) and log-periodogram methods (see [37, 85]). These estimators have shown relevancy mainly for large sample sizes.

In this section we propose two extensions of the wavelet packet method of [10] (dedicated to fractional Brownian motion Hurst parameter estimation) for the sake of estimating FBF parameters. These extensions, based on 2-D wavelet packet spectrum, are called *Log-Regression on Diagonal Wavelet Packet spectrum* (Log-RDWP) and *Log-Regression on Polar representation of Wavelet Packet spectrum* (Log-RPWP).

They will be shown more relevant than standard estimators [97] for robust Hurst parameter estimation.

#### 4.3.1 Log-RDWP estimation method

The Log-RDWP estimation method [98] is based on the wavelet packet spectrum. In the case of 2-D separable wavelets, it exists three different regression lines (horizontal, vertical and diagonal regression lines) allowing to estimate the Hurst parameter  $H$  or spectrum decay parameter  $\alpha$  (see Eq. (3.43)).

In this work, the estimation method Log-RDWP uses the diagonal regression line and relies on the following formula:

$$\hat{\alpha}_{Log-RDWP} = \frac{1}{C} \sum_{j,k} \frac{\log \hat{S}(u_j, u_j) - \log \hat{S}(u_k, u_k)}{\log \|(u_k, v_k)\| - \log \|(u_j, v_j)\|}, \quad (4.14)$$

where

- $C = \frac{N!}{2(N-2)!}$  is the number of all possible combinations of the log-ratios,
- $\hat{S}$  (here  $\hat{S}_{FBF}$ ) denotes the spectrum estimated from the method proposed in [10],
- $N$  is the number of considered frequencies in two dimensions,
- $0 < j < k \leq N$ ,
- $\|(u_k, v_k)\| = \sqrt{u_k^2 + v_k^2}$  and
- $\|(u_j, v_j)\| = \sqrt{u_j^2 + v_j^2}$ .

### 4.3.2 Log-RPWP estimation method

Log-RPWP Hurst parameter estimation method [98] consists of three steps.

- In the first step, the spectrum with polar coordinates  $S_p$  is computed as,

$$S_p(r, \theta) = T(\hat{S}_{FBF}(u, v)), \quad (4.15)$$

where  $\hat{S}_{FBF}(u, v)$  is the wavelet packet spectrum ([8]), in Cartesian coordinates  $(u, v)$ , estimated from FBF samples and  $T$  is the Cartesian-to-polar transform.

- In the second step, averages are done over the angles:

$$S_p(r_i) = \frac{1}{J} \sum_{j=1}^J S_p(r_i, \theta_j), \quad (4.16)$$

with  $1 \leq i \leq N$  denoting the radial sampling index.

- In the third step, Hurst parameter  $H$  is estimated by:

$$\hat{H}_{RPWP} = \frac{1}{2C} \sum_{\substack{1 \leq i, k \leq N \\ i < k}} \frac{\log S_p(r_i) - \log S_p(r_k)}{\log r_k - \log r_i} - 1, \quad (4.17)$$

thus spectrum decay parameter  $\alpha$  (see Eq. (3.43)) can be obtained by

$$\hat{\alpha}_{RPWP} = \frac{1}{C} \sum_{\substack{1 \leq i, k \leq N \\ i < k}} \frac{\log S_p(r_i) - \log S_p(r_k)}{\log r_k - \log r_i}, \quad (4.18)$$

where  $C = \frac{N!}{2(N-2)!}$  is the number of all possible combinations of indices  $(i, k)$  such that  $0 < i < k \leq N$ .

### 4.3.3 Results of Hurst parameter estimation

In order to evaluate the performance of the Log-RDWP and Log-RPWP estimation methods, we generate 10 realizations of an FBF for  $\alpha \in \{2.4, 2.8, 3.2, 3.6\}$  and for two different image sizes:  $512 \times 512$  and  $2048 \times 2048$ .

$RDWP_N$  and  $RPWP_N$  mean that  $\alpha$  is estimated by Log-RDWP method and Log-RPWP method respectively, where  $N$  is the number of samples (see Eq. (4.14) and Eq. (4.18)). We use the Daubechey filter for computing the WP spectrum (see [10]). The results given in Tab. 4.1 and Tab. 4.2 are obtained with a level of decomposition equal to 7. The

Size Image	512*512							
	2,4		2,8		3,2		3,6	
Real Value								
Estimated	$\alpha$	Var( $\alpha$ )						
RDWP_8	1,781	0,145	2,132	0,160	2,651	0,424	3,236	0,292
RDWP_12	2,186	0,038	2,553	0,086	2,993	0,053	3,553	0,090
RDWP_16	1,833	0,039	2,293	0,031	2,772	0,044	3,343	0,039
RDWP_20	2,197	0,039	2,612	0,007	3,035	0,030	3,542	0,037
RDWP_24	2,145	0,045	2,688	0,019	3,050	0,019	3,510	0,018
RDWP_28	2,074	0,021	2,693	0,011	3,066	0,010	3,483	0,025
RDWP_32	1,935	0,009	2,523	0,007	2,987	0,025	3,400	0,014
RDWP_64	1,778	0,008	2,487	0,006	2,936	0,006	3,433	0,002
RPWP_8	2,649	0,026	3,133	0,056	3,594	0,081	4,138	0,023
RPWP_12	2,501	0,017	2,947	0,035	3,398	0,029	3,895	0,010
RPWP_16	2,486	0,004	2,948	0,016	3,435	0,018	3,942	0,003
RPWP_20	2,441	0,004	2,906	0,007	3,363	0,008	3,860	0,003
RPWP_24	<b>2,377</b>	0,002	2,875	0,005	3,335	0,006	3,799	0,002
RPWP_28	2,322	0,002	2,844	0,003	3,312	0,005	3,767	0,002
RPWP_32	2,282	0,001	<b>2,819</b>	0,002	<b>3,298</b>	0,004	3,746	0,001
RPWP_64	1,842	0,001	2,544	0,001	3,081	0,001	<b>3,584</b>	0,001

Table 4.1: Mean values of estimated  $\hat{\alpha}$  and their variances computed from 10 FBF realizations with image size equal to  $512 \times 512$ .

mean square error (denoted as MSE) is computed as:

$$MSE(\hat{\alpha}) = Bias(\hat{\alpha})^2 + Var(\hat{\alpha}), \quad (4.19)$$

with

$$Bias(\hat{\alpha}) = \alpha - \hat{\alpha}, \quad (4.20)$$

where  $Var$  means the variance of estimated  $\alpha$  in 10 FBF realizations. Tab. 4.1 and Tab. 4.2 show that, for the small size images, the Log-RPWP method estimates the parameter  $\alpha$  better than the Log-RDWP method. For the images with a large size, the Log-RDWP method gives comparable results to those of the Log-RPWP method. Fig. 4.3 gives one example by using MSE to demonstrate the stability of Log-RPWP method. In this work, we use Log-RPWP method to estimate the Hurst parameter of FBF model.

Size Image	2048*2048							
	2,4		2,8		3,2		3,6	
Real Value	$\alpha$	Var( $\alpha$ )						
Estimated	$\alpha$	Var( $\alpha$ )						
RDWP_8	2,308	0,023	<b>2,801</b>	0,035	3,190	0,029	3,727	0,014
RDWP_12	2,482	0,004	2,949	0,013	3,337	0,009	3,833	0,005
RDWP_16	2,241	0,004	2,748	0,008	<b>3,193</b>	0,007	3,642	0,001
RDWP_20	<b>2,401</b>	0,010	2,898	0,009	3,329	0,012	3,760	0,008
RDWP_24	2,339	0,001	2,842	0,003	3,278	0,004	3,725	0,004
RDWP_28	2,322	0,002	2,834	0,002	3,282	0,002	3,733	0,002
RDWP_32	2,195	0,004	2,709	0,003	3,153	0,004	3,615	0,009
RDWP_64	1,835	0,001	2,510	0,003	3,048	0,002	3,562	0,003
RPWP_8	2,688	0,010	3,209	0,009	3,701	0,015	4,260	0,007
RPWP_12	2,554	0,003	3,070	0,004	3,543	0,004	4,012	0,002
RPWP_16	2,542	0,001	3,060	0,001	3,523	0,002	3,997	0,001
RPWP_20	2,498	0,001	3,011	0,001	3,462	0,001	3,940	0,001
RPWP_24	2,440	0,001	2,953	0,001	3,402	0,001	3,872	0,001
RPWP_28	2,398	0,001	2,919	0,001	3,377	0,001	3,841	0,001
RPWP_32	2,346	0,001	2,892	0,001	3,357	0,001	3,819	0,001
RPWP_64	1,885	0,001	2,570	0,001	3,114	0,001	<b>3,607</b>	0,001

Table 4.2: Mean values of estimated  $\hat{\alpha}$  and their variances computed from 10 FBF realizations with image size equal to  $2048 \times 2048$ .

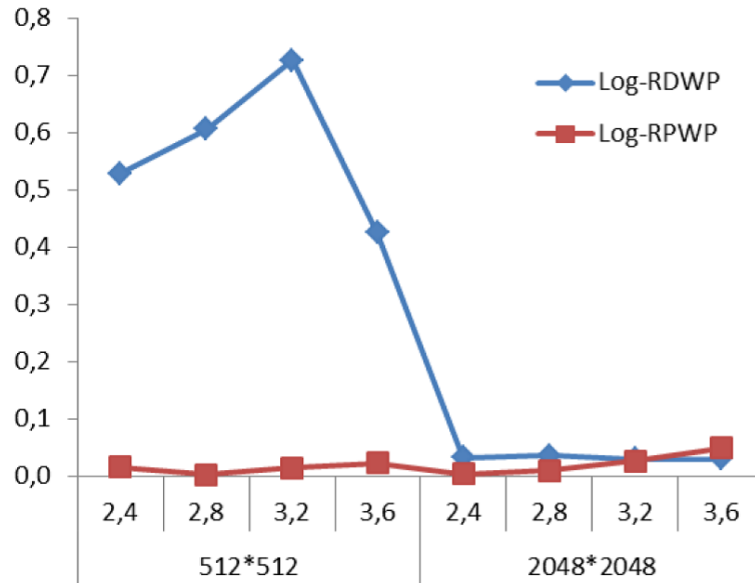


Figure 4.3: Mean square value computed with values obtained in Tab. 4.1 and Tab. 4.2 for  $RDWP_8$  and  $RPWP_{32}$  (best results) with image size equal to  $512 \times 512$  and  $2048 \times 2048$ .

#### 4.3.4 Performance of Log-RPWP Hurst parameter estimator

In the literature two 2-D Hurst parameter estimation - Log-Regression based on Poly-Harmonic Wavelet (denoted here as Log-RPHW) and Maximum Likelihood based on Poly-Harmonic Wavelets (denoted here as ML-PHW) - methods have been proposed in [97]. The methods Log-RPHW and ML use isotropic poly-harmonic wavelets of [107] and

the fact that the poly-harmonic wavelet turns out to be a whitening operator for FBF, see [97] for details.

We experimentally demonstrate the performance of Log-RPWP Hurst parameter estimator (see [98]) based on 2-D wavelet packet spectrum for the estimation of the Hurst parameter of an image, in comparison with Log-RPHW and ML-PHW estimators proposed in [97, 107]. The experimental setup concerns FBF sampling from random number generators. Two generators are used for experimental tests: the Generator #1 of [107] is an FBF synthesis *via* back-projections from PolyHarmonic wavelet coefficients and the Generator #2 proposed by [57] is a direct spatial synthesis by imposing the covariance structure of Eq. (3.41).

Sample FBF	Log-RPWP			Log-RPHW		ML-PHW	
	$H$	$\widehat{H}$	$std$	$\widehat{H}$	$std$	$\widehat{H}$	$std$
Generator #1	0.2	0.210	0.031	0.204	0.009	0.200	0.006
	0.4	0.427	0.020	0.392	0.012	0.392	0.009
	0.6	0.643	0.039	0.600	0.010	0.597	0.007
	0.8	0.877	0.017	0.792	0.006	0.793	0.004
Generator #2	0.2	0.156	0.018	-0.029	0.004	-0.088	0.005
	0.4	0.424	0.026	0.264	0.014	0.226	0.010
	0.6	0.579	0.033	0.452	0.024	0.362	0.035
	0.8	0.815	0.048	0.415	0.029	0.313	0.023

Table 4.3: Mean values and standard deviations for estimated Hurst parameters from 10 FBF realizations.

Tab. 4.3 gives, for FBF Generators #1 and #2, the best relevant Hurst parameter estimations for all Log-RPWP, Log-RPHW and ML-PHW, when the maximal wavelet decomposition level is limited to 7 (sample realizations are with sizes  $512 \times 512$ ). Hurst parameter estimation was realized from 10 FBF realizations and  $H \in \{0.2, 0.4, 0.6, 0.8\}$ .

One can observe from Tab. 4.3 that accuracies of Log-RPHW and ML-PHW methods are limited to the Polyharmonic FBF: this is due to that the latter is synthesized by using the same wavelets as those involved in Log-RPHW and ML-PHW estimation routines. However, Log-RPHW and ML-PHW methods fail to estimate Hurst parameter of Generator #2's FBF, which uses no *a priori* on a specific wavelet generating function.

In contrast to Log-RPHW and ML-PHW, the Log-RPWP method gives relevant results whatever the generator used to derive FBF samples, as it can be seen in Tab. 4.3. In the following experimental tests on real word data, we thus focus on Log-RPWP estimator which guarantees robustness of the Hurst parameter estimation.



---

## Application to HRTEM image characterization

---

In this chapter, we present several applications of the models presented in Chapters 3 and 4 for HRTEM image characterization. The first application is soot HRTEM image texture synthesis from random field  $K$ -factor GFBF modeling. The second application is modeling and synthesis of HRTEM image of catalyst with the convolution mixture of FBF and modulated FBF. Let us notice that the synthesis of textures issued from HRTEM images is a scientific domain of interest and some recent works on the subject can be found in [103]. Of course, in these works, other models are used to synthesize textures. The last application is morphology based discrimination of catalysts using ARFBF.

### 5.1 $K$ -factor GFBF samples and Soot HRTEM textures

In this section, we generate several samples of  $K$ -factor GFBF and analyse these samples, in comparison with a soot texture. The analysis is performed here by using wavelet packet spectrum (see [8] for details).

Different  $K$ -factor GFBF realizations are provided in Fig. 5.1. These realizations exhibit several non-trivial structures (that do not reduce in line-wise or column-wise delineations). In Fig. 5.1, poles and Hurst parameters are generated from random variables distributed as Gaussian, Uniform and Gamma respectively. Poles are distributed in  $[0, \frac{\pi}{2}] \times [0, \frac{\pi}{2}]$  and Hurst parameters are distributed in  $]0; 0.5[$ .

Fig. 5.2 provides spectra of GFBF textures given in Fig. 5.1. In Fig. 5.2, when poles are very close, they fuse in one "big" pole. Poles associated with small Hurst parameters tend to be dominated (display setup) by other poles. Spectra are estimated from images in order to highlight the impacts of sampling and estimation. The spectra have been computed from the wavelet packet method given in [10]. Fig. 5.2 highlights the peaks and the exponential decay in the neighborhood of these peaks, for the synthesized tex-

tures from GFBF  $\mathcal{E}_{\mathcal{H}_K}$ . A visual analysis highlights that K-factor GFBF  $\mathcal{E}_{\mathcal{H}_{21}}$  and  $\mathcal{E}_{\mathcal{H}_{22}}$

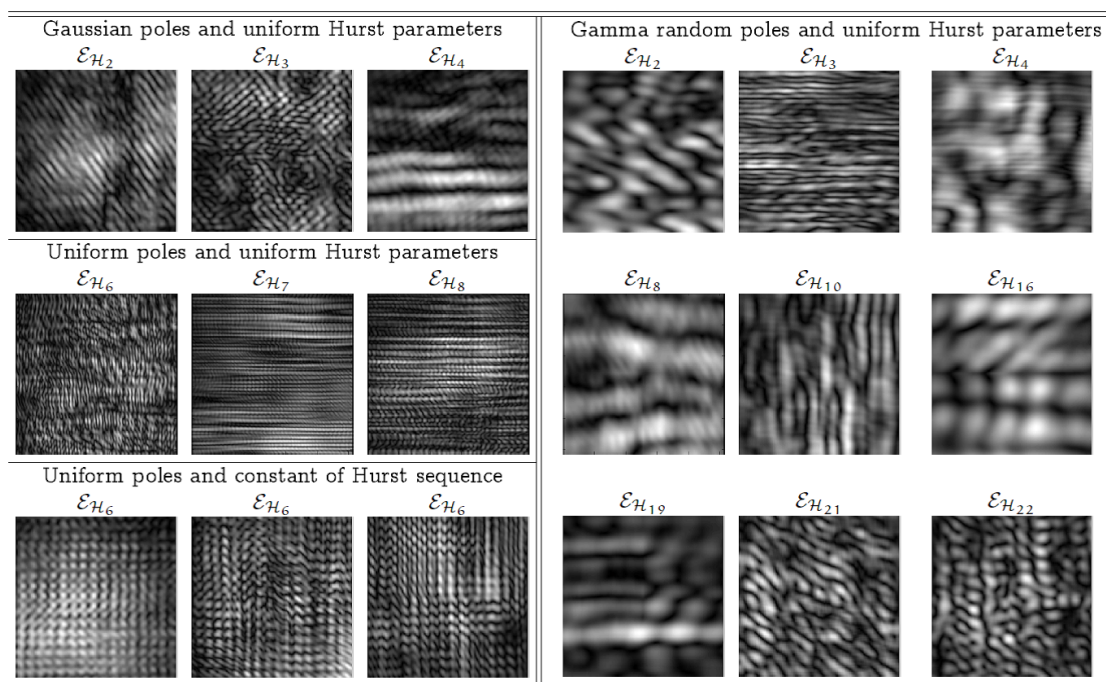


Figure 5.1:  $K$ -factor GFBF  $\mathcal{E}_{\mathcal{H}_K}$  for different values of  $K$ . Figure is originated from [10].

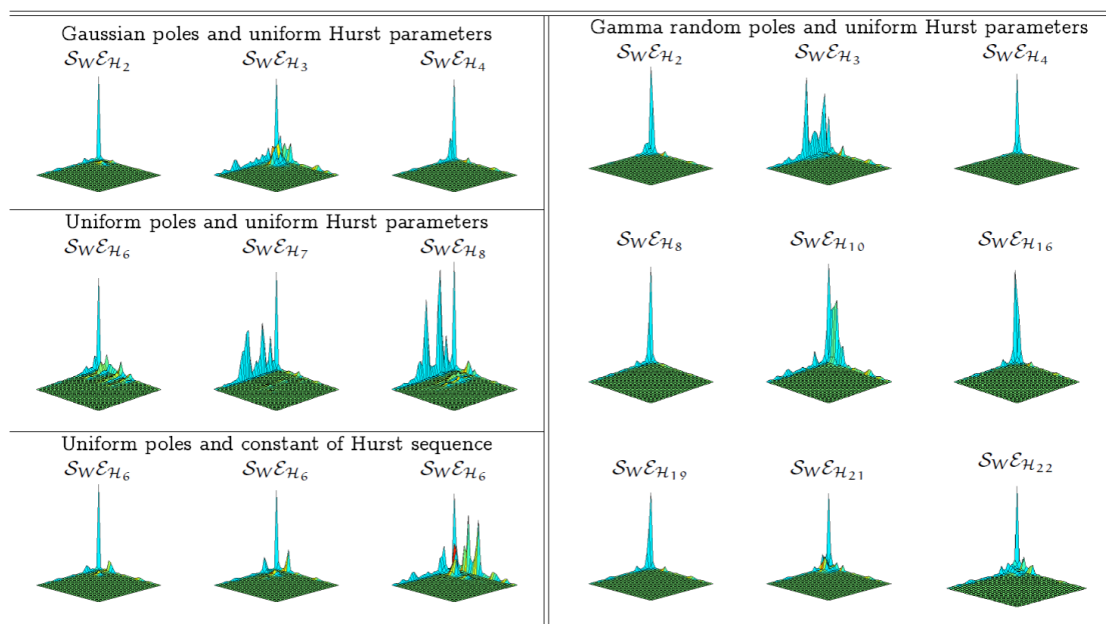


Figure 5.2: Wavelet spectra  $S_W \mathcal{E}_{\mathcal{H}_K}$  of  $K$ -factor GFBF  $\mathcal{E}_{\mathcal{H}_K}$  texture images given in Fig. 5.1. Spectra are given in  $[0, \frac{\pi}{2}] \times [0, \frac{\pi}{2}]$ . Figure is originated from [10].

of Fig. 5.1 present textural structures similar with some fringes observed on HRTEM image given by Fig. 5.3 (see the zoomed versions).

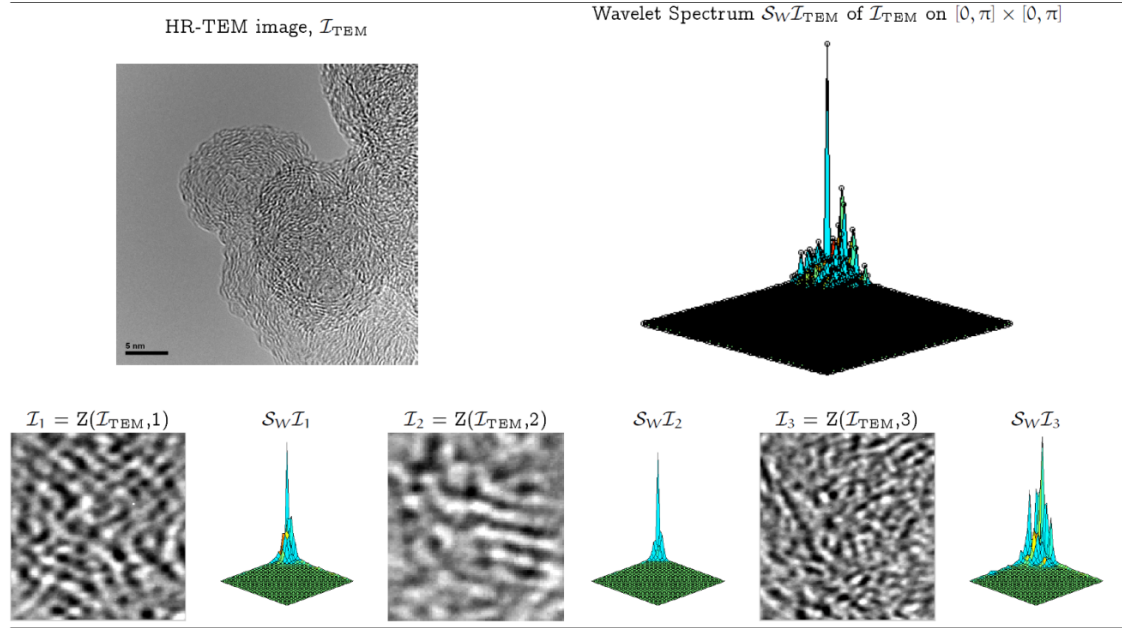


Figure 5.3: HRTEM image  $I_{TEM}$  (top-left) and its wavelet spectrum  $S_W I_{TEM}$  (top-right). Bottom: some Zooms (Z) on regions of image  $I_{TEM}$  and their wavelet spectrum.

This remark is also confirmed by the spectra  $S_W \mathcal{E}_{\mathcal{H}_{21}}$  and  $S_W \mathcal{E}_{\mathcal{H}_{22}}$  given by Fig. 5.2. Note that in Fig. 5.3, the frequency grid is  $[0, \pi] \times [0, \pi]$  for  $S_W I_{TEM}$  and  $[0, \frac{\pi}{2}] \times [0, \frac{\pi}{2}]$  for  $S_W I_1$ ,  $S_W I_2$ ,  $S_W I_3$  (most textural information is concentrated on the latter grid, see for instance  $S_W I_{TEM}$ ). This is consistent with the fact that fringe information are not expected to lie in the highest frequencies.

In practice, modeling HRTEM image by a  $K$ -factor GFBF requires the estimation of different parameters:

- the location of frequencies associated with poles and their numbers,
- the local exponential decays near those frequencies relating the Hurst parameters.

Prior to addressing the more complex and challenging  $K$ -factor GFBF parameter estimation (for  $K \geq 2$ , closed poles can lead to confusion between a single estimated "big" pole or 2 different "small" poles, especially when  $K$  is large and the image resolution limited), we consider in the following sections, the analysis of a sub-class of GFBF.

## 5.2 Convolution mixture of FBF and modulated FBF modeling for HRTEM catalyst texture synthesis

### 5.2.1 Motivation

The description of textural and spectral similitudes observed in Section 5.1 will be investigated more concisely in this section, by focusing on different HRTEM sub-images with single or dual fringe informations. The HRTEM sub-images containing active phases

(fringes) under consideration have been described in Section 2.3. We propose to use the CMFBBF model defined in Section 4.2.1.3 in the following, for modeling, analyzing, and synthesizing the fringes observed in HRTEM images. We first estimate parameters of CMFBBF on real images of catalyst. Then, using these parameters, we propose to synthesize new numerical images by means of the model.

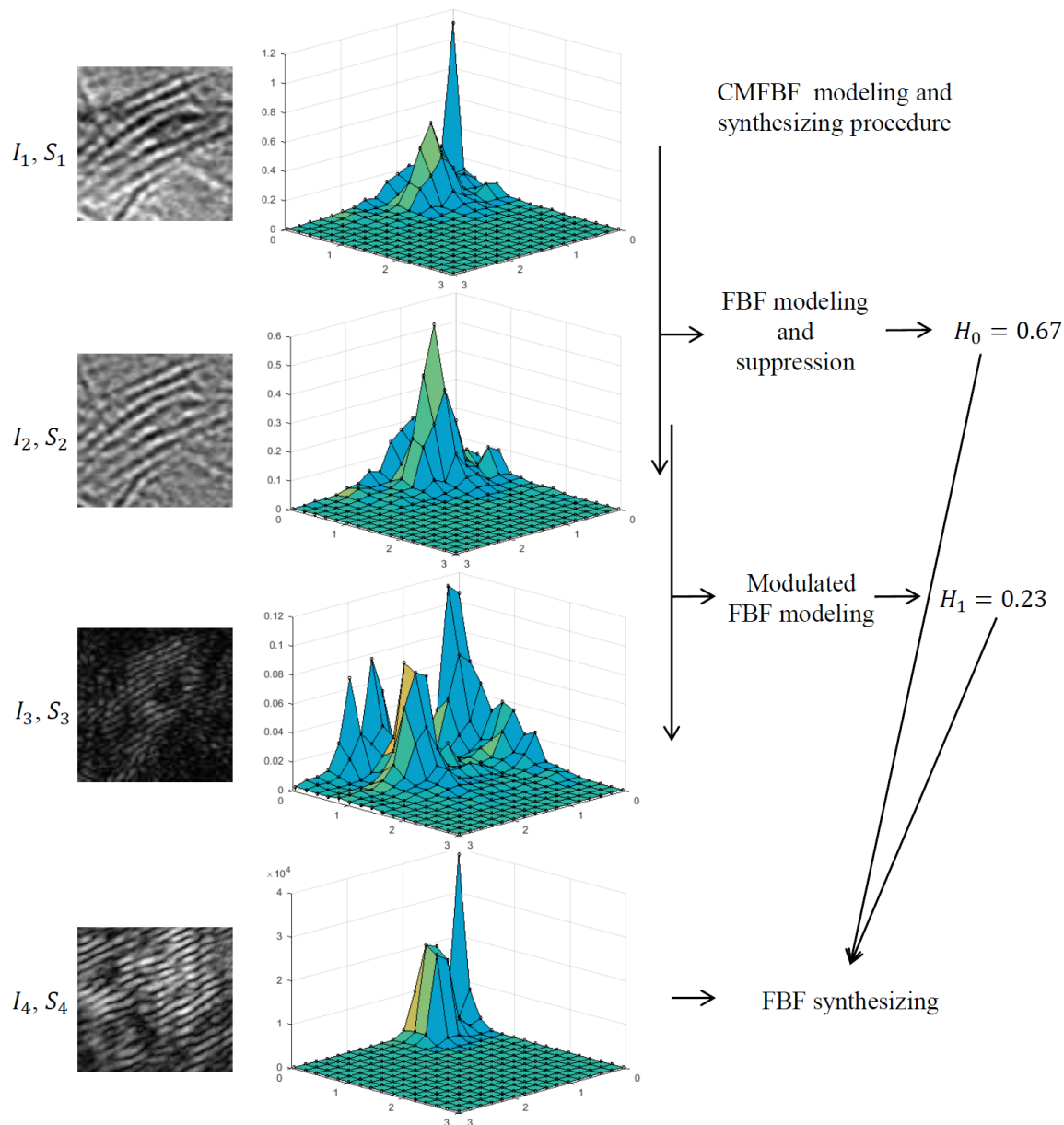


Figure 5.4: The original image  $I_1$  (catalyst HRTEM) with its WPS (Wavelet Packet Spectrum)  $S_1$  are given in the first row. The image  $I_4$  (row 4) has been synthesized from CMFBBF modeling of  $I_1$ . The intermediate images ( $I_2, I_3$ ) and the spectral features ( $S_2, S_3$ ) obtained at every step of this modeling are given for illustration. The WPS of  $I_4$  is  $S_4$  and it shows strong similarities with  $S_1$ .

## 5.2.2 CMFBBF modeling for catalyst HRTEM image

Denote an original HRTEM image as  $I_1$  (we consider one arbitrary sub-image containing active phases (fringes) as an input/original image) and its Wavelet Packet Spectrum (WPS) denoted as  $S_1$ . Fig. 7.1 - Row 1 provides an example of such an original HRTEM image  $I_1$  and its WPS  $S_1$ . This WPS has been computed from the wavelet packet method given in [8].

WPS  $S_1$  of Fig. 7.1 - Row 1 highlights one peak located at zero frequency and a second one located somewhere with exponential decay in the neighborhood of these peaks. Thus, a CMFBBF model is expected to be relevant for modeling  $I_1$ . Indeed, a CMFBBF model has a spectral representation associated with two peaks: one peak located at zero frequency and the other located elsewhere (see Section 4.2.1.3 for details). The peak at the zero frequency corresponds to slow grey-level variations in the HRTEM image (considered as background) and will be modeled by an FBF. Fundamentally, this peak is not representative of active phase (fringes). We use a second modulated FBF to model these fringes.

The procedure used for associating a CMFBBF model to  $I_1$  is summarized by the bloc diagram of Fig. 5.5. Details concerning the steps associated with this procedure are given below.

### 5.2.2.1 Step 1: FBF modeling and suppression

A first FBF model is used to describe the peak located at zero frequency (see  $S_1$  in Fig. 7.1). We estimate the Hurst parameter denoted as  $H_0$  by using the method described in Section 4.3. After removing the contribution of this first FBF in  $I_1$ , the residual image is denoted  $I_2$  and its WPS, denoted  $S_2$  (see Fig. 7.1 - Row 2), can be given as

$$S_2(u, v) = \frac{S_1(u, v)}{S_{FBF}(u, v)}. \quad (5.1)$$

Fig. 7.1 - Row 2 highlights that modeling the peak at the zero frequency by an FBF is relevant: the energy of PSD  $S_1$  around the zero frequency has been almost totally removed in  $S_2$ .

### 5.2.2.2 Step 2: Modulated FBF parameter estimation

Consider the residual image  $I_2$  obtained after FBF suppression (previous sub-section, see  $I_2$  and its WPS  $S_2$  in Fig. 7.1 - Row 2). The residual peak located outside the zero frequency in  $S_2$  is associated with a modulated FBF. For estimating the Hurst parameter associated to this modulated FBF, we

- address estimating the location of the maximum in the WPS  $S_2$ , then,
- shift this peak to the zero frequency (demodulation, the demodulated image is denoted  $I_3$  and its corresponding WPS  $S_3$  are given in Fig. 7.1 - Row 3) and, finally,

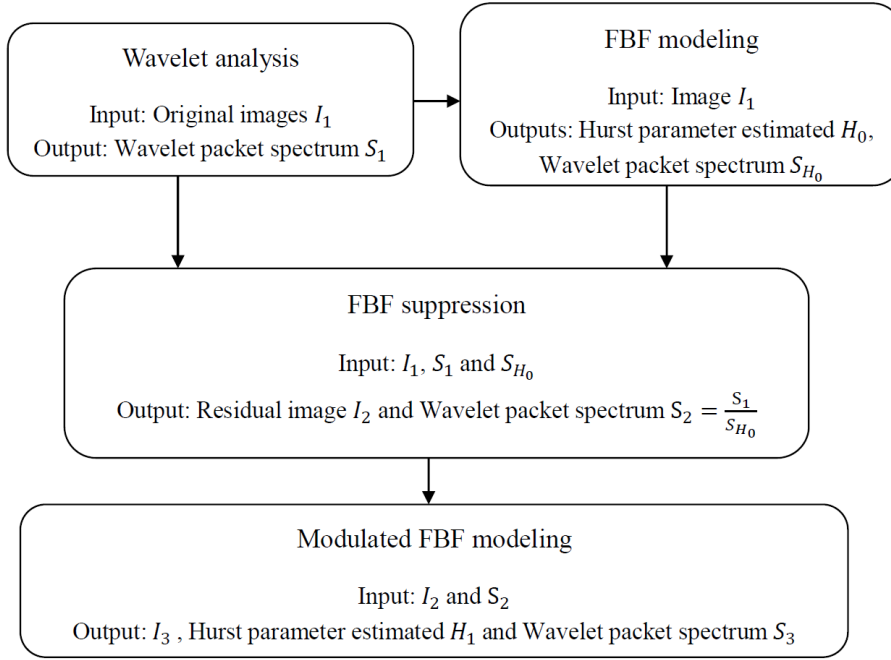


Figure 5.5: The complete CMFBB framework.

- estimate the Hurst parameter associated to this modulated FBF from  $I_3$  (as if  $I_3$  is an FBF, due to the demodulation step above). We denoted this Hurst parameter as  $H_1$ .

### 5.2.3 Synthesis of catalyst HRTEM images from CMFBB

In this section, we present catalyst HRTEM image synthesis from CMFBB modeling associated with Hurst parameters  $H_0$  and  $H_1$  estimated by considering original catalyst HRTEM images.

Fig. 7.1 - Row 4 presents a first example of texture synthesis by using Hurst parameters  $H_0 = 0.67$  and  $H_1 = 0.23$  estimated from the HRTEM image  $I_1$  modeled in Section 5.2.2. The synthesized image is denoted  $I_4$  and its WPS is denoted  $S_4$ .

Fig. 5.6 and Fig. 5.7 present two other examples of synthesis from catalyst HRTEM image CMFBB modeling. The catalyst HRTEM images are denoted  $im_1$  and  $im_2$  in these figures. For  $im_1$ , the Hurst parameters estimated are  $H_0 = 0.15$  and  $H_1 = 0.36$ . For  $im_2$ , the Hurst parameters estimated are  $H_0 = 0.60$  and  $H_1 = 0.61$ .

A test set consisting of 18  $Cat_X$  and 8  $Cat_Y$  representative HRTEM images is given by Fig. 5.8 and Fig. 5.9. The synthetic CMFBB images obtained from their modeling provide an average of  $H_0$  and  $H_1$  parameters for  $Cat_X$  and  $Cat_Y$ : this would correspond to a representative average synthetic image of active catalyst phases.

Fig. 5.10 gives 4 synthetic CMFBB images obtained from the average of  $H_0$  and  $H_1$

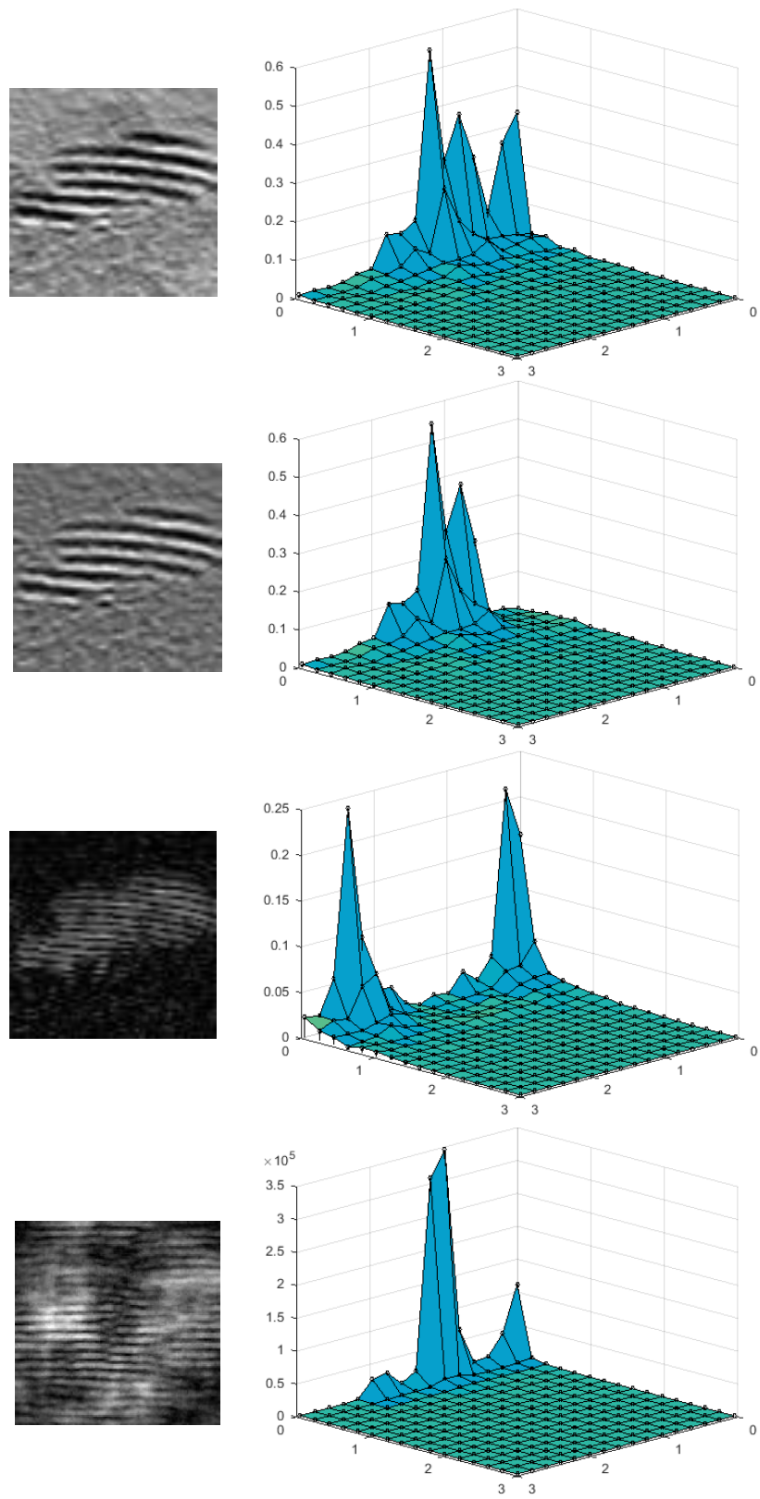


Figure 5.6: Synthesis of catalyst HRTEM image using CMFBBF estimated Hurst parameters  $H_0$  and  $H_1$  from  $im_1$ . In the first row, the original image and its WPS; in the second row, the residual image (after removing the FBF contribution from the original image) and its WPS; in the third row, the demodulated version of the residual image and its WPS. Finally, the last row presents the synthesized image with its corresponding WPS.

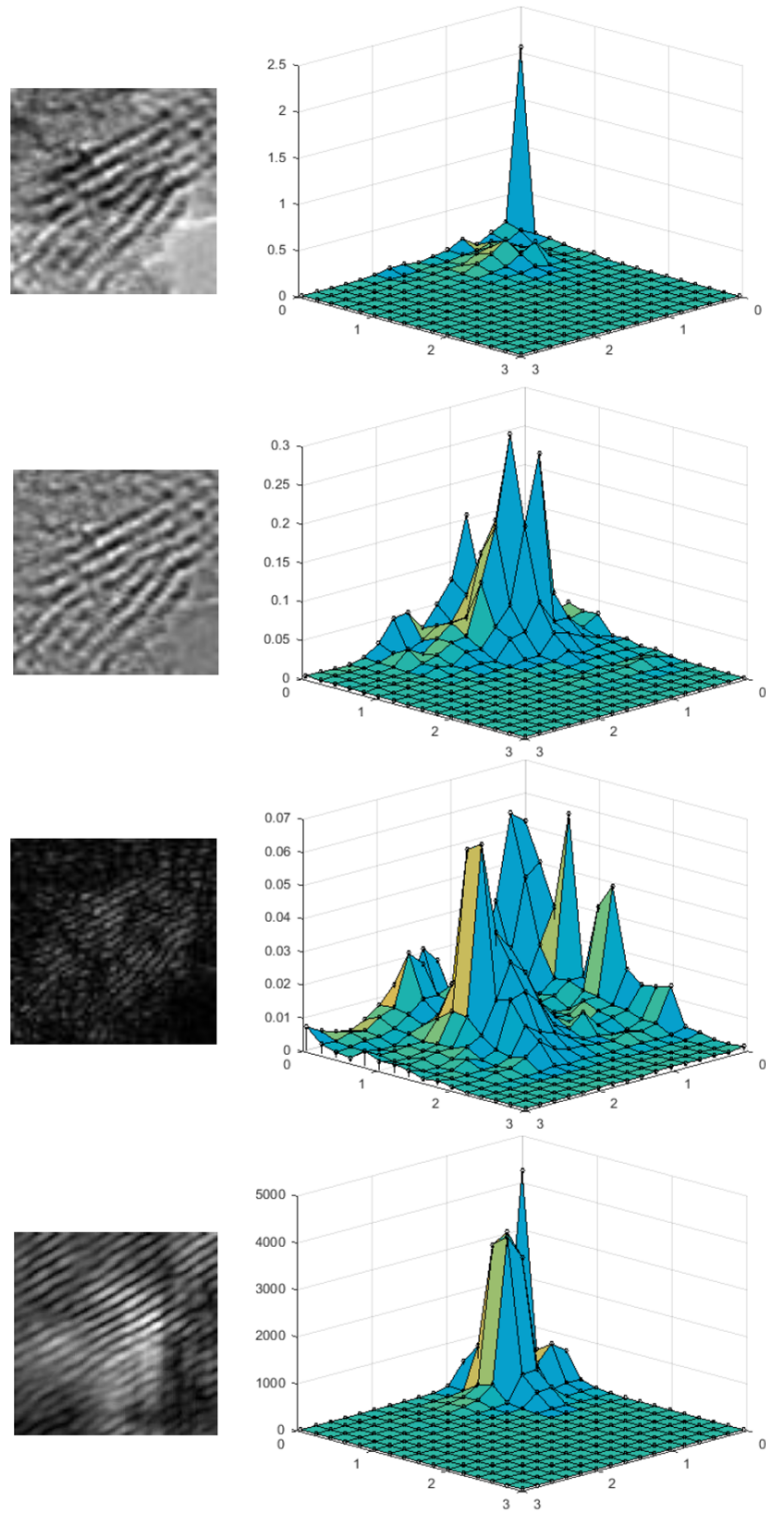


Figure 5.7: Synthesis of catalyst HRTEM image using CMFBBF estimated Hurst parameters  $H_0$  and  $H_1$  from  $im_2$ . In the first row, the original image and its WPS; in the second row, the residual image (after removing the FBF contribution from the original image) and its WPS; in the third row, the demodulated version of the residual image and its WPS. Finally, the last row presents the synthesized image with its corresponding WPS.

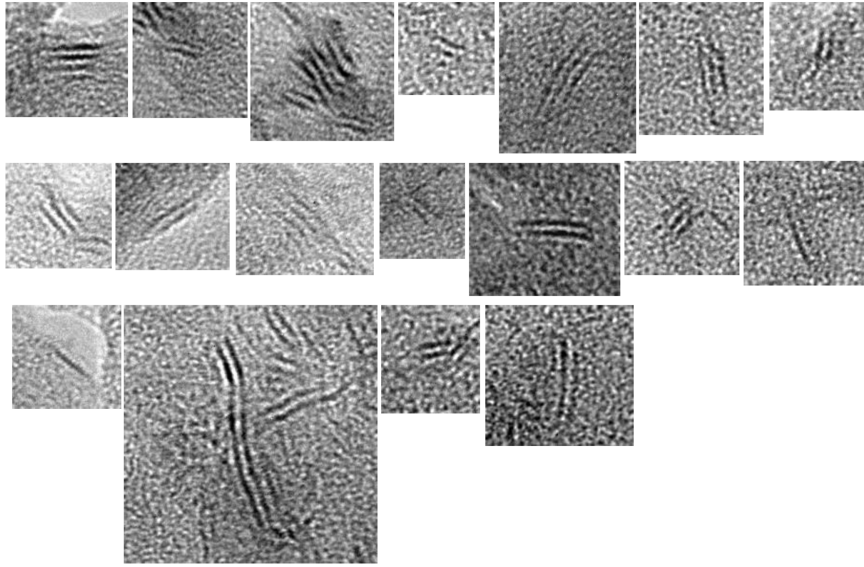


Figure 5.8: Selected 18  $Cat_x$  HRTEM images.

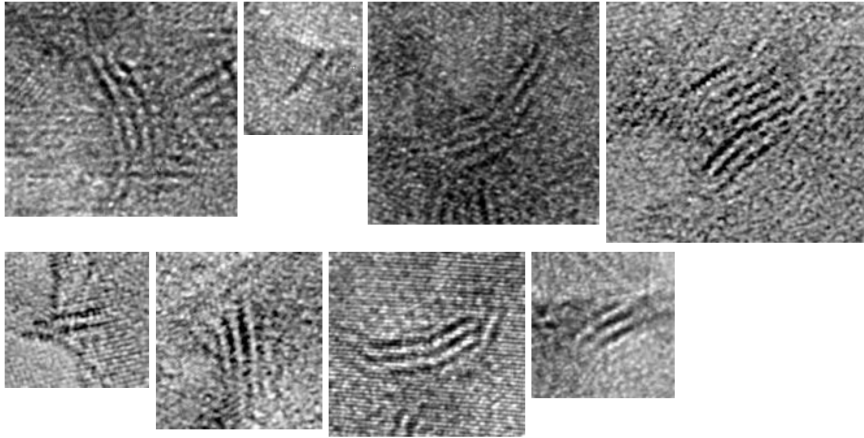


Figure 5.9: Selected 8  $Cat_y$  HRTEM images.

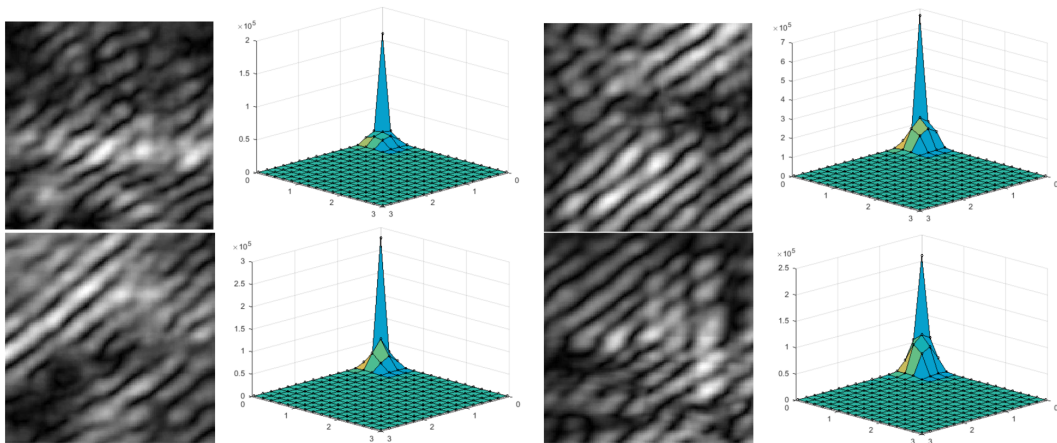


Figure 5.10: Images synthesized from an average of  $H_0$  and  $H_1$  parameters of 18  $Cat_x$  HRTEM images using CMFBF modeling and its WPS.

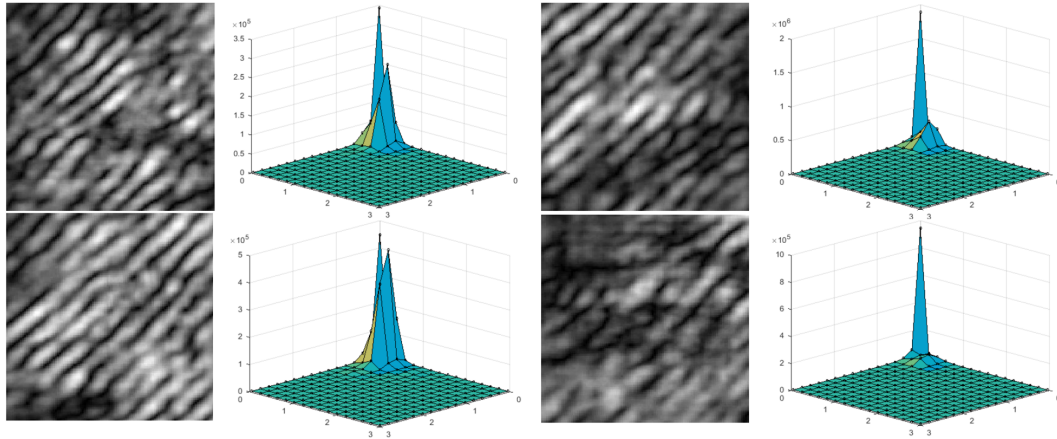


Figure 5.11: Images synthesized from an average of  $H_0$  and  $H_1$  parameters of 8  $Cat_Y$  HRTEM images using CMFBF modeling and its WPS.

parameters associated with the 18  $Cat_X$  HRTEM images. The average estimated Hurst parameters  $H_0$  and  $H_1$  are 0.60 and 0.41 respectively.

Fig. 5.11 gives 4 synthetic CMFBF images obtained from an average of  $H_0$  and  $H_1$  parameters with the 8  $Cat_Y$  HRTEM images. The average estimated Hurst parameters  $H_0$  and  $H_1$  are 0.54 and 0.24 respectively.

In all synthesis examples provided in this section, the synthesized textures by using Hurst parameters  $H_0$  and  $H_1$  estimated from catalyst HRTEM image presents some structural similarities with original HRTEM image. In future work, it could be interesting to investigate the case of multiple fringes: these fringes may require a convolution mixture with a higher number FBF factors so as to take into account several spectral peaks.

### 5.3 Morphology analysis of catalyst active phase using ARFBF modeling

In this section, we consider the application of ARFBF model to catalyst HRTEM image characterization and discrimination. Fig. 5.12 provides the block diagram of the complete analysis chain proposed for this purpose.

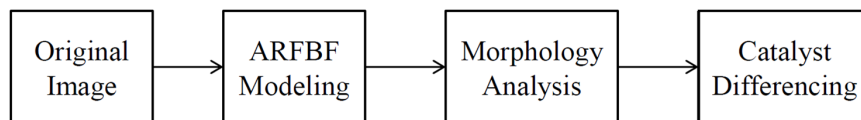


Figure 5.12: Morphology analysis procedure using ARFBF model.

#### 5.3.1 Problem formulation

Atomic structure of active phases can be observed directly by HRTEM imaging. The analysis of these fringes is generally composed of several steps: noise reduction, contrast

enhancement, segmentation and morphological analysis such as length and tortuosity measurements (see [113]).

We propose hereafter a completely different approach with characterization in the frequency domain to obtain information about regularity of spacing or regularity of curvature for layers of fringes. Another advantage of the frequency domain is to separate the information associated with "superimposed" fringes with different main orientations, which produces different spectral bumps. However, analysis in this domain is an intricate work because of high frequency due to acquisition noise, and of low frequency due to the catalyst support. Our approach uses wavelet filtering, suppression of catalyst support contribution by means of an FBF modeling, and use of an AR model to smooth the residue image corresponding to fringes. A morphological characterization of these lobes will allow us to obtain information about inter fringes distance, regularity of spacing observing distance variation and regularity of curvature looking at tangential length of lobes (see Section 5.3.3).

In this section, we study sub-images containing active phases (fringes) taken from HRTEM images of catalysts X and Y. We propose to use a model-based approach with ARFBF model to characterize these fringes of different catalysts. We first apply our proposed ARFBF modeling to analyze the entry image (see [98]), then apply our proposed morphology method on the DSP calculated from ARFBF estimated parameters. Finally, we use the properties of the estimated ARFBF model to distinguish different catalysts (see Fig. 5.12).

### 5.3.1.1 Pre-processing - WHFR

Depending on the acquisition conditions, certain HRTEM images are affected by high frequency disturbances induced by the alumina support of the catalyst and/or the electronic noise. An example of HRTEM image concerned by these disturbances is given by Fig. 7.2 - Row 1 - Left Image. An harmonic analysis is applied to calculate the PSD  $S_{I_1}$  of the input image  $I_1$ , see Fig. 7.2 - Row 1 - Middle and Right Images. In this figure, the 'Right-column' images are zoomed versions of the 'Middle-column' images. A pre-processing of the HRTEM image  $I_1$  is required for the removal of the high frequency disturbances visible in  $S_{I_1}$ .

Hereafter, we present a pre-processing of HRTEM images based on wavelet denoising, namely Wavelet based High Frequency Removal (WHFR) (see [19, 72, 66, 25]). WHFR processing can be defined as follows:

- Firstly, we apply a 2-D Discrete Stationary Wavelet Transform (DSWT, see [19]) to decompose the HRTEM image.
- Then, we keep the approximation coefficients and force to zero all detail coefficients.
- Finally, we apply a 2-D Inverse Discrete Stationary Wavelet Transform (IDSWT, see [19]) to reconstruct a high-frequency-free HRTEM image.

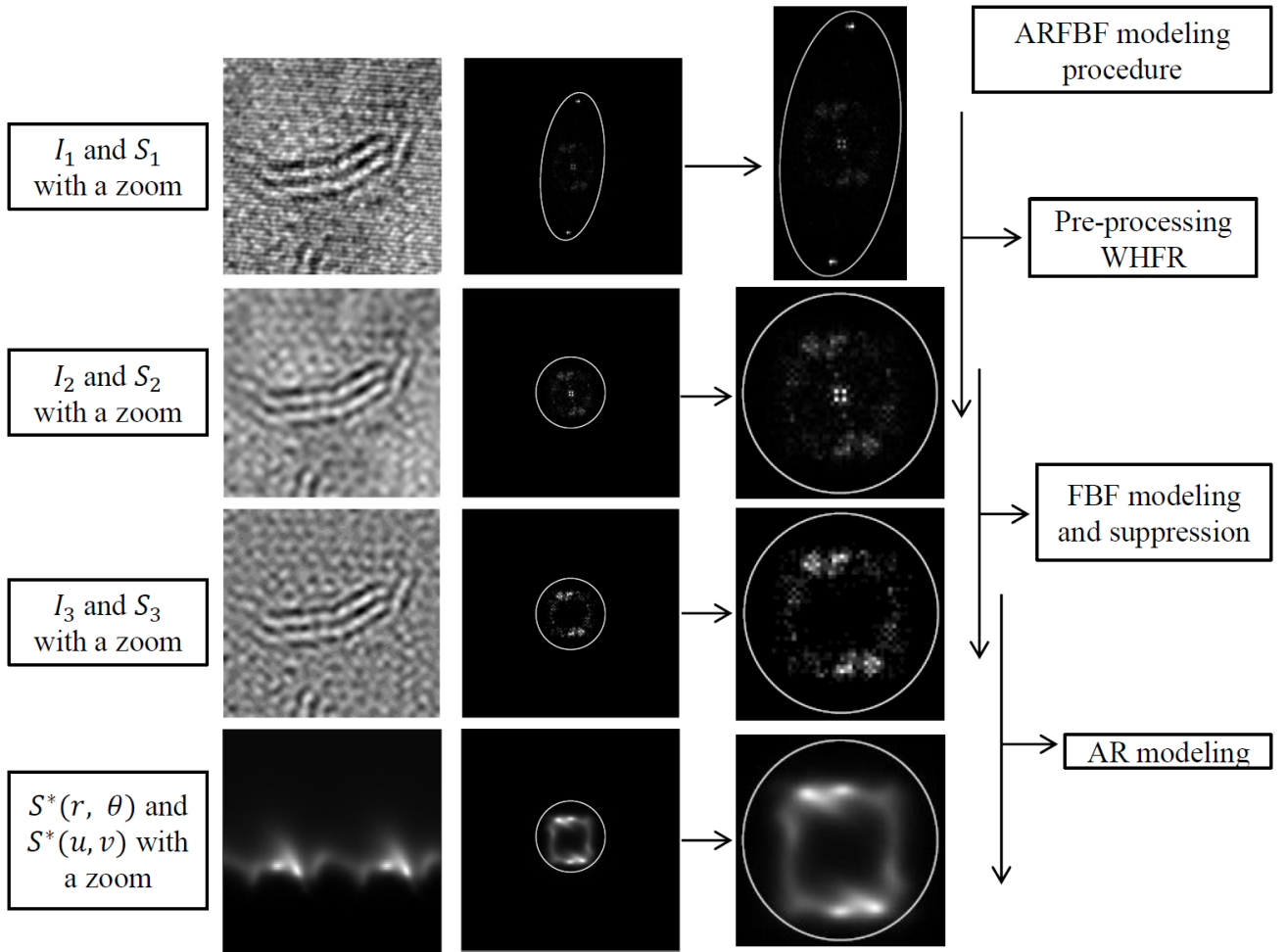


Figure 5.13: ARFBF modeling procedure of HRTEM image.

We apply the WHFR pre-processing to the original image  $I_1$ . The image after pre-processing is denoted  $I_2$  (see Fig. 7.2 - Row 2 - Left) and its corresponding PSD is denoted  $S_2$  (see Fig. 7.2 - Row 2 - Middle/Right). PSD  $S_2$  obtained shows that high frequencies are well removed with WHFR method.

## 5.3.2 ARFBF modeling of HRTEM image

### 5.3.2.1 FBF modeling and suppression

We apply an FBF modeling to estimate the Hurst parameter  $H$  from  $S_2$  and PSD  $S_{\hat{H}}$  associated to  $I_2$  is derived. Removing the contribution of the FBF in  $I_2$ , the spectrum of the residual part is

$$S_{residual}(u, v) = \frac{S_2(u, v)}{S_{FBF}(u, v)}.$$

The residual image is obtained and is denoted as  $I_3$  (see Fig. 7.2 - Row 3 - Left) and the residual spectrum  $S_{residual}(u, v)$  is denoted as  $S_3$  (see Fig. 7.2 - Row 3 - Middle/Right). From  $S_3$ , we can see that the peak (high energy) near the zero frequency has been almost

totally removed, without affecting central frequency content, proof of the relevancy of FBF assumption.

### 5.3.2.2 AR modeling

We apply an AR modeling to  $I_3$  (see Fig. 7.2 - Row 3 - Left). The maximum prediction supports in this work are  $M_1 = 10$  and  $M_2 = 10$ . The model is then used to compute a smooth PSD of  $I_3$  (denoted as  $S^*(r, \theta)$  in polar coordinate and  $S^*(u, v)$  in Cartesian coordinate).

Fig. 7.2 - Row 4 - shows that the PSD calculated by using the AR model is a smooth version of the PSD computed directly on  $S_3$ . In the Fig. 7.2 - Row 4, we show PSD both in polar (Fig. 7.2 - Row 4 - Left) and Cartesian (Fig. 7.2 - Row 4 - Middle/Right) representations. The spectra contain one or several main bump(s) whose form(s) is (are) associated to the active phase inside the HRTEM image  $I_3$  (also in image  $I_1$  and  $I_2$ ).

Let us notice that the AR spectrum in polar coordinates is not an interpolated version of the AR spectrum in Cartesian coordinates. Indeed, Eq. (3.54) shows that it is possible to represent the AR spectrum whatever is the support in the frequency domain.

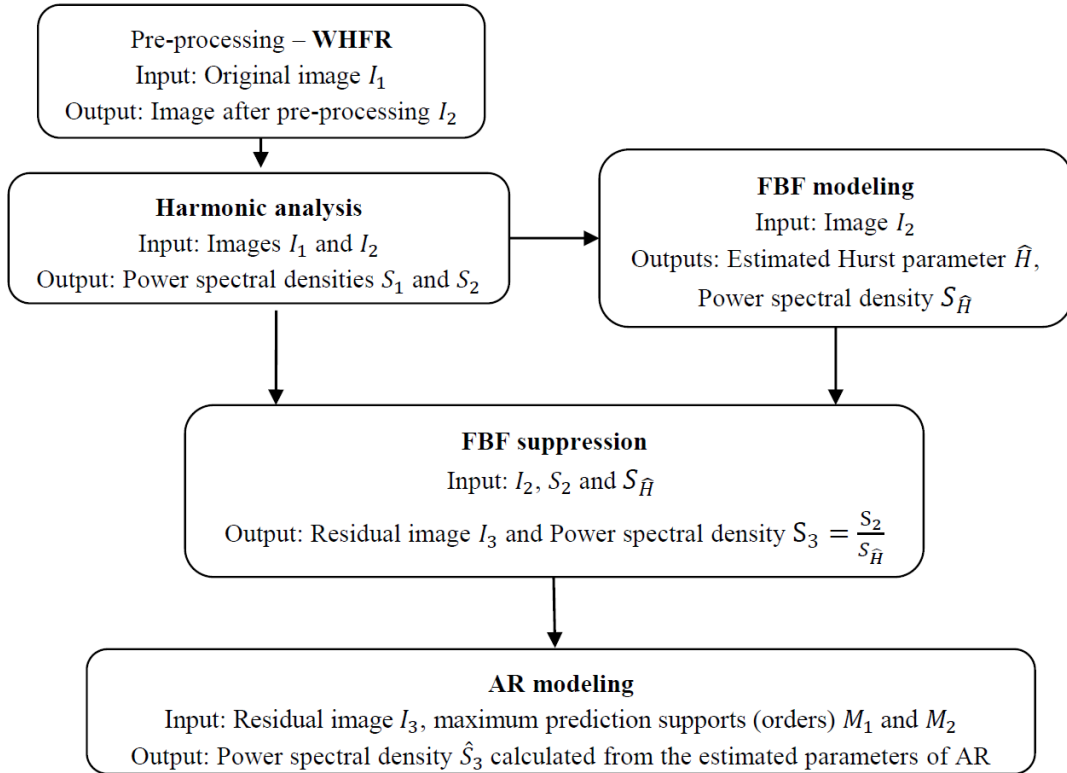


Figure 5.14: AR modeling.

The bloc diagram of Fig. 5.14 summarizes ARFBF modeling inputs and outputs. The next step is a morphological analysis of ARFBF estimated PSD.

### 5.3.3 Morphological analysis of HRTEM ARFBF features

The spectra calculated from ARFBF model association to an HRTEM image allow us to obtain a regularized version of input texture PSD. This regularized PSD will be used for morphological analysis of the fringes. The morphological analysis concerns the bumps (lobes) involved in spectral rings corresponding to local fringe features.

#### 5.3.3.1 Morphological analysis

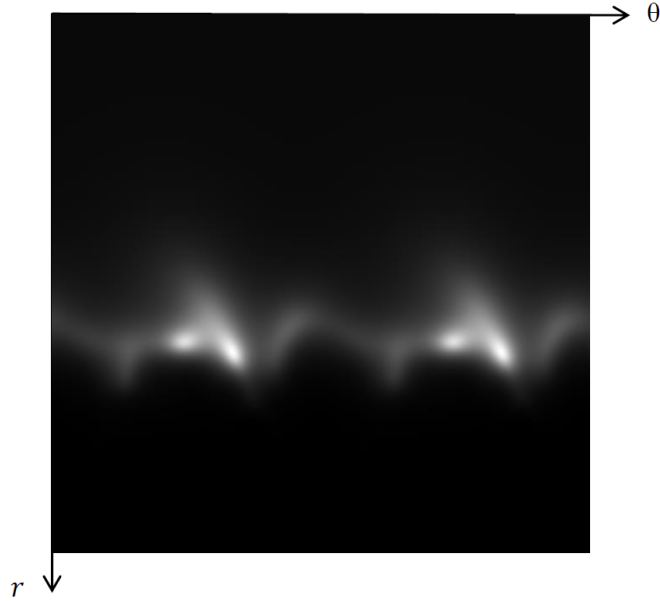


Figure 5.15: Estimated PSD  $S^*(r, \theta)$  from AR in polar coordinate.

The objective of morphology analysis based on ARFBF modeling of active phases aims at deriving characterizations on:

- regularity of spacing (observing distance variation) between active phases,
- regularity of curvature (looking at tangential length of lobes) of active phases.

Note that we have recalled in Fig. 2.13, the relations between lobe morphology and position in frequency domain, and fringes aspects.

In the following, we detail a morphological analysis of lobes which are present in the polar representation of the ARFBF PSD (image  $S^*(r, \theta)$  in Fig. 5.15).

#### 5.3.3.2 Lobe detection

##### *First lobe detection*

First, we search the point  $P_1[r^*, \theta^*]$  designing maximum value of  $S^*$  and we calculate an adaptive threshold  $\alpha_1$  as follows:

$$P_1 = \underset{r, \theta}{\operatorname{argmax}} S^*(r, \theta), \quad (5.2)$$

and

$$\alpha_1 = \lambda_1 S^*(P_1), \quad (5.3)$$

with  $\lambda_1 \in [0; 1]$ . Angle  $\theta \in [0; 2 \times \pi]$  in practice, but because of the symmetric property,

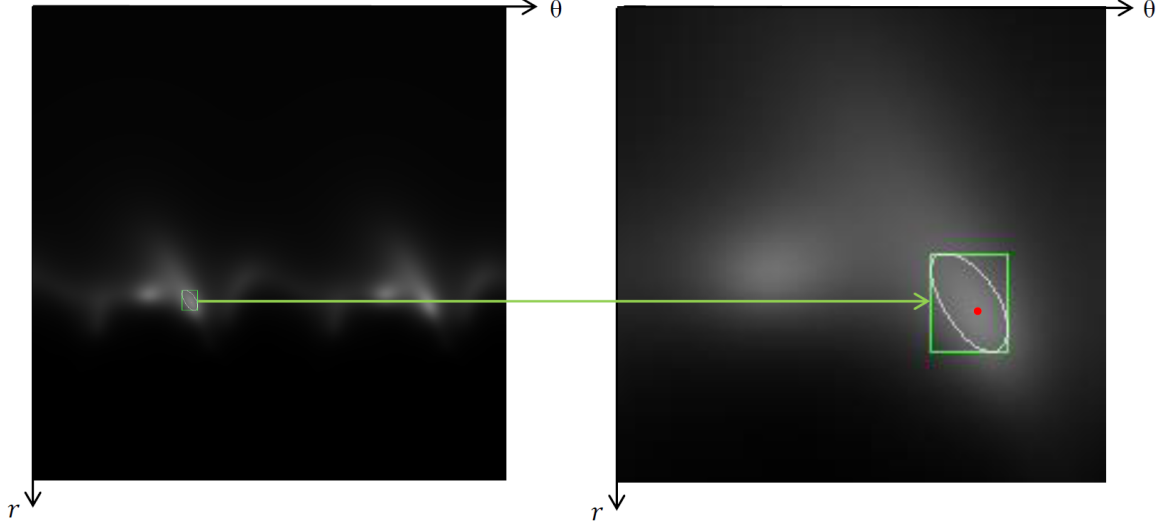


Figure 5.16: Estimated PSD  $S^*(r, \theta)$  from AR in polar coordinate and lobe detection.

in our application,  $\theta \in [0; \pi]$  (see right of Fig. 5.16). For  $\lambda_1$  value, we chose  $\lambda_1 = 0.8$ . Segmentation with  $\alpha_1$  can lead to several connected components. This issue can be easily handled using a morphological reconstruction (see [92]) with  $P_1$  as marker.

A first lobe (see Fig. 5.16) is obtained on a binary image  $Q_1$ :

$$Q_1 = \gamma_{rec}^{S^{**}}(P_1), \quad (5.4)$$

and

$$S^{**}(x) = \begin{cases} 1, & \text{if } S^*(x) > \alpha_1, \\ 0, & \text{otherwise.} \end{cases} \quad (5.5)$$

### *Second lobe detection*

If a second lobe is located on  $S^*$ , it can be obtained using a similar procedure. The contribution of the first lobe is removed on  $S^*$  using morphological dilation with disc of radius  $r$  on  $Q_1$ :

$$S_1^*(x) = \begin{cases} S^*(x), & \text{if } \delta_r(Q_1) \neq 0, \\ 0, & \text{otherwise.} \end{cases} \quad (5.6)$$

A new threshold  $\alpha_2$  is calculated and a binary image  $Q_2$  is obtained by:

$$\alpha_2 = \lambda_2 S^*(P_1), \quad (5.7)$$

with  $\lambda_2 \in [0; \lambda_1]$ ,

$$P_2 = \operatorname{argmax}_{r, \theta} S_1^*, \quad (5.8)$$

$$Q_2 = \gamma_{rec}^{S_1^{**}}(P_2), \quad (5.9)$$

and

$$S_1^{**}(x) = \begin{cases} 1, & \text{if } S_1^*(x) > \alpha_2, \\ 0, & \text{otherwise.} \end{cases} \quad (5.10)$$

In our application, we chose  $\lambda_2 = 0.6$ . In contrast with  $Q_1$ ,  $Q_2$  value is not necessarily with non-zero value if there is no remaining significant second lobe. We limit the study to the detection of two lobes in this experimental setup, with the knowledge that observation of more than two layers of overlapping fringes is rare in our application.

### 5.3.3.3 Characterization on average spatial distance between atomic layers $G$ , distance variation $\Delta_G$ and tangential length $L_\theta$

#### *Average spatial distance between atomic layers $G$*

For each lobe on images  $Q_i$ ,  $i = 1$  or  $2$ , denoting a layer of fringes, an average spatial distance between atomic layers is estimated by the distance value  $G$ ,

$$G = \frac{T_e}{r^*}, \quad (5.11)$$

associated to the maximum of the lobe  $P_1 = [r^*, \theta^*]$ ,  $T_e$  is the period of sample (here  $T_e = 0.057$  nm). Lobe on binary image  $Q_i$ ,  $i = 1$  or  $2$ , can be considered as an ellipse

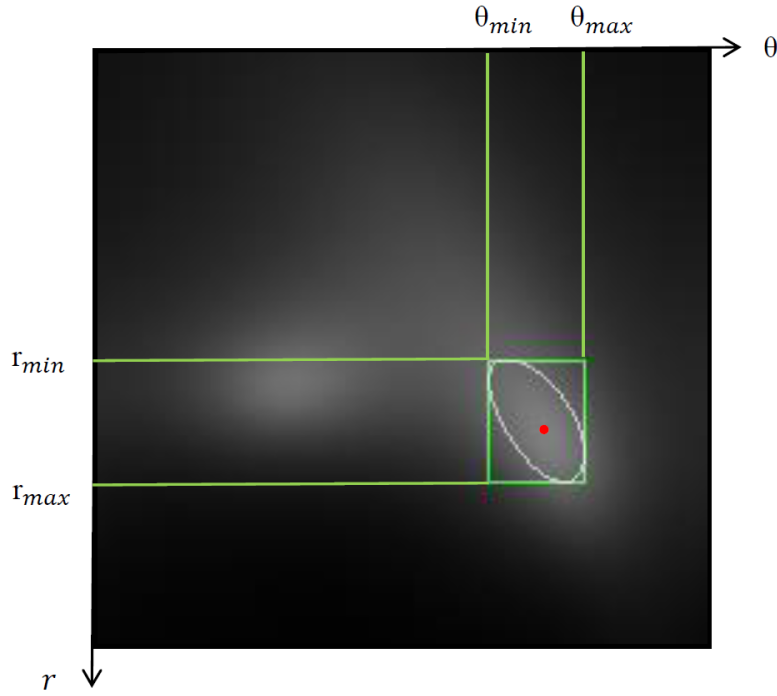


Figure 5.17: The spectral lobe detected can be considered as an ellipse embedded in a bounding box  $(r_{min}, r_{max}, \theta_{min}, \theta_{max})$ .

embedded in a bounding box  $(r_{min}, r_{max}, \theta_{min}, \theta_{max})$  (see Fig. 5.17). The extension of the lobe allows us to describe the changes in the distance between atomic layers (regularity of spacing) and in the curvature of atomic layers (regularity of curvature).

### *Distance variation $\Delta_G$*

The regularity of spacing can be estimated by distance variation  $\Delta_G$  (see Eq. (5.12)) which is defined as:

$$\Delta_G = |G_{max} - G_{min}|, \quad (5.12)$$

with

$$G_{max} = \frac{T_e}{r_{min}}, \quad (5.13)$$

and

$$G_{min} = \frac{T_e}{r_{max}}, \quad (5.14)$$

where  $T_e = 0.057$  nm.

### *Tangential length $L_\theta$*

The regularity of curvature can be estimated by tangential length  $L_\theta$  (see Eq. (5.15)) which is defined as:

$$L_\theta = |\theta_{max} - \theta_{min}|. \quad (5.15)$$

In the next section, we present our statistical analysis for the discrimination of catalyst active phases.

## **5.3.4 Statistical analysis for catalyst discrimination**

Based on the geometric features described previously, a comparison between two catalysts is presented. HRTEM images consist of  $1024 \times 1024$  pixels and their numerical resolutions are 0.057 nm by pixel. For catalyst X ( $Cat_X$ ), 93 sub-images containing active phases are taken from 21 HRTEM images. For catalyst Y ( $Cat_Y$ ), 109 sub-images containing active phases are taken from 19 HRTEM images (see Section 2.3 for details). For each sample, we calculate geometric features distance  $G$ , distance variation  $\Delta_G$  and tangential length  $L_\theta$  on detected lobes.

### **5.3.4.1 Statistical distributions of $G$ , $\Delta_G$ and $L_\theta$**

#### *Moments*

The first moment *Mean* and the second central moment *Variance* noted as  $\mu$  and  $var$  respectively can be defined as follows:

$$\mu = \frac{1}{n} \sum_{i=1}^n G_i, \quad (5.16)$$

$$var = \frac{1}{n-1} \sum_{i=1}^n (G_i - \mu)^2, \quad (5.17)$$

The standard deviation noted as  $\sigma$  ( $\sigma^2 = var$ ) can be expressed as:

$$\sigma = \left( \frac{1}{n-1} \sum_{i=1}^n (G_i - \mu)^2 \right)^{\frac{1}{2}}, \quad (5.18)$$

The third moment *skewness* measures the asymmetry of the probability distribution of a real-valued random variable (here,  $G$ ,  $\Delta_G$  or  $L_t$ ) about the corresponding mean value. The positive *skewness* indicates that the tail on the right side is longer or fatter than the left side.

The fourth moment (with normalization and shift) *kurtosis* measures the "tailedness" of the probability distribution of real-valued random variable  $G$ ,  $\Delta_G$  or  $L_t$ . Distribution of  $G$ ,  $\Delta_G$  or  $L_t$  with *kurtosis* is said to be *leptokurtic* (*kurtosis value*  $> 3$ ). Infrequent extreme deviations effecting the greater part of variance lead to a higher *kurtosis*.

The *skewness* (noted as *skew*) and *kurtosis* (noted as *kurt*) of  $G$  (same to  $\Delta_G$  and  $L_t$ ) are defined as follows:

$$skew = \frac{1}{n} \frac{\sum_{i=1}^n (G_i - \mu)^3}{\sigma^3}, \quad (5.19)$$

where  $E$  represents the expected value of  $(G - \mu)^3$ .

$$kurt = \frac{1}{n} \frac{\sum_{i=1}^n (G_i - \mu)^4}{\sigma^4}, \quad (5.20)$$

where  $E$  represents the expected value of  $(G - \mu)^4$ .

### ***Kernel distribution***

The distribution of these results are studied by using a Kernel smoothing function  $f_w$  which is defined as follows ([87, 74, 114, 43]):

$$f_w(x) = \frac{1}{nw} \sum_{i=1}^n K\left(\frac{x - x_i}{w}\right), \quad (5.21)$$

where  $n$  is the sample size,  $\{x_i\}_{i=1, \dots, n}$  are the set of considered samples,  $x \in \mathbb{R}$ ,  $K(\cdot)$  is the kernel smoothing function and  $w$  is the bandwidth.

Tab. 5.1 gives certain informative statistics of distance  $G$  (measured in  $nm$ ), distance variation  $\Delta_G$  (measured in  $nm$ ) and tangential lengths  $L_\theta$  (measured in degree) in terms of minimum value (denoted as *Min*), maximum value (denoted as *Max*), mean value (denoted as *Mean*), variance value (denoted as *Variance*), third standardized moment (denoted as *Skewness*) and fourth standardized moment (denoted as *Kurtosis*) of the detected lobes on  $Cat_X$  and  $Cat_Y$ . *Catalyst* ( $n$ ) presents the number of samples in  $Cat_X$  and  $Cat_Y$  respectively.

The inter-distance between two neighboring white/black fringes  $G$  is close to 0.615 nm (see [34]). In Tab. 5.1,  $G$  has almost same value for  $Cat_X$  and  $Cat_Y$  (0.611 nm vs 0.593 nm), it confirms  $G$  as a physical characterization. For  $\Delta_G$  and  $L_\theta$  of  $Cat_X$  and  $L_\theta$  of

<i>Catalyst</i> ( <i>n</i> )	<i>Cat<sub>X</sub></i> (93)			<i>Cat<sub>Y</sub></i> (109)		
<i>Stat</i>	<i>G</i>	<i>L<sub>r</sub></i>	<i>L<sub>θ</sub></i>	<i>G</i>	<i>L<sub>r</sub></i>	<i>L<sub>θ</sub></i>
<i>Min</i>	0.378	0.025	4.922	0.431	0.006	1.406
<i>Max</i>	0.744	0.377	21.094	0.692	0.169	17.930
<i>Mean</i>	0.611	0.141	12.088	0.593	0.085	8.807
<i>Variance</i>	0.004	0.005	14.779	0.003	0.001	14.625
<i>Skewness</i>	-1.153	1.282	0.286	-1.278	-0.092	0.238
<i>Kurtosis</i>	6.324	4.606	2.414	4.447	2.954	2.937

Table 5.1: Statistics of distance (see Eq. (5.11)), distance variation (see Eq. (5.12)) and tangential length (see Eq. (5.15)) features of the detected lobe of catalyst image databases (*Cat<sub>X</sub>* and *Cat<sub>Y</sub>*).

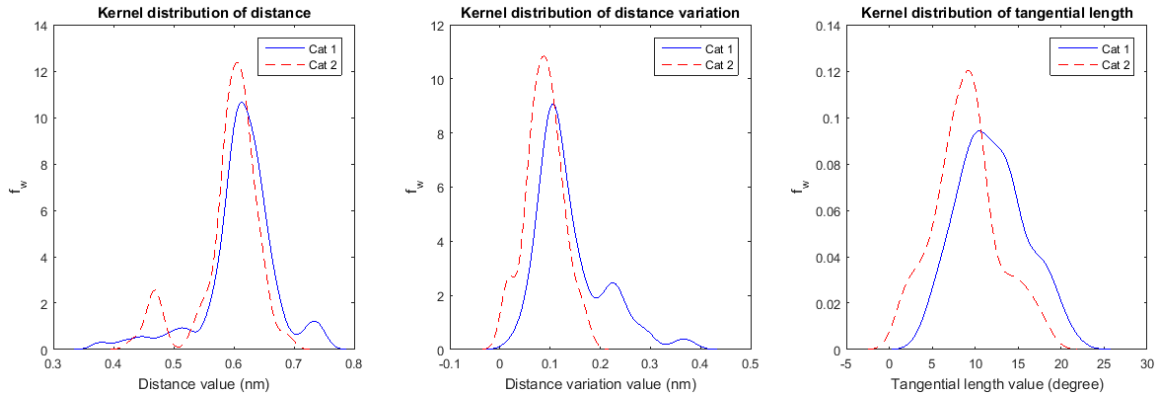


Figure 5.18: Kernel distributions of distance (left), distance variation (center) and tangential length (right) of the detected lobe of *Cat<sub>X</sub>* (— in blue) and *Cat<sub>Y</sub>* (--- in red).

*Cat<sub>Y</sub>*, the positive *skewness* values in Tab. 5.1 indicates that the tail on the right side is longer or fatter than that of the left side. When the *skewness* values are bigger, this phenomenon will be clearer (see Fig. 5.18). In contrast, for the other cases, the tail on the left side is longer or fatter than that of the right side (see Fig. 5.18) because of negative *skewness* values.

The *kurtosis* measures provided "tailedness" information of the distribution of variables *G*,  $\Delta_G$  or *L<sub>θ</sub>*. All kurtosis being larger than 3, one can conclude that *G* (for both of *Cat<sub>X</sub>* and *Cat<sub>Y</sub>*) and  $\Delta_G$  (just for *Cat<sub>X</sub>*) distributions are far from being Gaussian. In addition, when kurtosis are large, this implies that several outliers can be present in the corresponding variables. These observations are confirmed by Fig. 5.18 which shows the statistical distributions of *G*,  $\Delta_G$  or *L<sub>θ</sub>* for both catalysts.

#### 5.3.4.2 Kolmogorov-Smirnov test for catalyst discrimination

In this section, we propose Kolmogorov-Smirnov (KS) test for comparing *Cat<sub>X</sub>* and *Cat<sub>Y</sub>* ARFBF morphology characterizations. The KS measure is given by (see [76] for details)

$$\mathcal{K} = \max_x (|\hat{f}_1(x) - \hat{f}_2(x)|), \quad (5.22)$$

where  $\hat{f}_1, \hat{f}_2$  are the empirical cumulative distribution functions of catalyst datasets indexed by "1" and "2". Then  $\hat{f}$  can be in our study the cumulative kernel distribution for one of the three features:  $G$ ,  $\Delta_G$  and  $L_\theta$ . A threshold, based on asymptotic of  $\mathcal{K}$ , is used to derive a decision between alternative hypotheses:

- null hypothesis ( $\mathcal{H} = 0$ ) is that the two samples are drawn from the same catalyst, or
- $\mathcal{H} = 1$  means that the test rejects the null hypothesis at the 5% significance level.

### 1-D Kolmogorov-Smirnov test

Tab. 5.2 highlights that 1-D Kolmogorov-Smirnov test makes a clear discrimination between the two catalysts effective when considering parameters  $\Delta_G$  and  $L_\theta$ .

When performing 1-D Kolmogorov-Smirnov tests on sub-classes of catalysts  $Cat_X$  and  $Cat_Y$  (2 sub-classes per catalyst due to the limited number of available samples), then the test still performs a relevant discrimination, as it can be seen in Tab. 5.3.

Statistic	$Cat_k \setminus Cat_\ell$	$G$		$\Delta_G$		$L_\theta$	
		$Cat_X$	$Cat_Y$	$Cat_X$	$Cat_Y$	$Cat_X$	$Cat_Y$
$\mathcal{H}$	$Cat_X$	0	0	0	1	0	1
	$Cat_Y$	0	0	1	0	1	0
$10^3\mathcal{K}$	$Cat_X$	0	196	0	402	0	391
	$Cat_Y$	196	0	402	0	391	0

Table 5.2: 1-D Kolmogorov–Smirnov test of  $Cat_X$  and  $Cat_Y$ .

### 2-D Kolmogorov-Smirnov test

Because of 1-D Kolmogorov-Smirnov test making a clear discrimination between the two catalysts effective when considering parameters  $\Delta_G$  and  $L_\theta$ , we form a 2-D data with these two parameters. When we address 2-D Kolmogorov–Smirnov test to discriminate the two catalysts ( $Cat_X$  and  $Cat_Y$ ), Tab. 5.4 confirms our proposition. When performing 2-D Kolmogorov-Smirnov tests on sub-classes of catalysts  $Cat_X$  and  $Cat_Y$ , Tab. 5.5 shows that the test performs a very good discrimination between sub-classes of two different catalysts. Thus, our proposed ARFBF morphology characterization seems to be a suitable feature-based description to separate the two sets of HRTEM images representing active phases of the two catalysts.

A block diagram summarizing the whole ARFBF morphological characterization steps for catalyst discrimination is given by Fig. 5.19.

Stat	$Cat_k^m \setminus Cat_\ell^n$	$G$			
		$Cat_X^1$	$Cat_X^2$	$Cat_Y^1$	$Cat_Y^2$
$\mathcal{H}$	$Cat_X^1$	0	0	0	0
	$Cat_X^2$	0	0	1	1
	$Cat_Y^1$	0	1	0	0
	$Cat_Y^2$	0	1	0	0
$10^3\mathcal{K}$	$Cat_X^1$	0	261	261	87
	$Cat_X^2$	261	0	348	304
	$Cat_Y^1$	261	348	0	239
	$Cat_Y^2$	87	304	239	0

(1)

Stat	$Cat_k^m \setminus Cat_\ell^n$	$\Delta_G$			
		$Cat_X^1$	$Cat_X^2$	$Cat_Y^1$	$Cat_Y^2$
$\mathcal{H}$	$Cat_X^1$	0	0	1	1
	$Cat_X^2$	0	0	1	1
	$Cat_Y^1$	1	1	0	0
	$Cat_Y^2$	1	1	0	0
$10^3\mathcal{K}$	$Cat_X^1$	0	130	500	413
	$Cat_X^2$	130	0	435	413
	$Cat_Y^1$	500	435	0	196
	$Cat_Y^2$	413	413	196	0

(2)

Stat	$Cat_k^m \setminus Cat_\ell^n$	$L_\theta$			
		$Cat_X^1$	$Cat_X^2$	$Cat_Y^1$	$Cat_Y^2$
$\mathcal{H}$	$Cat_X^1$	0	0	1	1
	$Cat_X^2$	0	0	1	0
	$Cat_Y^1$	1	1	0	0
	$Cat_Y^2$	1	0	0	0
$10^3\mathcal{K}$	$Cat_X^1$	0	239	587	435
	$Cat_X^2$	239	0	348	261
	$Cat_Y^1$	587	348	0	152
	$Cat_Y^2$	435	261	152	0

(3)

Table 5.3: 1-D Kolmogorov–Smirnov test of sub-classes  $Cat_X^m$  and  $Cat_Y^n$  of  $Cat_X$  and  $Cat_Y$  respectively,  $m, n \in \{1, 2\}$ .

Statistic	$Cat_k \setminus Cat_\ell$	$Cat_X$	$Cat_Y$
$\mathcal{H}$	$Cat_X$	0	1
	$Cat_Y$	0	0
$10^3\mathcal{K}$	$Cat_X$	0	457
	$Cat_Y$	457	0

Table 5.4: 2-D Kolmogorov–Smirnov test of  $Cat_X$  and  $Cat_Y$ .

Stat	$Cat_k^m \setminus Cat_\ell^n$	$Cat_X^1$	$Cat_X^2$	$Cat_Y^1$	$Cat_Y^2$
$\mathcal{H}$	$Cat_X^1$	0	0	1	1
	$Cat_X^2$	0	0	1	1
	$Cat_Y^1$	1	1	0	0
	$Cat_Y^2$	1	1	0	0
$10^3\mathcal{K}$	$Cat_X^1$	0	217	652	478
	$Cat_X^2$	217	0	457	413
	$Cat_Y^1$	652	457	0	217
	$Cat_Y^2$	478	413	217	0

Table 5.5: 2-D Kolmogorov–Smirnov test of sub-classes  $Cat_X^m$  and  $Cat_Y^n$  of  $Cat_X$  and  $Cat_Y$  respectively,  $m, n \in \{1, 2\}$ .

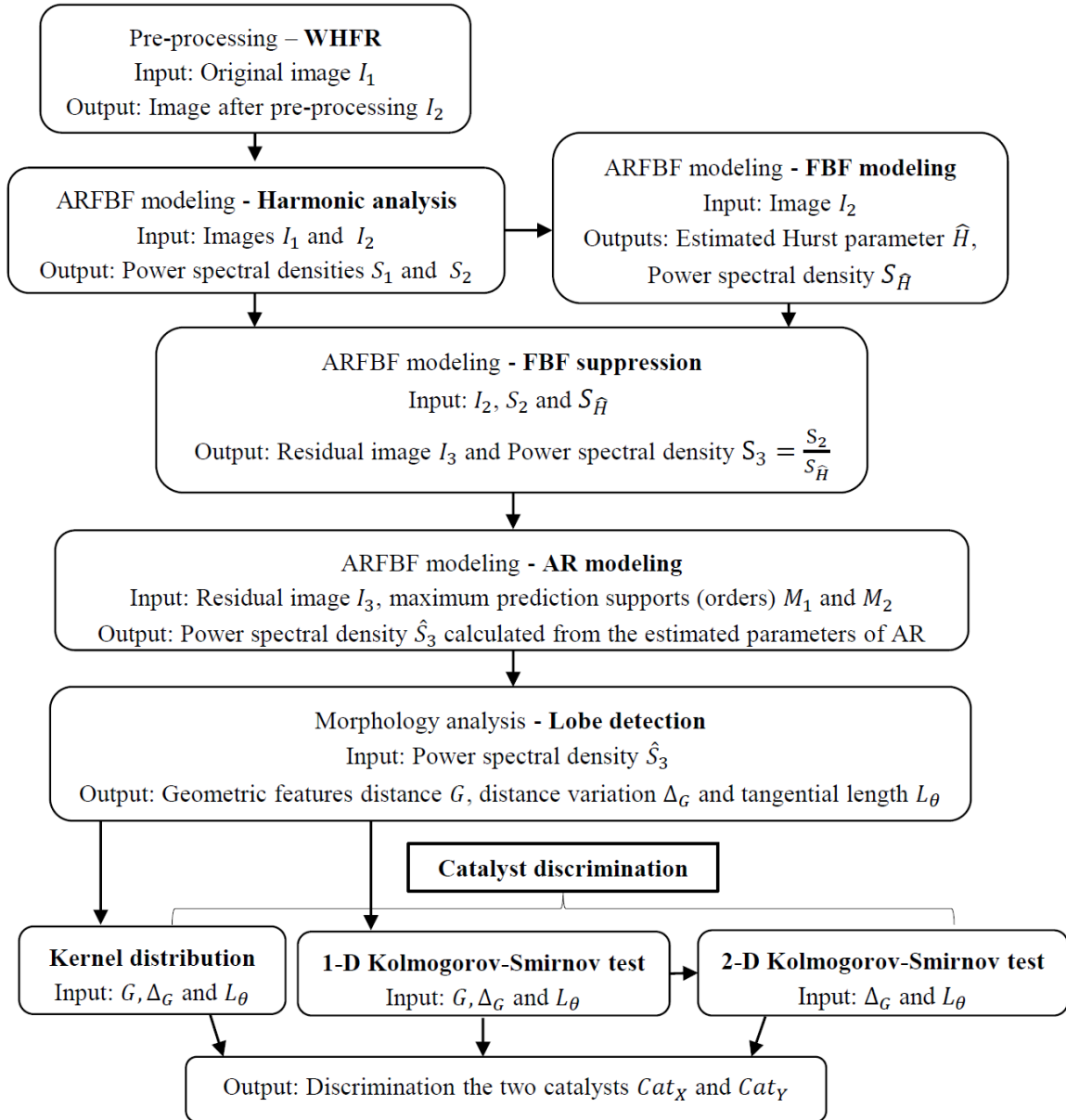


Figure 5.19: ARFBF modeling morphology analysis of HRTEM images of catalyst - ARFBF modeling morphological characterization of HRTEM image of catalyst and catalyst discrimination.



---

## General conclusion

---

This thesis presents two models and their application to HRTEM textures: Auto-Regressive Fractional Brownian Field (ARFBF) and  $K$ -factor Generalized Fractional Brownian Field (GFBF) with a focus on a subclass of the latter, subclass defined as a mixture of 2-factor Fractional Brownian Field (CMFBF).

The ARFBF model can characterize either stationary properties or some non-stationary properties involved in textures. With such a model, we can address the characterization of an HRTEM image presenting several spectral bumps or lumps as well as the relative distances and/or angles between bumps or lumps. The application of the proposed approach (ARFBF morphological analysis) suits for the description of HRTEM images corresponding to the observation of material microstructures at nanometer scale.

The  $K$ -factor GFBF model obtained from convolution and modulation operators over a sequence of fractional Brownian random fields associated with an arbitrary sequence of Hurst parameters is non-stationary and associated with several spectral poles, which make them powerful tools for structured random field synthesis.

For estimating the Hurst parameters involved in the ARFBF or GFBF models, we have proposed two methods based on Wavelet Packet (WP) spectrum: the Log-Regression on Diagonal WP spectrum (Log-RDWP) and the Log-Regression on Polar representation of WP spectrum (Log-RPWP). The Log-RPWP method provides a better estimation performance for small size images. The relevance of our method is highlighted by comparisons with the literature and its application to the analysis of HRTEM images.

The first application addressed is soot HRTEM image texture synthesis from  $K$ -factor GFBF modeling. A texture synthesized from  $K$ -factor GFBF possesses many spectral peaks and has exponential spectral decays in the neighborhood of these peaks. Such a spectral behavior can be observed in many structured/pseudo or quasi periodic textures issued from material sciences. In particular, textures synthesized from  $K$ -factor GFBF

have shown appealing structural content and similarities with some fringe structures encountered in HRTEM textures.

The second application deals with the CMFBBF modeling of an isolated HRTEM fringe of catalyst. The CMFBBF model has a spectral representation associated with two peaks and two Hurst parameters ( $H_0$  and  $H_1$ ). In HRTEM images, its peak located at zero frequency characterizes the background through its Hurst parameter  $H_0$  and the second peak is representative to fringes with a stochastic regularity parameter  $H_1$ . The synthesized textures by using Hurst parameters  $H_0$ ,  $H_1$  estimated from CMFBBF modeling of catalyst HRTEM image are shown to present some structural similarities with the original HRTEM fringes.

The last application is ARFBBF morphology analysis of HRTEM images of catalyst. Our proposed ARFBBF morphological analysis gives the description of HRTEM textures corresponding to the observation of material micro-structures at nanometer scale and allows for catalyst discrimination. This morphological description is based on 2-D parametric ARFBBF spectrum. The obtained features encompass heterogeneous HRTEM image background described by an FBF, active phase fringes associated with an AR model and geometric features derived by morphology analysis of the spectral fringe information. The proposed analysis allows to discriminate between two classes of catalysts and opens some prospects on monitoring of active phases associated with different materials at nanoscale.

In perspective, the performance of the ARFBBF and CMFBBF models must be evaluated qualitatively on several types of textures. For the  $K$ -factor GFBBF model, we need to perform a procedure for estimating all associated Hurst parameters, as well as a morphological analysis method (detection of the different lobes, discussion of the choice of associated values and their influence ...) in order to be able to apply it to the characterization of materials. Then, the  $K$ -factor AR-GFBBF will be studied: 1) estimation methods of the AR model, 2) estimation of the parameters in a sequential and then joint way and 3) application to the characterization of the images.

---

## Appendix: résumé substantiel

---

L'objectif principal de cette thèse est la proposition de modèles statistiques pour l'analyse et la caractérisation des images observées à Haute Résolution (échelle nanométrique) par Microscopie Électronique en Transmission (imagerie HRMET). L'application visée est la caractérisation des arrangements spatiaux de phases actives dans les catalyseurs afin de comprendre les propriétés de ces matériaux. Les contributions de cette thèse sont la proposition de deux modèles statistiques, deux méthodes d'estimation du paramètre de Hurst et leur application aux images HRMET :

- le premier modèle ARCBF (Champ Brownien Fractionnaire Auto-Régressif) est défini par une opération de convolution entre un Champ Brownien Fractionnaire (CBF) et un champ Auto-Régressif (AR). Nous avons également développé une méthode d'analyse morphologique dans le domaine fréquentiel associée au contenu ARCBF.
- le deuxième modèle  $K$ -facteurs CFBG (Champ Brownien Fractionnaire Généralisé) est basé sur des opérateurs de convolution et de modulation de CBF et représente une classe des modèles non-stationnaires et de champ multifractionnaires.
- la première méthode d'estimation est la méthode Log-RDPO (Log-Régression sur la Diagonale du spectre des Paquets d'Ondelettes),
- la deuxième méthode d'estimation est la méthode Log-PPPO (Log-Régression sur la représentation en coordonnées Polaires du spectre des Paquets d'Ondelettes),
- ces modèles et méthodes nous ont permis de synthétiser des textures proches visuellement de celles présentes dans les images HRMET et de discriminer deux types de catalyseurs.

Le premier chapitre présente le contexte, la motivation et les contributions principales réalisées dans cette thèse.

Le chapitre 2 décrit principalement la modalité d'imagerie utilisée. Il est constitué de 4 sections. La section 1 présente la microscopie électronique en transmission en rappelant les principes physiques et les contraintes de préparations des échantillons. La section 2 présente un premier ensemble d'échantillons d'images HRMET de nanostructures de particules de suie, produites par la combustion incomplète de carburants dans les moteurs diesel. La section 3 présente un deuxième ensemble d'échantillons d'images HRMET des phases actives de catalyseurs d'hydrotraitement. Toutes les images HRMET présentées dans ce travail sont produites à IFP Energies nouvelles, section Physique et Analyse, avec un microscope JEOL 2100F. Ces deux types d'images (suie et catalyseur) seront par la suite analysées et/ou synthétisées par les modèles et méthodes d'estimation proposés. La dernière section présente la relation entre la morphologie des phases actives des catalyseurs et leur observations dans le domaine spatial et fréquentiel.

Le chapitre 3 présente une étude bibliographique sur les modèles stochastiques. Pour commencer, nous rappelons les définitions et les propriétés des processus aléatoires à mémoire courte, à mémoire longue et auto-similaires. Quelques exemples en temps continu et discret sont fournis, tels que,

- en temps continu,
  - le modèle Gaussien H-ASIS (processus  $H$ –Auto-Similaire avec Incréments Stationnaires) appelé communément mouvement Brownien fractionnaire,
  - les modèles non-Gaussiens H-ASIS : processus  $\alpha$ -stables pour  $0 < \alpha < 2$ ;
- en temps discret, le processus  $K$ -facteur GARMM (Gegenbauer Auto-Régressif et Moyenne Mobile) avec ses cas particuliers tels que le processus ARFIMM (Auto-Régressif Fractionnaire Intégré et Moyenne Mobile) et le processus FI (Fractionnaire Intégré).

Ensuite, nous présentons les spécificités de l'extension de certains processus aléatoires aux champs aléatoires 2-D, notamment les CBF et les champs AR. Le paramètre de Hurst du CBF représente la régularité stochastique (rugosité de texture). La Densité Spectrale de Puissance (DSP) 2-D AR est calculée comme la moyenne harmonique de deux spectres associés à deux supports de prédiction Quart de plan (QP). Le spectre 2-D estimé à partir de cette méthode est facile à calculer et possède de bonnes propriétés d'estimation par rapport aux autres méthodes existantes. À un ordre fixé, les paramètres du modèle AR sont estimés grâce à la minimisation au sens des moindres carrés.

Le chapitre 4 est consacré à la présentation des modèles et des méthodes d'estimation du paramètre de Hurst qui sont les contributions apportées par cette thèse dans le domaine des statistiques. Il est constitué de 3 sections. La section 1 introduit le modèle ARCBF (champ  $Z(x, y)$ ) qui est la convolution (notation  $\otimes$ ) d'un champ AR  $A$  avec un CBF  $B_H$ , dans le but de décrire simultanément des dépendances à court et à long termes :

$$Z(x, y) = \left( A \otimes B_H \right) (x, y). \quad (7.1)$$

Nous désignons par  $S_A$ , le spectre d'un champ AR, et par  $S_{B_H}$ , le spectre du CBF. À partir de l'Eq. (7.1), le spectre associé au modèle ARCBF est

$$S_Z(u, v) = S_A(u, v) S_{B_H}(u, v). \quad (7.2)$$

L'estimation des paramètres du modèle ARCBF est réalisée de manière séquentielle: d'abord le paramètre de Hurst, puis les paramètres du modèle AR. La section 2 présente le modèle  $K$ -facteur CBFG ( $B_{G_{H_K}}$ ) défini par des convolutions de  $K$  CBFs modulés ( $B_{H_k}$ ),  $k = 1, 2, \dots, K$ ,

$$B_{G_{H_K}} = \bigotimes_{k=1}^K B_{H_k}. \quad (7.3)$$

L'ensemble de paramètres de ce modèle est  $\{H_1, H_2, \dots, H_K\}$  qui est une suite de paramètres de Hurst. Le spectre du  $K$ -facteur CBFG s'écrit de manière suivante :

$$S_{B_{G_{H_K}}}(u, v) = \prod_{k=1}^K S_{B_{H_k}}. \quad (7.4)$$

Le modèle  $K$ -facteur CBFG peut admettre un nombre arbitraire de points de singularité spectrale et de paramètres de Hurst. Nous avons étudié plus particulièrement le MCCBF (convolution d'un CBF et d'un CBF modulé) qui est un 2-facteur CBFG. Pour finir, la section 3 présente deux extensions de la méthode des paquets d'ondelettes pour rendre l'estimation du paramètre de Hurst du CBF plus robuste. Les performances des deux méthodes proposées, Log-RDPO et Log-RPPO, sont analysées de manière quantitative et montrent une meilleure robustesse pour la méthode Log-RPPO. La méthode Log-RPPO est alors comparée à d'autres méthodes issues de la littérature. Les résultats sont globalement convaincants et soulignent l'intérêt de l'approche proposée.

Le chapitre 5 concerne les applications des modèles et méthodes d'estimation proposés aux images HRMET. Il s'agit d'une part importante du travail dans cette thèse et représente la partie appliquée des contributions. Ce chapitre est constitué de 3 sections. La section 1 présente la modélisation d'images HRMET de suite par le modèle  $K$ -facteur CBFG. Les structures des textures synthétiques présentent des similitudes avec celles des images HRMET. Il est montré qualitativement que le modèle  $K$ -facteur CBFG peut permettre de représenter des images HRMET réelles. La section 2 est consacrée à la modélisation des images HRMET de catalyseurs avec le modèle MCCBF, une sous-classe du modèle  $K$ -facteur CBFG. La représentation spectrale du MCCBF est associée à deux pics. Le pic à la fréquence zéro correspond au fond de l'image (considéré comme arrière plan) et modélisé par un CBF de paramètre  $H_0$ . Le pic situé ailleurs correspond à la phase active (information à caractériser) et modélisé par un CBF modulé de paramètre  $H_1$ . Le modèle MCCBF est alors utilisé pour la synthèse de textures HRMET de catalyseurs (voir Fig. 7.1). La procédure utilisée est:

- Étape 1, pour l'image d'origine  $I_1$ , le Spectre par Paquets d'Ondelettes (SPO)  $S_1$  est calculé.
- Étape 2, le paramètre de Hurst  $H_0$  du CBF est estimé.
- Étape 3, la contribution du CBF dans  $I_1$  est supprimée. Pour l'image résiduelle  $I_2$ , son SPO  $S_2 = \frac{S_1}{S_{H_0}}$ . Le pic à l'origine des fréquences est bien modélisé par un CBF, car l'énergie autour de la fréquence nulle a été presque totalement supprimée.

- Étape 4, le paramètre de Hurst  $H_1$  du modèle CBF modulé est estimé à partir de  $I_2$ .
- Étape 5, une image est synthétisée à l'aide d'un MCCBF de paramètre  $\{H_0, H_1\}$ . L'image synthétisée  $I_4$  et son SPO  $S_4$  présentent des similitudes avec  $I_1$  et  $S_1$ .

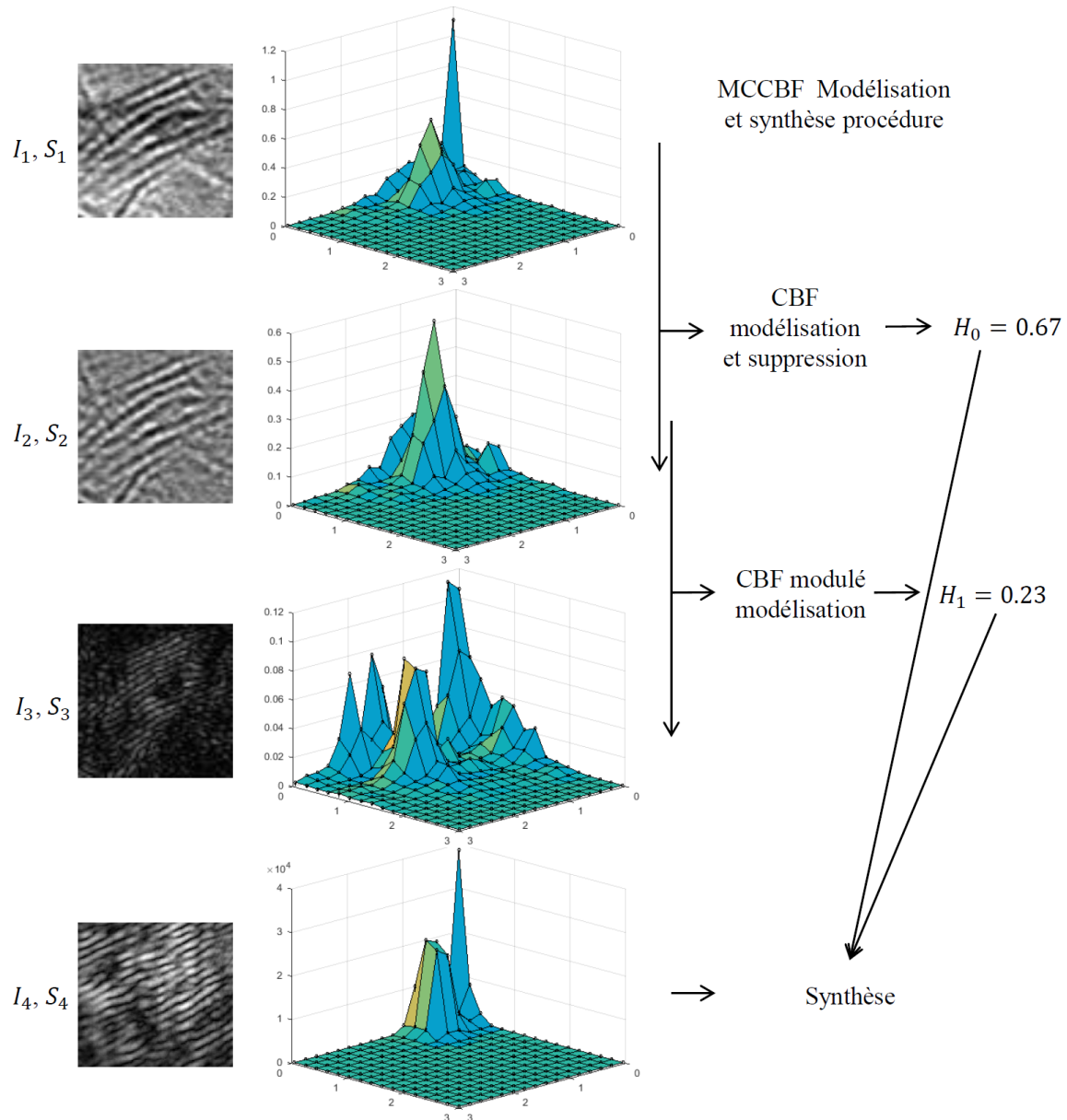


Figure 7.1: Modèle MCCBF pour la synthèse de textures HRMET de catalyseurs.

La section 3 montre l'intérêt pratique du modèle ARCBF grâce à une analyse morphologique dans le domaine des fréquences. L'application du modèle ARCBF aux images HRMET de catalyseurs est illustrée Fig. 7.2. Sa procédure utilisée est:

- Étape 1, la DSP  $S_1$  de l'image d'origine  $I_1$  est calculée.  $I_1$  contient plusieurs hautes fréquences qui sont induites par le support d'alumine du catalyseur et le bruit électronique.

- Étape 2, on applique alors un pré-traitement appelé SHFO (Suppression des Hautes Fréquences basée Ondelette) à  $I_1$ . La DSP  $S_2$  de l'image après traitement  $I_2$  est calculée. Les hautes fréquences sont bien supprimées avec la méthode SHFO.
- Étape 3, le paramètre de Hurst  $H$  d'un CBF est estimé à partir de  $I_2$  à l'aide de méthode Log-RPPO.
- Étape 4, la contribution du CBF dans  $I_2$  est supprimée. La DSP  $S_3 = \frac{S_2}{S_H}$  de l'image résiduelle  $I_3$  est calculée.
- Étape 5, les paramètres d'un modèle AR d'ordre (10,10) sont estimés à partir de  $I_3$ .
- Étape 6, la DSP (absolument continue) de  $I_3$  (noté  $S^*(r, \theta)$  en coordonnées polaires et  $S^*(u, v)$  en coordonnées cartésiennes) est calculée en utilisant les paramètres estimés du modèle AR.  $S^*(u, v)$  est une version lisse de  $S_3$  (les  $S_1, S_2, S_3$  de la Fig. 7.2 sont obtenues à partir du module de la transformée de Fourier discrète 2D).

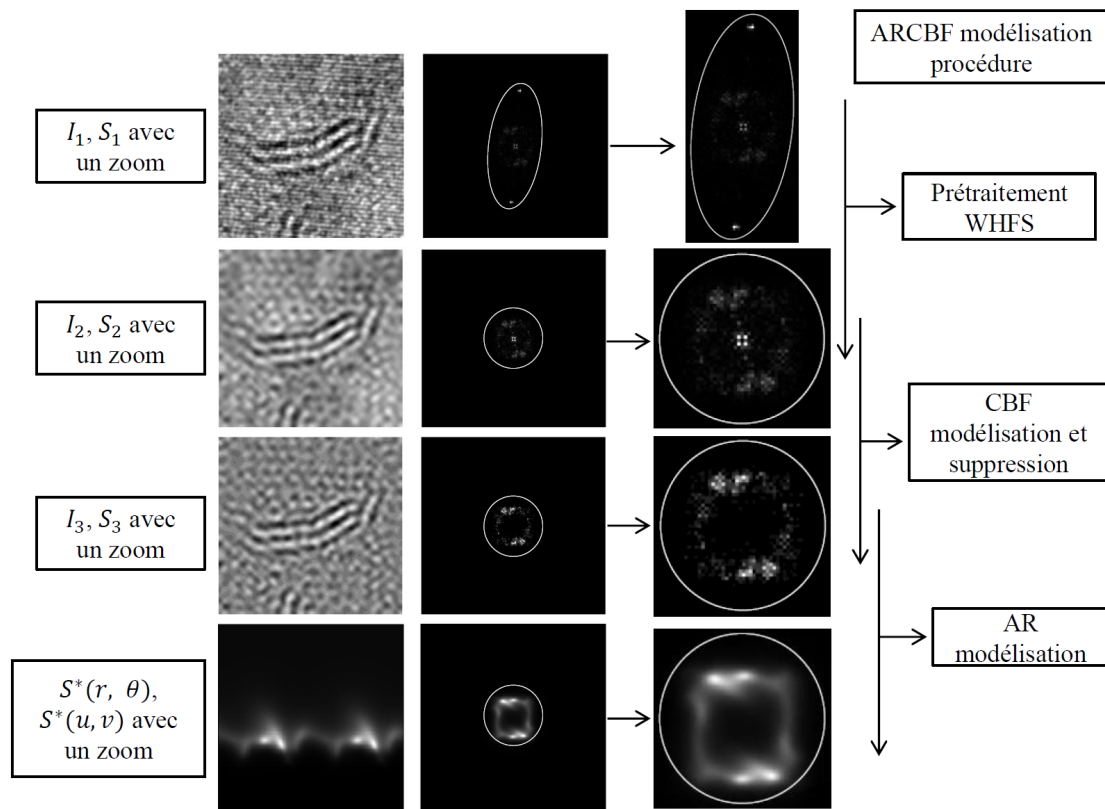


Figure 7.2: Application du modèle ARCBF aux images HRMET de catalyseurs

Nous avons ensuite réalisé une analyse morphologique à partir de  $S^*(r, \theta)$  afin de décrire des propriétés géométriques des phases actives: la distance spatiale entre couches atomiques  $G$ , la variation de cette distance  $\Delta_G$  et longueur tangentielle  $L_\theta$  en rapport avec les changements d'orientation des franges. Ensuite à l'aide d'analyses statistiques (estimation de densités de probabilité par la méthode à noyau et le test Kolmogorov Smirnov),

nous avons montré qu'il était possible de distinguer les deux types de catalyseurs étudiés.

Le chapitre 6 termine cette thèse par une conclusion qui résume les contributions et propose quelques pistes d'investigation à partir des modèles stochastiques proposés. En conclusion, cette thèse présente des contributions en rapport avec modèles (CBF, MC-CBF,  $K$ -facteur CBFG et ARCBF) et leur applications.

- Pour le modèle CBF, nous avons proposé deux méthodes d'estimation du paramètre de Hurst (Log-RDPO et Log-RPPO) et la méthode Log-RPPO possède de meilleures performances d'estimation pour les images de petites tailles par rapport à la méthode Log-RDPO et un bon comportement par rapport aux méthodes de l'état de l'art.
- A l'aide du modèle MCCBF, nous avons effectué la modélisation et la synthèse de franges dans les images HRMET. Des similitudes entre images d'origine et les images synthétisées montrent la pertinence du modèle.
- Pour le modèle  $K$ -facteur CBFG, des similitudes liées à la présence de franges dans les images HRMET de suies et dans les textures synthétisées montre son intérêt pour la synthèse de champs aléatoires structurés.
- Le modèle ARCBF a été appliqué à la caractérisation des arrangements spatiaux dans des images HRMET de catalyseurs par la réalisation d'une méthode d'analyse morphologique.

En perspective, les performances des modèles ARCBF et MCCBF doivent être évaluées de manière qualitative sur plusieurs types de textures. Pour le modèle  $K$ -facteur CBFG, nous devons réaliser une procédure d'estimation de tous les paramètres de Hurst associés, ainsi qu'une méthode d'analyse morphologique (détection des différents lobes, discussion les choix des valeurs associées et leur influence...) afin de pouvoir réaliser son application à la caractérisation des matériaux. Puis, le modèle  $K$ -facteur AR-CBFG sera étudié: 1) méthodes d'estimation du modèle AR, 2) estimation des paramètres de manière séquentielle puis conjointe et 3) application à la caractérisation des images.

---

## Bibliography

---

- [1] H. Akaike. A new look at the statistical model identification. *IEEE Transactions on Automatic Control*, 19:716 – 723, 1974.
- [2] O. Alata. Caractérisation de textures par coefficients de réflexion 2-d - application en classification et segmentation, "partie 1. modélisation de champs aléatoires 2-d". *Thèse de Doctorat, Université Bordeaux I, France*, 1998.
- [3] O. Alata and C. Cariou. *Two-Dimensional Signal Analysis, Chapter "2-D Linear Stochastic Modeling"*, chapter 2, pages 65–114. ISTE, Wiley, 2008.
- [4] O. Alata and C. Cariou. *Two-Dimensional Signal Analysis, Chapter "2-D Spectral Analysis"*, chapter 3, pages 115–174. ISTE, Wiley, 2008.
- [5] O. Alata, C. Cariou, C. Ramananjara, and M. Najim. Classification of rotated and scaled textures using hmhv spectrum estimation and the fourier-mellin transform. *Image Processing, ICIP*, 1:53–56, 1998.
- [6] O. Alata and C. Olivier. Choice of a 2-d causal autoregressive texture model using information criteria. *Pattern Recognition Letters*, 2003.
- [7] O. Alata and C. Ramananjara. Unsupervised textured image segmentation using 2-d quarter plane autoregressive support with four prediction support. *Pattern Recognition Letters*, 26:1069–1081, 2005.
- [8] A. M. Atto, Y. Berthoumieu, and P. Bolon. 2-dimensional wavelet packet spectrum for texture analysis. *IEEE Transactions on Image Processing*, 2013.
- [9] A.M. Atto and Y. Berthoumieu. How to perform texture recognition from stochastic modeling in the wavelet domain. *IEEE ICASSP*, 2011.
- [10] A.M. Atto, D. Pastor, and G. Mercier. Wavelet packets of fractional brownian motion: Asymptotic analysis and spectrum estimation. *IEEE Transactions on Information Theory*, 56:4741 – 4753, 2010.

- [11] A.M. Atto, Z. Tan, O. Alata, and M. Moreaud. Non-stationary texture synthesis from random field modeling. *Image processing, ICIP*, pages 4266–4270, 2014.
- [12] R.T. Baillie. Long memory process and fractional integration in econometrics. *Journal of Econometrics*, 73:5–59, 1996.
- [13] J. Beran. *Statistics for long memory, Chapter "Stationary processes with long memory"*, chapter 2, pages 41–59. Chapman and Hall, New York, 1994.
- [14] S. Bertelli and M. Caporin. A note on calculation auto-covariance of long memory processes. *Journal of Time Series Analysis*, 23, 2002.
- [15] G. Bertoni and J. Verbeeck. Accuracy and precision in model based eels quantification. *Ultramicroscopy*, 108:782–790, 2008.
- [16] G. Boon and G. Bastin. Quantitative analysis of thin specimens in the tem using a  $\phi(\rho z)$  model. *Microchimica Acta*, 147:125–133, 2004.
- [17] S. Bres, B. Celse, P. Guérout, F. Moreau, and L. Sorbier. Semi-automatic detection of sulfur slabs. *International Conference on Stereology and Image Analysis in Material Science, STERMAT2008, Zakopane, Pologne*, pages 2–6, 2008.
- [18] E.L. Church and P.Z. Takacs. *Handbook of Optics, 3rd edition, Chapter "Surface Scattering"*, chapter 8. M. Bass, Editor. McGraw-Hill, 2010.
- [19] R.R. Coifman and D.L. Donoho. Translation invariant de-noising. *Lecture Notes in Statistics*, 103:125–150, 1995.
- [20] C. Collioux. *La Microscopie Electronique, Chapter "Comprendre les images"*, chapter V. Presse Universitaire de France, 1996.
- [21] C. Collioux. *La Microscopie Electronique, Chapter "Les échantillons pour la microscopie électronique"*, chapter IV. Presse Universitaire de France, 1996.
- [22] C. Collioux. *La Microscopie Electronique, Chapter "Les principaux éléments du microscope électronique"*, chapter III. Presse Universitaire de France, 1996.
- [23] G. Cross and A.K. Jain. Markov random field texture models. *IEEE Transaction on Pattern Analysis and Machine Intelligence*, 5:25–39, 1983.
- [24] A. Datye, S. Srinivasan, L. Allard, C. Peden, J. Brenner, and L. Thompson. Oxide supported  $mos_2$  catalysts of unusual morphology. *Journal of Catalysis*, 158:205–216, 1996.
- [25] I. Daubechies. Ten lectures on wavelets. *CBMS-NSF conference series in applied mathematics, SIAM Ed*, 1992.
- [26] W. Eltzner, M. Breysse, M. Lacroix, C. Leclercq, M. Vrinat, A. Muller, and E. Die-mann. A new highly active hydrotreating catalysts prepared by the decomposition of thiotungstatonickelate and characterized by high resolution electron microscopy. *Polyhedron*, 7:2405–2409, 1988.

- [27] R.F. Engle. Antoregressive conditional heteroscedasticity with estimates of the variance of united kingdom inflation. *Journal of Econometrica*, 50:987–1008, 1982.
- [28] H. Federer. Geometric measure theory. *Springer Verlag, New York*, 1969.
- [29] H. Federer. Colloquium lectures on geometric measure theory. *Bull. Am. Math. Soc*, 84:291–338, 1978.
- [30] L. Ferrara and D. Guégan. Forecasting financial times series with generalized long memory processes. *Computational Finance*, 1:319–342, 2000.
- [31] P. W. Fieguth and A. S. Willsky. Fractal estimation using models on multiscale trees. *IEEE Trans. Signal Proc.*, 44:1297–1300, 1996.
- [32] P.A. French, J.R. Zeidler, and W.H. Ku. Enhanced detedctability of small objects in correlated clutter using an improved 2-d adaptive lattice algorithm. *IEEE Transactions on Image Processing*, 6:383–397, 1997.
- [33] M. Frenklach and H. Wang. Detailed modeling of soot particle nucleation and growth. *Symposium (International) on Combustion*, 23:1559–1566, 1991.
- [34] C. Geantet and L. Sorbier. Chapter 2.6 - characterisation of catalysts. *STDI Frame Maker*, 2012.
- [35] S. Geman and D. Geman. Stochastic relaxation, gibbs distribution, and the bayesian restoration of images. *IEEE Transaction on Pattern Analysis and Machine Intelligence*, PAMI-6:721–741, 1984.
- [36] G. Georgiadis, Alessandro Chiuso, and S. Soatto. Texture compression. *Processing DCC*, pages 221–230, 2013.
- [37] J. Geweke and S. Porter-Hudak. The estimation and application of long memory time series models. *Journal of Time Series Anal.*, 4:221–237, 1983.
- [38] L. Giraitis and R. Leipus. A generalized fractionally differencing approach in long memory modeling. *Lithuanian Mathematical Journal*, 35:65–81, 1995.
- [39] C.W.J. Granger and R. Joyeux. An introduction to long memory times series models and fractional differencing. *J. Time Series Analysis*, 1:15–29, 1980.
- [40] H.L. Gray, H.F. Zhang, and W.A. Woodward. On generalized fractional processes. *J. Time Series Analysis*, 10(3):233–257, 1989.
- [41] C.M. Grinstead and J. L. Snell. *Introduction to Probability, 2en Rev edition, Chapter "Markov Chains"*, chapter 11, pages 405–470. American Mathematical Society, 1997.
- [42] X. Guyon. Champs aléatoires sur un réseau. *Modélisations statistiques et applications*, page 226 pages, 1993.
- [43] B. E. Hansen. Lecture notes on nonparametrics. *University of Wisconsin*, Spring 2009.

- [44] T. Hayden and J. Dumesic. Studies of the structure of molybdenum oxide and sulfide supported on thin films of alumina. *Journal of Catalysis*, 103:366–384, 1987.
- [45] T. Hayden, J. Dumesic, R. Sherwood, and R. Baker. Direct observation by controlled atmosphere electron microscopy of the changes in morphology of molybdenum oxide and sulfide supported on alumina and graphite. *Journal of Catalysis*, 105:299–318, 1987.
- [46] J.R.M. Hosking. Fractional differencing. *Biometrika*, 68(1):165–176, 1981.
- [47] Q. Huang, J. R. Lorch, and R. C. Dubes. Can the fractal dimension of images be measured? *Pattern Recognition*, 27:339–349, 1994.
- [48] Z. Huang and B.K. Ray. Anisotropic fractional brownian random fields as white noise functionals. *Acta Mathematicae Applicatae Sinica, English Series*, 21:655–660, 2005.
- [49] C.M. Hurvich and C. Li. Estimation of the memory parameter for nonstationary or noninvertible fractionally integrated processes. *Journal of Time Series Analysis*, 16:017–042, 1995.
- [50] Y. Iwata, Y. Araki, K. Honna, Y. Miki, K. Sato, and H. Shimada. Hydrogenation active sites of unsupported molybdenum sulphide catalysts for hydroprocessing heavy oils. *Catalysis Today*, 65:335–341, 2001.
- [51] L. B. Jackson and H. C. Chien. Frequency and bearing estimation by two-dimensional linear prediction. *IEEE ICASSP*, pages 665 – 668, 1979.
- [52] D. Jacobs. Correlation and convolution. *Class Notes for CMSC*, 426, 2005.
- [53] A.K. Jain. Advances in mathematical models for image proceeding. *Proceedings of the IEEE*, 69:502–528, 1981.
- [54] M. José-Yacamán, G. Díaz, and A. Gómez. Electron microscopy of catalysts; the present, the future and the hopes. *Catalysis Today*, 23:161–199, 1995.
- [55] R.L. Kashyap and R. Chellappa. Estimation and choice of neighbors in spatial-interaction models of images. *IEEE Transaction on Information Theory*, IT-29:60–71, 1983.
- [56] V. Keast, A. Scott, R. Brydson, D. Williams, and J. Bruley. Electron energy-loss near-edge structure - a tool for the investigation of electronic structure on the nanometer scale. *Journal of Microscopy*, 203:135–175, 2001.
- [57] D. P. Kroese and Z. I. Botev. Spatial process generation. *Statistics Computation*, 2013.
- [58] N. Lamharess, C. Millet, L. Starck, E. Jeudy, J. Lavy, and P. D. Costa. Catalyzed diesel particulate filter: Study of the reactivity of soot arising from biodiesel combustion. *Catalysis Today*, 176:219–224, 2011.

- [59] A. Levasseur, E. Schmidt, G. Meunier, D. Gonbeau, L. Benoist, and G. Pfister-Guillouzo. New amorphous molybdenum oxysulfide thin films - their characterization and their electrochemical properties. *Journal of Power Sources*, 54:352–355, 1995.
- [60] M. Liu. Asymptotics of nonstationary fractional integrated series. *Econometric Theory*, 14:641–662, 1998.
- [61] X. Liu. Modélisation paramétrique en traitement d'images: algorithmes adaptatifs 2-d en treillis de type moindres carrés. *Thèse de Doctorat, Université de Bordeaux, France*, 1993.
- [62] P. Loubaton. Champs stationnaires au sens large sur  $z^2$ : propriétés structurelles et modèles paramétriques. *Traitement du signal*, 6, 1989.
- [63] Z. Lu. Analysis of stationary and non-stationary long memory process: Estimation, application and forecast. *Ecole Normale Supérieure de Cachan and East China Normal University*, 2009.
- [64] AP. Lévy. Random functions: General theory with special reference to laplacian random functions. *Univ. California Pul. Statist.*, 1:331–390, 1953.
- [65] J. Lynch. Microscopie électronique à transmission. analyse physico-chimique des catalyseurs industriels (j. lynch, ed). *Editions Technip, Paris*, pages 171–198, 2001.
- [66] S. Mallat. A theory for multiresolution signal decomposition: the wavelet representation. *IEEE Pattern Anal. and Machine Intell.*, 11:674–693, 2008.
- [67] B.B. Mandelbrot. *The fractal geometry of nature, Chapter "Three classic fractals, tamed"*, chapter 2, pages 25–74. W.H. Freeman and Company, New York, 1977.
- [68] B.B. Mandelbrot and J.W. Van Ness. Fractional brownian motions, fractional noises and application. *SIAM Review*, 10:422–437, 1968.
- [69] J. Mao and A.K. Jain. Texture classification and segmentation using multi-resolution simultaneous autoregressive (mr-sar) models. *Pattern Recognition*, 25:173–188, 1992.
- [70] R. Meylani, A. Ertuzun, and A. Ercil. Texture defect detection using the adaptive two-dimensional lattice filter. *Proc. IEEE ICASSP*, pages 165–168, 1996.
- [71] M. Moreaud, D. Jeulin, A. Thorel, and J. Y. Chane-Ching. A quantitative morphological analysis of nanostructured ceria-silica composite catalysts. *Journal of Microscopy*, 232:293–305, 2008.
- [72] G.P. Nason and B.W Silverman. The stationary wavelet transform and some statistical applications. *Lecture Notes in Statistics*, 103:281–299, 1995.
- [73] P.A. Nikulshin, D.I. Ishutenko, A.A. Mozhaev, K.I. Maslakov, and A.A. Pimerzin. Effects of composition and morphology of active phase of  $\text{CoO}/\text{Al}_2\text{O}_3$  catalysts prepared using  $\text{Co}_2\text{MoO}_7$ -heteropolyacid and chelating agents on their catalytic properties in hds and hyd reactions. *Journal of Catalysis*, 312:152–169, 2014.

- [74] E. Parzen. On estimation of a probability density function and mode. *Ann. Math. Statist.*, 33:1065–1076, 1962.
- [75] R. I.A. Patterson and M. Kraft. Models for the aggregate structure of soot particles. *Combustion and Flame*, 151:160–172, 2007.
- [76] JA Peacock. Two-dimensional goodness-of-fit testing in astronomy. *Monthly Notices of the Royal Astronomical Society*, 202(3):615–627, 1983.
- [77] B. Pesquet-Popescu and P. Larzabal. 2d self-similar processes with stationary fractional increments. *Springer-Verlag in Fractals in Engineering*, pages 138–151, 1997.
- [78] B. Pesquet-Popescu and J. L. Véhel. Stochastic fractal models for image processing. *IEEE Signal Processing Magazine*, 19:48–62, 2002.
- [79] S. Pollack, J. Sanders, and R. Tischer. High-reflectance and single layer mos<sub>2</sub>: Two new forms. *Applied Catalysis*, 8:383–388, 1983.
- [80] A.D. Poularikas. *The Handbook of Formulas and Tables for Signal Processing, Chapter "Two-Dimensional Z-Transform"*, chapter 8. Boca Raton: CRC Press LLC, 1999.
- [81] I.U.H. Qazi, O. Alata, J.C. Burie, M. Abadi, A. Moussa, and C. Fernandez-Maloigne. Parametric models of linear prediction error distribution for color texture and satellite image segmentation. *Computer Vision and Understanding*, 115:1245–1262, 2011.
- [82] S. Ranganath and A. K. Jain. Two-dimensional linear prediction models - part i: spectral factorization and realization. *IEEE Transactions on Acoustic, Speech and Signal Processing*, ASSP-33(1):280–299, 1985.
- [83] J. Reyes-Gasca, S. Tehuacanero, and M. Yacamán. Moiré patterns in high resolution electron microscopy images of mos<sub>2</sub>. *Microscopy Research and Technique*, 40:2–9, 1998.
- [84] F. Richard and H. Bierme. Statistical tests of anisotropy for fractional brownian textures. application to full-field digital mammography. *Journal of Mathematical Imaging and Vision*, 36:227 – 240, 2010.
- [85] P. M. Robinson. Log-periodogram regression of times series with long range dependence. *The Annals of Statistics*, 23:1048–1072, 1995.
- [86] P. M. Robinson. Conditional sum of squares estimation of models for stationary time series with long memory. *Monograph Series*, 52:130–137, 2006.
- [87] M. Rosenblatt. Remarks on some nonparametric estimates of a density function. *Ann. Math. Statist.*, 27:832–837, 1956.
- [88] G. Samorodnitsky and M.S. Taquq. *Stable Non-Gaussian Random Processes: Stochastic Models with Infinite Variance, Chapter "Dependence structure of multivariate stable distributions"*, chapter 4, pages 173–217. Chapman and Hall, New York, 1994.

- [89] G. Samorodnitsky and M.S. Taqqu. *Stable Non-Gaussian Random Processes: Stochastic Models with Infinite Variance, Chapter "Self similar processes"*, chapter 7, pages 309–387. Chapman and Hall, New York, 1994.
- [90] G. Samorodnitsky and M.S. Taqqu. *Stable Non-Gaussian Random Processes: Stochastic Models with Infinite Variance, Chapter "Stable random process and stochastic integrals"*, chapter 3, pages 111–167. Chapman and Hall, New York, 1994.
- [91] J. Sanders. High resolution electron microscopy of some catalytic particles. *Chemica scripta*, 14:141–145, 1979.
- [92] J. Serra. Image analysis and mathematical morphology: Theoretical advances. *Academic Press, London*, 1988.
- [93] L. Sorbier, A. S. Gay, A. Fécant, M. Moreaud, and N. Brodusch. Measurement of palladium crust thickness on catalysts by optical microscopy and image analysis. *Microscopy and Microanalysis*, 2013.
- [94] P. Souza. Texture recognition via autoregression. *Pattern Recognition*, 15:471–475, 1982.
- [95] F. Sowell. Maximum likelihood estimation of stationary univariate fractionally integrated time series models. *Journal of Econometrics*, 53:165–188, 1992.
- [96] F. Sowell. Modeling long-run behavior with the fractional arima model. *Journal of Monetary Economics*, 29:277–302, 1992.
- [97] P.D. Tafti, D.V. De Ville, and M. Unser. Invariances, laplacian-like wavelet bases, and the whitening of fractal processes. *IEEE*, 2009.
- [98] Z. Tan, A. M. Atto, O. Alata, and M. Moreaud. Arfbf model for non-stationary random fields and application in hrtem images. *IEEE ICIP*, 2015.
- [99] M.S. Taqqu, V. Teverovsky, and W. Willinger. Is network traffic self similar or multifractal. *Fractals*, 5:63–73, 1997.
- [100] T.S. Totton, D. Chakrabarti, A.J. Misquitta, M. Sander, D.J. Wales, and M. Kraft. Modeling the internal structure of nascent soot particles. *Combustion and Flame*, 157:909–914, 2010.
- [101] H. Toulhoat and P. Raybaud. Catalysis by transition metal sulphides - from molecular theory to industrial application. *IFP Publications*, 2013.
- [102] B. Tsybakov and N.D. Georganas. On the self-similar traffic in atm queues: definitions, overflow probability bound, and cell delay distribution. *IEEE ACM Trans, Netw.* 5.3:397–409, 1997.
- [103] Radu D. Urs. Non parametric synthesis of volumetric textures from a 2d sample. *PhD thesis, University of Bordeaux, France*, 2013.

- [104] C. Velasco. Gaussian semiparametric estimation of non-stationary time series. *Journal of Time Series Analysis*, 20:87–127, 1999.
- [105] C. Velasco. Non-stationary log-periodogram regression. *Journal of Econometrics*, 91:325–371, 1999.
- [106] C. Velasco and P.M. Robinson. Whittle pseudo-maximum likelihood estimation for nonstationary time series. *Preprint*, 2000.
- [107] D. V. De Ville, T. Blu, and M. Unser. Isotropic polyharmonic b-splines: Scaling functions and wavelets. *IEEE*, 2005.
- [108] J. Wang. Champs markoviens multi-échelles: Applications à la segmentation d’images texturées et à la fusion multi-film. *Thèse de Doctorat, Université de Paris XI - Centre d’Orsay, France*, 1994.
- [109] H. Weyl. Bemerkungen zum begriff der differential-quotenten gebrochener ordnung. *Vierteljschr. Naturforsch. GES. Zurich*, 62:296–302, 1967.
- [110] W.A. Woodward, Q.C. Cheng, and H.L. Gray. A  $k$ -factor gamma long memory model. *Journal Time Series Analysis*, 19(5):485–504, 1998.
- [111] Valeriy V. Yashchuk, Andrew D. Franck, Steve C. Irick, Malcolm R. Howells, Alastair A. MacDowell, and Wayne R. McKinney. Two dimensional power spectral density measurements of x-ray optics with the micromap interferometric microscope. *Lawrence Berkeley National Laboratory*, 2005.
- [112] K. Yehliu, R.L. Vander Wal, and A.L. Boehman. A comparison of soot nanostructure obtained using two high resolution transmission electron microscopy image analysis algorithms. *Carbon (in press)*, 2011.
- [113] K. Yehliu, R.L. Vander Wal, and A.L. Boehman. Development of an hrtem image analysis method to quantify carbon nanostructure. *Combustion and Flame*, 158:1837–1851, 2011.
- [114] A.Z. Zambom and R. Dias. A review of kernel density estimation with application to econometrics. *Universidade Estadual de Campinas*, 2012.
- [115] B. S. Zhang, Y. J. Yi, W. Zhang, C. H. Liang, and D. S. Su. Electron microscopy investigation of the microstructure of unsupported ni-mo-w sulfide. *Materials Characterization*, 62:684–690, 2011.
- [116] P. Zhao and D.R. Yu. An ubbiased and computationally efficient ls estimation method for identifying parameters of 2-d noncausal sar models. *Materials Characterization*, 62:684–690, 2011.